Molecular Tagging Velocimetry for exploring rarefied gas flows

Zongwei Zhang

Université Fédérale
Toulouse Midi-Pyrénées

THÈSE

En vue de l'obtention du
DOCTORAT DE L'UNIVERSITÉ DE TOULOUSE

Délivré par l'Institut National des Sciences Appliquées de Toulouse

---

Présentée et soutenue par

Zongwei ZHANG

Le 24 octobre 2023

Vélocimétrie par marquage moléculaire pour analyser les écoulements de gaz raréfiés

---

Ecole doctorale : **MEGEP - Mécanique, Energétique, Génie civil, Procédés**

Spécialité : **Dynamique des fluides**

Unité de recherche :
ICA - Institut Clément Ader

Thèse dirigée par
Stéphane COLIN et Marco ROJAS CARDENAS

Jury

M. Jean-Christophe BATSALE, Rapporteur
M. David NEWPORT, Rapporteur
Mme Christine BARROT LATTES, Examinatrice
M. Lounès TADRIST, Président du jury
M. Stéphane COLIN, Directeur de thèse
M. Marcos ROJAS-CáRDENAS, Co-directeur de thèse

To my parents Yahui and Li

To my cousins Yang, Bo, and Cathy

To my soulmate Tan

Acknowledgements

I would like to take this opportunity to express my sincerest gratitude to all those who supported and guided me during my PhD studies. Thank you for your company and your emotional and scientific help. There were times when I would not have known what to do without your help. It is because of your helping hands that this doctoral thesis has been completed.

First of all, I would like to thank the members of the jury: Prof. Jean-Christophe BATSALE, Dr. David NEWPORT, Prof. Lounès TADRIST, and Dr. Christine BARROT LATTES. They read my thesis and attended my doctoral defense. I enjoyed the discussions with you. I am very grateful to the thesis reviewers Prof. Jean-Christophe BATSALE and Dr. David NEWPORT for their pertinent comments and valuable opinions on my thesis.

I would like to express my deep gratitude to my supervisors, Prof. Stéphane COLIN, and Dr. Marcos ROJAS-CARDENAS. Almost 4 years ago they chose me to come to France to do my PhD and I am very grateful to them for giving me this valuable opportunity. And throughout the whole process of studying for my PhD, they have always played the role of patient supervisors, family members and true friends. They have always given me firm support, invaluable guidance, and endless patience. Their presence has made me realize that there are times when the difficulties I encounter aren't worth getting me in such a bad mood because problems will always be solved and they will always be there to help me. Their expertise, meticulous explanations, and rigorous approach to research played a key role in this study. I learnt from them the rigor of a researcher and how to conduct research. Especially during the final period of writing the thesis and completing the publication and preparing for the defense, we went through a very difficult period together. They gave me their utmost help without any reservation. I always remember their patience and friendliness. I am grateful that they chose me 4 years ago and have helped me throughout these 4 years.

I would also like to express my sincere gratitude to the members of the Microfluidics Group: Prof. Lucien Baldas, Dr. Christine Barrot Lattes, Dr. Pascale Magaud, Dr. Ahmad Batikh, Dr. Stéphane Orieux, Mr. Nicolas Laurien, Dr. Dominique Fratantonio, Dr. Guillermo López-Quesada, Dr. Varun-Kumar Yeachana, Dr. Georges Saliba, Dr. Tohme Tohme, Dr. Dingdong Zhang,

Phassawat Leelaburanathanakul, Franz Schweizer, and Slaven Bajic. Their solidarity, willingness to share knowledge and spirit of cooperation have created a very excellent academic environment.

I would also like to thank Christine, who has been very helpful as part of my thesis supervisors team. I was impressed that when she was injured and had to work from home, she still insisted on having a Zoom meeting with me at 8:00 a.m. to solve a problem I was having with my experimental setup. I learnt from her how a female researcher with a successful career should balance her family life and research work. I have also been secretly learning her dressing style. Some of her ensembles are very tasteful and exquisite.

I am very grateful to Pascale for her friendliness and warmth. She is a very easy-going, very gentle, and friendly lady. I still remember in my first year of PhD, when we were having pizza together, she suggested to me that we should form a contact network of Chinese people in our research group and share contact information of our graduated and current Chinese students, which is a very good idea, but unfortunately, we don't have the time to do this. In my work, Pascal has always given me patience and valuable guidance, which I will always remember.

I would like to thank Lucien, who always helped me without hesitation from the beginning to the end. I will do my best to improve my French so that one day I hope I can understand the jokes between him and Stéphane.

I would also like to thank Ahmad for his valuable advice on the simulation work.

I would like to highlight my thanks to Dominique, who, as a senior PhD in our group, always lent me a helping hand during my PhD studies, whether I encountered problems with experimental setup or research ideas. Without his help, it is hard to say that I could have achieved what I have today. And his patience and friendliness I always remembered and deeply touched me. I was also impressed by his extremely gifted mathematical thinking.

Thanks to Zhenhang, I often dropped by your office to discuss some issues with you, ask for your opinion, draw on your experience, and sometimes shared some successes or joys with you. Of course, many times I have been dumping mental rubbish, thank you for listening and your valuable advice.

Thanks to Varun, your warmth and friendliness have always impressed me, and you gave us valuable experience and advice on the experimental work at the beginning of my thesis.

Thanks to Thome, as a senior PhD student and the president of the student union of the doctoral school, your experience and opinions have always taught me a lot. When I had my 1st Black Friday in France, due to the problem I encountered with my bank card payment, we waited together on the sofa of Galeries Lafayette for the salesman to solve the refund problem for me. I used the lipstick I bought then in my defense.

Thanks to George, a quiet friendly researcher. I learnt a lot from Georges's daily life and was impressed with his style in the form of generous research. Georges and I also enjoyed the noise-filled experimental environment together. I could often hear the noise of his experimental setup in my laser room.

I would like to also thank Marco Rosati, who was my 1st European friend in France. We completed the first six months of experimental training together and got some initial results, and I am very grateful to him for sharing what he learned with me throughout the process. I wish him all the best in Ireland and with his girlfriend Sarah.

Thank you, Guillermo, you have always surprised me with your friendliness and knowledge of China. I am honored to be one of the only several people in our group who can pronounce your name correctly in Spanish. It's very rare to meet someone who knows about China when you're abroad. Not to mention that you have been to China several times and to many different cities.

Thanks to Dingdong, we have been with each other for the past four years, finished each other's PhD thesis, and helped each other in the process. We helped each other through the process. I always remember that Dingdong and I moved some extremely heavy instruments together and completed some operations that I could not have done alone. I would also like to thank Bro Dong for always being a friendly smiling person and a good chef. I enjoyed the barbecue party with him as the chef. Fantastic and yummy yummy!

I can't thank Gems (Phassawat) enough. I was pleasantly surprised when I came into the office and saw you for the first time. When I was planning my trip to Thailand, you gave me a lot of valuable advice. And of course, you were inevitably dragged to the lab to help me several times, which was much appreciated! I still remember we shared the sweets we bought from Thailand and had a great time eating them. And the most amazing thing was that we lived in the same flat, where Georges also lived there of course. I was very happy to be able to have a hot pot with you. You've always been my compatriot in my eyes, no matter which language we were communicating in.

Thanks to Slaven, he gave me a newer and more comprehensive understanding of teamwork. This will make me more aware of teamwork in the future. I have learnt a lot from him.

I would also like to thank Dr.Anass Akrim for being my 1st office colleague and helping me with my life in the very beginning with his French.

Thanks to Dr. Sabrine Ziri, always very gentle in helping me with my problems in French.

I would also like to thank Nicolas for always helping me with my lab equipment.

I would also like to thank all of you in the Institut Clément Ader for providing me with a laboratory and working environment. I would like to thank Fermat for providing me with the lab equipment. I am grateful to CSC for financial support for my salary.

I am grateful to the staff of INSA Toulouse and the Doctoral School MEGEP, whose administrative assistance in all aspects of my research has been immeasurable.

I would like to thank my friends and family for their unwavering encouragement and understanding throughout this process. Their support has been the driving force that has kept me moving forward. Especially when I was going through the most difficult moments, it was due to their support that I was able to go on with my ideas. Thank you to my parents, they are always our strongest support. Thanks to Yang and Bo for bringing me a laptop from China, on which I did my thesis including this acknowledgements part. Especially Cathy and Tan, they always take care of me in my life, and when I encounter problems, their experience and opinions always point me to the right path. I guess all I must do is to always listen to you and do more with less.

Finally, I would like to express my sincere respect and gratitude to all those involved in this study and those around me. Thank you so much for your understanding, patience, tolerance, and kindness in all forms. I could not have come this far without you all. I hope that in the future, I will always be able to maintain contact and lifelong friendships with you all. Even though we have only worked together for a while, and we may not be in the same city or even the same country in the future, I would like to conclude by dedicating a line from a poem written during the Tang Dynasty in China: "海内存知己，天涯若比邻"(though we may be a world apart, friendship makes us neighbors at heart).

Sincerely,
Zongwei

Abstract

Molecular tagging velocimetry (MTV) is an optical, non-intrusive measurement technique, which has been widely used for gas and liquid flow visualization. The velocity measurement is realized by recording the temporal evolution of photoluminescence emission of tracer molecules, such as acetone vapor, which follow the gas flow. In this work, MTV was used for measuring velocity fields of rarefied gas flows in a millimetric channel. However, it is necessary to couple the molecular displacement measurements to a reconstruction method based on the advection-diffusion equation, in order to correctly extract the velocity profiles of the flow. In order to successfully implement this method, a correct estimation of the diffusion coefficient of the tracer molecules is necessary. Nevertheless, there is currently no definitive agreement in the literature regarding the value of the kinetic diameter of acetone, which compromises also the estimation of the diffusion coefficient. In this thesis, the diffusion coefficient was measured by recording the temporal evolution of the widening tagged line of acetone vapor. This work also offered an indirect experimental estimation of the kinetic diameter of acetone. This measurement helped us to improve the velocimetry measurements obtained via MTV in a novel transparent channel at low pressures.

Keyword: Molecular tagging velocimetry, rarefied gas flows, slip velocity, acetone, molecular diffusion, kinetic diameter

Résumé

La vélocimétrie par marquage moléculaire (MTV) est une technique de mesure optique non intrusive, qui a été largement utilisée pour la visualisation des écoulements de gaz et de liquide. La mesure de vitesse est réalisée en enregistrant l'évolution temporelle de l'émission photoluminescente de molécules traceurs, telles que la vapeur d'acétone dans le cas des gaz, portées par l'écoulement. Dans ce travail, la MTV a été utilisée pour mesurer les champs de vitesses des écoulements de gaz raréfié dans un canal de dimensions millimétriques. Cependant, il est nécessaire de coupler les mesures de déplacement moléculaire à une méthode de reconstruction basée sur l'équation d'advection-diffusion pour extraire correctement les profils de vitesse de l'écoulement. Afin de mettre en œuvre avec succès cette méthode, une estimation correcte du coefficient de diffusion des molécules traceuces est nécessaire. Néanmoins, à l'heure actuelle, il n'y a pas d'accord définitif dans la littérature en ce qui concerne la valeur du diamètre cinétique de l'acétone, ce qui compromet également l'estimation du coefficient de diffusion. Dans cette thèse, le coefficient de diffusion a été mesuré via l'enregistrement de l'évolution temporelle de l'élargissement de la ligne de traceur activée par un faisceau laser UV. Ce travail offre également une estimation expérimentale indirecte du diamètre cinétique de l'acétone. Cette mesure nous a permis d'améliorer les mesures de vélocimétrie obtenues par MTV dans un nouveau canal transparent adapté à des conditions de basse pression.

Mots-clés : Vélocimétrie par marquage moléculaire, écoulement de gaz raréfié, vitesse de glissement, acétone, diffusion moléculaire, diamètre cinétique

Nomenclature

Roman letters

Symbols	Description	Units
A	Area of the cross-section	[m^2]
a	Channel aspect ratio	[-]
a_i	Fitting coefficients	[-]
b	Channel width	[m]
C	Conductance of the gas system	[m^3]
C_1, C_2	Slip velocity boundary condition coefficients	[-]
c	Total velocity	[ms^{-1}]
c'	Molecular thermal velocity	[ms^{-1}]
$\overline{c'}$	Mean thermal velocity magnitude	[ms^{-1}]
c_r	Relative molecular velocity	[ms^{-1}]
D	Diffusion coefficient	[m^2s^{-1}]
D_m	Measured results of diffusion coefficient	[m^2s^{-1}]
$d_{m,avg}$	Mean value of the measured kinetic diameter	[m]
E	Laser fluence	[J m^{-2}]
$E_{1,init}$	Initial results measured by laser energy detector 1	[J]
$E_{2,img}$	Results measured by laser energy detector 1 during image acquisition	[J]
$E_{2,init}$	Initial results measured by laser energy detector 2	[J]
F	Force	[N]
$f(x)$	Gaussian fitting	[-]
$f(x)_{max}$	Gaussian peak	[-]

G	IRO gain	[-]
H	Channel height	[m]
$I_{f,ph}$	Luminescence emission rate	[ph m^{-2}]
k_1	rate constant of linear decay	[s^{-1}]
k_B	Boltzmann constant	[m^2 kg s^{-2} K^{-1}]
k_{nr}	Non-radiative constant	[s^{-1}]
k_{nr,T_1}	Internal non-radiative rate constant in the triplet state	[s^{-1}]
k_{ph}	Phosphorescence emission rate constant	[s^{-1}]
k_Q	Quenching rate constant per quencher molecule density	[s^{-1}]
k_r	Radiative rate constants	[s^{-1}]
k_λ	Mean free path coefficient	[-]
k_ν	Collision rate coefficient	[-]
L	Channel length	[m]
L_C	Characteristic length	[m]
$L_{C,min}$	Minimum of the characteristic length	[m]
M	Molar mass	[kg mol^{-1}]
M^2	M square of the laser beam	[-]
m	Molecular mass	[kg]
$\dot{m}$	Mass flow rate	[kg s^{-1}]
$\dot{m}_{CV}$	Mass flow rate measured from constant volume technique	[kg s^{-1}]
N_i	Number of averaged images	[-]
N_l	Number of laser pulses per image	[-]
n	Number density	[m^{-3}]
n_{abs}	Number density of absorbing molecules	[m^{-3}]
n_{iv}	Number of independent variables	[-]
n_Q	Molecular density of quenching species	[m^{-3}]
n_T	Molecular density of triplet molecules	[m^{-3}]

n_{T_1}	Temporal concentration of triplet acetone molecules	[m^{-3}]
n_x	Number of pixels in x-axis	[-]
p	Absolute Pressure	[Pa]
$p_1(t)$	Pressure from sensor 1	[Pa]
$p_{1,0}(t)$	Pressure from sensor 1 at the beginning of the flow	[Pa]
$p_2(t)$	Pressure from sensor 2	[Pa]
$p_{2,0}(t)$	Pressure from sensor 2 at the beginning of the flow	[Pa]
p_m	Mean pressure	[Pa]
p_{in}	Inlet pressure	[Pa]
p_{out}	Outlet pressure	[Pa]
Δp	Pressure difference	[Pa]
R	Gas constant	[$JK^{-1}mol^{-1}$]
R_S	Specific gas constant	[$m^2s^{-2}K$-1]
r	Distance between the center of two molecules	[m]
S	Gaussian peak	[-]
S_0	Ground singlet state	[-]
S_1	First excited singlet state	[-]
S_2	Second excited singlet state	[-]
S_i	Excited singlet state	[-]
$slope_{low}$	Lower border of the slope uncertainty	[m^2s^{-1}]
$slope_{up}$	Upper border of the slope uncertainty	[m^2s^{-1}]
T	Thermodynamic Temperature	[K]
T_0	Reference temperature	[K]
T_1	Triplet excited state	[-]
t	Delay time	[s]
t_0	Starting moment of the experiment	[s]
t_{CCD}	Exposure time of the CCD detector	[s]

Δt_{gate}	IRO gate time	[s]
U_{r,D_m}	Relative uncertainty of diffusion coefficient	[-]
U_{r,d_m}	Relative uncertainty of kinetic diameter	[-]
$U_{r,p}$	Relative uncertainty of pressure	[-]
$U_{r,slope}$	Relative uncertainty of slope	[-]
$U_{r,T}$	Relative uncertainty of temperature	[-]
u	Bulk macroscopical velocity of the gas flow	[ms^{-1}]
$\bar{u}_{2D}$	Mean velocity on a cross section	[ms^{-1}]
u_{cp}	Centerline Poiseuille axial velocity	[ms^{-1}]
$\bar{u}_{CV}$	Mean velocity on the center cross section obtained by dynamic constant volume technique	[ms^{-1}]
u_{gas}	Real velocity of the gas flow at the wall	[ms^{-1}]
$\bar{u}_{MTV}$	Mean velocity of the velocity profile obtained by molecular tagging velocimetry technique	[ms^{-1}]
u_s	Gas velocity out of the Knudsen layer	[ms^{-1}]
u_{slip}	Slip velocity	[ms^{-1}]
u_{sound}	Local speed of sound	[ms^{-1}]
u_{wall}	Velocity of the wall	[ms^{-1}]
V_0	Coefficient of volume	[m^3]
V_1	Volume of gas tank 1	[m^3]
V_2	Volume of gas tank 2	[m^3]
V_c	Collection volume	[m^3]
V_i	Vibrational energy levels	[-]
x, y, z	Spatial coordinates	[m]

Greek letters

Symbols	Description	Units

α_i	Adjusting parameter	[-]
β_{u1}	Correction factor on slip velocity	[-]
γ	Ratio of the specific heats of the gas	[-]
δ	Mean molecular spacing	[m]
ϵ_{FWHM}	Uncertainty of FWHM	[m]
ϵ_R	Resolution error	[m]
ϵ_t	Uncertainty of delay time	[s]
$\epsilon_{\mathrm{t-t_0}}$	Uncertainty of time difference	[s]
ϵ_{σ_x}	Uncertainty of standard deviation	[m]
$\epsilon_{\sigma_x^2}$	Uncertainty of variance	[m^2]
$\epsilon_{\sigma_{x,0}^2}$	Uncertainty of variance at initial time	[m^2]
$\epsilon_{\sigma_x^2(\mathrm{t})-\sigma_{x,0}^2}$	Uncertainty of variance difference	[m^2]
η_{opt}	Quantum yield	[-]
κ, η	Constant values of the force	[-]
λ	Mean free path	[m]
λ_{ex}	Excitation wavelength	[m]
λ_i	Wavelength of the laser idler laser beam	[m]
λ_p	Wavelength of the pump laser beam	[m]
λ_s	Wavelength of the signal laser beam	[m]
μ	Dynamic viscosity	[Pa s]
μ_0	Gas viscosity at reference temperature	[Pa s]
υ_{rate}	Collisional frequency or collision rate	[s^{-1}]
ξ	Velocity slip length or coefficient of slip	[m]
Π	Pressure ratio between the inlet and the outlet of the channel	[-]
ρ	Density	[kg m^{-3}]
$\sigma_{f,ph}$	Molecular absorption cross-section of the tracer	[m^2]
σ_T	Total collision cross-section	[m^2]
σ_{TMAC}	Tangential accommodation momentum coefficient	[-]
$\sigma_x^2(\mathrm{t})$	Evolution with time of the variance of the tagged molecules distribution of the tagged line	[m^2]

$\sigma_{x,0}^2$	Variance of the tagged line at the beginning of the experiments	[m^2]
τ	Characteristic time of intermolecular collisions	[s]
τ_f	Characteristic time of the flow	[s]
τ_{lf}	Lifetime of the luminescent signal	[s]
τ_{ph}	Time of phosphorescence	[s]
τ_{T_1}	Triplet lifetime	[s]
$\phi_{f,ph}$	Quantum yield	[-]
Ψ_i	Base functions for velocity distribution	[-]
Ω_i	Coefficients for 2D velocity profile	[-]
ω	Coefficient of IPL collisional model	[-]

Non-dimensional number

Kn	Knudsen number
Ma	Mach number
Re	Reynolds number

Subscripts

Ac	Acetone
n	Direction normal to the wall
s	Direction tangent to the wall
f	Fluorescence
ph	Phosphorescence
min	Minimum
in	Channel inlet
out	Channel outlet

Acronyms

APART	Air photolysis recombination tracking
AR	Anti-reflective

CCD	Charge-coupled device
CV	Constant volume
DCVT	Dynamic constant volume technique
DSMC	Direct Simulation Monte Carlo
FLEET	Femtosecond laser electronic excitation tagging
FOV	Field of view
FWHM	Full width at half-maximum
HEX	Heat exchanger
HS	Hard-sphere
IC	Integrated circuit
ICCD	Imager Intense progressive scan charge-coupled device
IPL	Inverse power law
IRO	Intensified relay optics
KL	Knudsen Layer
LDV	Laser Doppler velocimetry
LIF	Laser induced fluorescence
LIP	Laser induced phosphorescence
LIPA	Laser induced photochemical anemometry
L-J	Lennard-Jones
LOC	Lab-on-a-chip
MAVs	Micro aerial vehicles
MCP	micro channel plate
MEMS	Micro-electro-mechanical systems
MM	Maxwell molecules
MT	Molecular tagging
MTT	Molecular tagging thermometry
MTV	Molecular tagging velocimetry
NTV	Nitric oxide tagging velocimetry
OOC	Organ on a chip
OTV	Ozone tagging velocimetry

PHANTOMM	Photoactivated non-intrusive tracing of molecular motion
PIV	Particle image velocimetry
PLIF	Planar laser-induced fluorescence
POCT	Point-of-care testing
PTU	Programmable timing unit
RBC	Red blood cells
RELIEF	Raman excitation plus laser-induced electronic fluorescence
SC	Semiconductor
SEM	Scanning-electronic-microscope
SNR	Signal-to-noise ratio
SSE	Sum of Squared Errors
SST	Sum of Squares Total
TMAC	Tangential accommodation coefficient
TTA	Triplet-triplet annihilation
UV	Ultraviolet
VENOM	Vibrationally excited nitrous oxide monitoring
VHS	Variable hard-sphere
VSS	Variable soft-sphere

Table of Contents

Chapter 1 Introduction

1.1 MEMS technology

Micro-electro-mechanical systems (MEMS) are micrometric devices combining mechanical and electrical components which are mainly manufactured through micromachining techniques on silicon chips [1].

Compared to traditional macroscopic devices, MEMS have numerous attractive properties, such as small scale, lightweight, low volume, low energy consumption, low reagent consumption, low-cost, high system integration with electrical or electronic circuits, high resonance frequency, and multifunctionality [2]. The characteristic sizes can range from several millimeters to several micrometers. The MEMS concept dates back to the early 1960s [2], while its practical expansion to different applications was mainly due to electronics miniaturization, originating from the great development of semiconductor and integrated circuit (IC) technology. The micro motor, created by Fan et al in 1988 [3], represents the commencement of the micromachining technique (Figure 1.1).

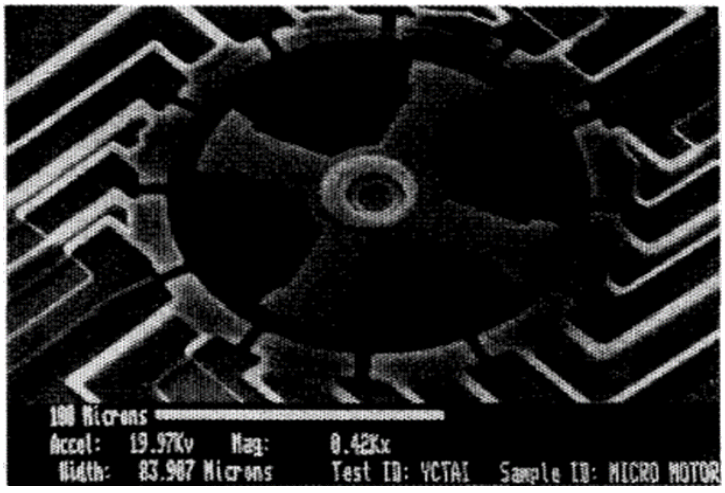

Figure 1.1. The scanning-electronic-microscope (SEM) image of the micro motor with 12-stator, 4-rotor-pole. The spacing between the stator and rotor is 6 μm. Reproduced from [3].

Historically, the MEMS fabrication was mainly based on IC fabrication techniques, involving materials such as silicon which had attractive properties, such as strong strength, conductivity, high robustness and so on. However, in recent years new varieties of materials, like polymers and glass, are used in MEMS devices fabrication in order to satisfy the increasing scientific and industrial requirements [1]. The main micro fabrication technique for MEMS manufacturing is based on lithographic technologies, bulk micromachining, surface micromachining, and LIGA techniques [1; 4].

During recent years, MEMS have experienced rapid development due to their unique advantages for a great variety of applications in several research and commercial fields [1; 4]. The potential market is today estimated in the order of billions of dollars. The earliest commercial applications are MEMS pressure sensor and accelerometers, which were widely used in the automotive industry [1]. Other traditional usages of MEMS devices were mainly focused on micro sensors, micro actuators, accelerometers, RF switches, etc. [5]. Nowadays, the application of MEMS devices has spread to much wider fields covering aerospace, military, microfluidics, read/write heads in computer storage systems and other micro device components.

1.2 MEMS-based microfluidic devices

Nowadays the MEMS technology has largely spread in the microfluidic scientific domain for fluid manipulation, such as the biomedical, chemical process, aeronautics, energy, automobile fields [6]. The advantages of using microfluidic devices are mainly related to their small scale, low energy consumption, high throughput and multifunctionality. The microfluidic devices could be divided into four main categories, which are micropumps, microvalves, microneedles, and micromixers [1]. To be more specific, the flows circulating inside microfluidic devices can also be divided into two other categories consisting of liquid and gas flows. The focus of the following sections will be around gas flows.

1.2.1 Microfluidics in biomedical application

The last decade has witnessed a considerable growth in biomedical or biological MEMS (BioMEMS). BioMEMS is a combination of MEMS technology and biological or biomedical

applications. The integrated multifunctional BioMEMS system is also called lab-on-a-chip (LOC), also known as micro-total analysis systems (μTAS). LOC devices are defined as a single chip combining a series of laboratory functions in a domain of several millimeters or several centimeters. According to the definition, the LOC system has the advantage in its high integration, miniaturization, automation, and parallel running of different analysis, which can offer a low-cost, quick-response, efficient-control, and high-performance biochemical analysis. Microfluidic based LOC devices can cover the whole laboratory functions on a single chip. Two typical microfluidic based LOC systems are point-of-care testing (POCT) and organ on a chip (OOC).

Several OOC platforms have been developed to reproduce cellular microenvironment for various organs and tissues. Benam et al. [7] has proposed a "small airway-on-a-chip" model for a lung-on-a-chip platform to mimic the Asthma by epithelium exposure to interleukin-13 (IL-13) for acquiring in vivo like responses to therapeutics. As demonstrated in Figure 1.2, the 'lung small airway-on-a-chip' could be mainly divided into three parts, from the top to the bottom, the air channel whose width and height are both 1 mm to mimic the human bronchiole, mucociliary bronchiolar epithelium layer, and the fluid flow channel. These devices might also contribute to lower the cost and time response of diagnostics in respect to large scale incidents, such as the global pandemic of COVID-19 [8] and or the study of the Influenza Virus evolution [9].

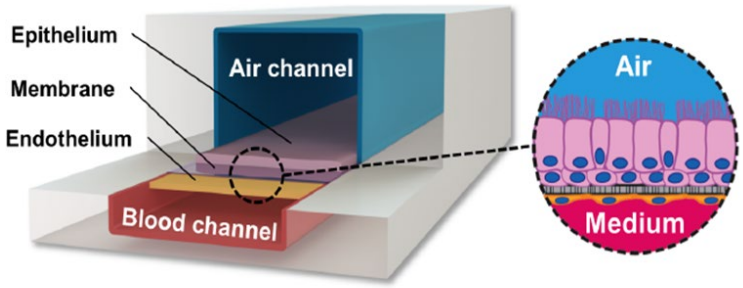

Figure 1.2 The sketch of lung small airway-on-a-chip. Reproduced from [7-9].

1.2.2 Microfluidics in aeronautics and spatial application

Microfluidics has become an important tool for aeronautical and space applications. Following, some examples will be listed. Pressure distributions were studied along micro aerial vehicles (MAVs) for aerodynamic shape design optimization, covering the information on

minimum pressure point, shake wave position and the air separation on the surface of aircraft [4]. A flexible microfluidic sensor was developed by Wang et al. [10] for aerodynamic pressure measurement on the aircraft surface (Figure 1.3.a). In order to advance the efficiency of aircraft from the view of skin friction drag, Hughes et al. [11] created a microfluidic sensor for local wall shear stress measurement. The sensor measurements were cross-verified by micro-PIV technique.

With the emergence of micro or nano spacecraft and satellites, the micro propulsion system needs to offer low thrust to maintain precise altitude control [12]. A 1-mN-class cold gas thruster was created by Janson et al in 1999 [13], which consists of two identical micro nozzles and two commercial silicon MEMS valves (Figure 1.3.b). The main component is the micro nozzle, which has a throat diameter of 100 μm and a length of 1 mm, fabricated by laser-processed Foturan technique (Figure 1.3.c).

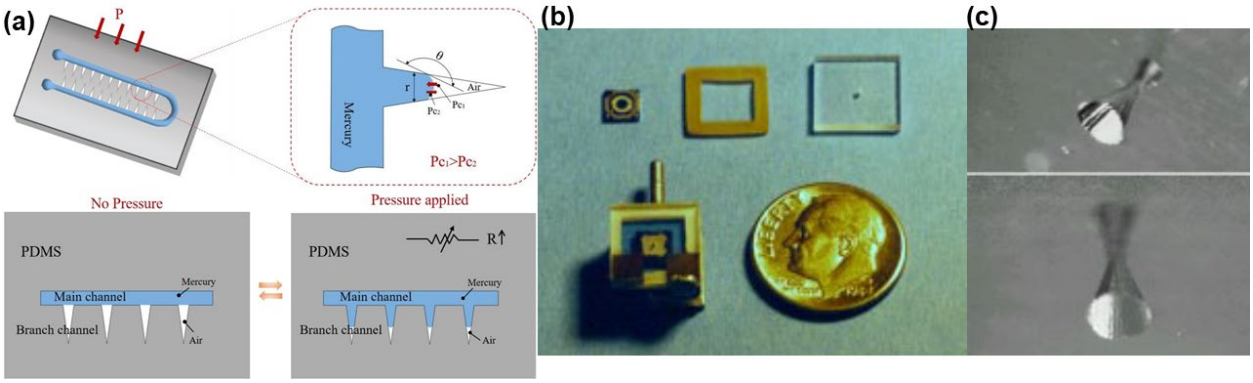

Figure 1.3 (a) The sensing mechanism of flexible microfluidic sensor; (b) A cold gas thruster; (c) Photo of a laser-machined nozzles. Reproduced from [10; 13].

A microfluidic system based on diverse industrial chemical sensors was integrated within an MAVs by Andrikopoulou et al. for monitoring and mapping outdoor air pollution(ELCOD Endurance Low Cost Drone Project) [14]. This integration can offer a comprehensive and global air measurement in the troposphere range. The microfluidic device inside the integrated measurement system was mainly used to maintain a proper flow rate environment for the micro sensors sampling.

Micro-jets have been used to decrease flow separation and skin friction, and to increase heat transfer on airfoils or other elements [4; 15]. Kumar and Alvi [16] confirmed that micro-jets based

actuators were promising for effective flow separation control in internal flows, such as inlets and channels in aircraft propulsion, and external flows, such as aircraft wings. The work of Khobragade et al. [17] also verified the effectiveness of micro-jet control in postponing flow separation for rocket science applications. The capability of the micro-jet array actuation method to decrease skin friction was validated by the work of Aubrun et al. [18]. The experimental work of Saliba et al. [19] proved that the pulsed impinging micro-jet can enhance the heat transfer for accelerating the cooling on heated boards.

1.2.3 Knudsen pump

Micro-pumps play an important role in the microfluidics actuation control. They can be classified as mechanical (moving parts) and non-mechanical (no-moving parts). For the non-mechanical cases, the driving force can come from thermal, chemical, electric, or magnetic effects. Without the moving part, non-mechanical micropumps have increased stability, sensitivity, life span and structure simplicity [20]. Knudsen pumps are a typical example of gas flow transport by using solely a temperature gradient along a confined rarefied gas flow [20-23]. These pumps (or compressors) are widely applied to vacuum generation, fluid delivery and gas separation.

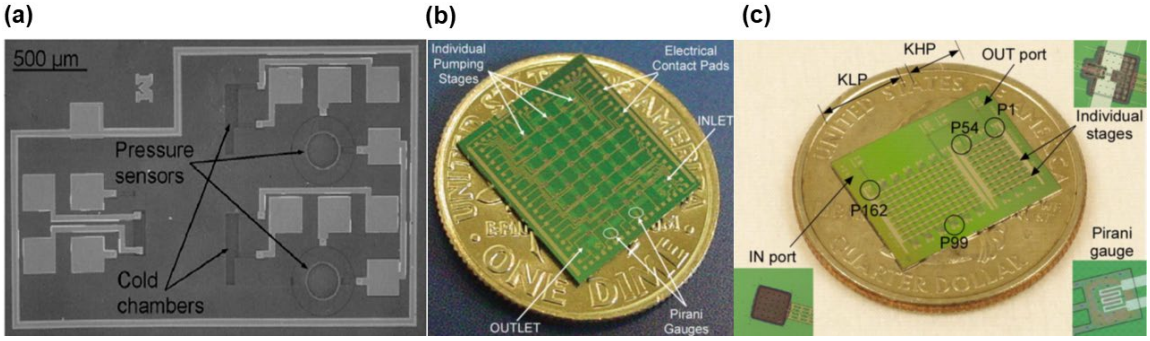

Figure 1.4 (a) one stage Knudsen pump; (b) 48-stage Knudsen pump; (c) 162-stage Knudsen pump. Reproduced from [24-26].

The first single stage Knudsen pump, was fabricated completely on silicon wafer in 2005 [24], integrated with two capacitive pressure sensors. The smallest dimension of the channels was 10 μm. This Knudsen pump was able to decrease the pressure in an 8×10^{-5} mm^3 chamber to 46.6 kPa within just two seconds for a compression ratio of 2. However, this single stage Knudsen pump cannot work with larger volumes. In order to increase the devices efficiency, a 48-stage Knudsen

pump with integrated Pirani gauges was created in 2012 [25]. The pressure drop for this device was considerably larger: more than 93.3 kPa of pressure difference could be achieved (smallest channel height h = 0.15 μm), for a maximum compression ratio of 50. In 2014, the same group proposed a 162- stage KP (smallest channel height of 0.1 μm), for a maximum compression ratio of 950, from 760 Torr to around 0.9 Torr [26]. Figure 1.4 compares the structure of single stage, 48-stage and 162-stage Knudsen pump.

Baier and co-authors [27] studied the gas separation phenomenon of binary gas mixtures (Helium–Xenon) along the Knudsen pump induced by a Crookes radiometer via direct simulation Monte Carlo (DSMC). Their work investigated the different behavior of the individual species in transport induced by composition, temperature, and pressure gradients. Gas separation was successfully accomplished in a model separation column inspired by opposing fluxes driven by thermal and pressure gradients, with a Knudsen number near unity. This study is important when utilizing the Knudsen pump to transport gas mixtures to a sensor surface, the detection properties of the sensor system can be affected by the preferential movement of different species in the gas mixture.

1.2.4 Micro heat exchangers

Due to its high heat transfer efficiency, micro heat exchangers, also known as μHx or microHEXs, have gained great interest among the industrial and scientific communities. The micro heat exchangers are most commonly used for cooling electronic components, MEMS or MOEMS [6].

Yang et al. have developed a gas-to-gas double layer μHx to study the behavior of gas flow and heat transfer through microHEXs by means of both experimental and numerical methods [28]. As shown in Figure 1.5, 133 microchannels were fabricated on a PEEK layer. Based on this new design, a study on the gas forced convection at the microscale verified the applicability of the recent conventional theory in respect to convective heat transfer in gas micro flows.

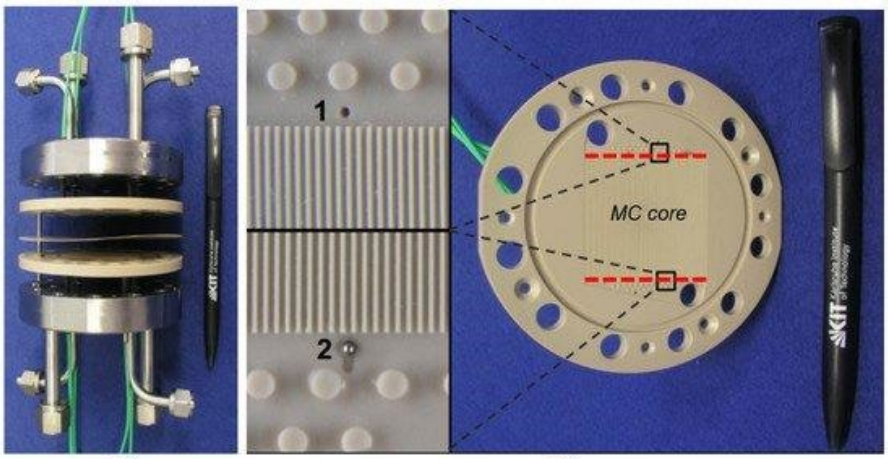

Figure 1.5. (a) A double layer Micro heat exchangers (μHx) created; and (b) zoomed view of single layer. Reproduced from [29].

A novel design of low-temperature flue-gas heat exchanger with micro pipe array was proposed in the work of Yang et al [29]. Experimental work in a practical cold environment showed that the heat exchanger integrated with a micro heat pipe array had a higher thermal efficiency than traditional heat exchangers. The internal dimensions and the integrated structure of the micro heat pipe array is presented in Figure 1.6.

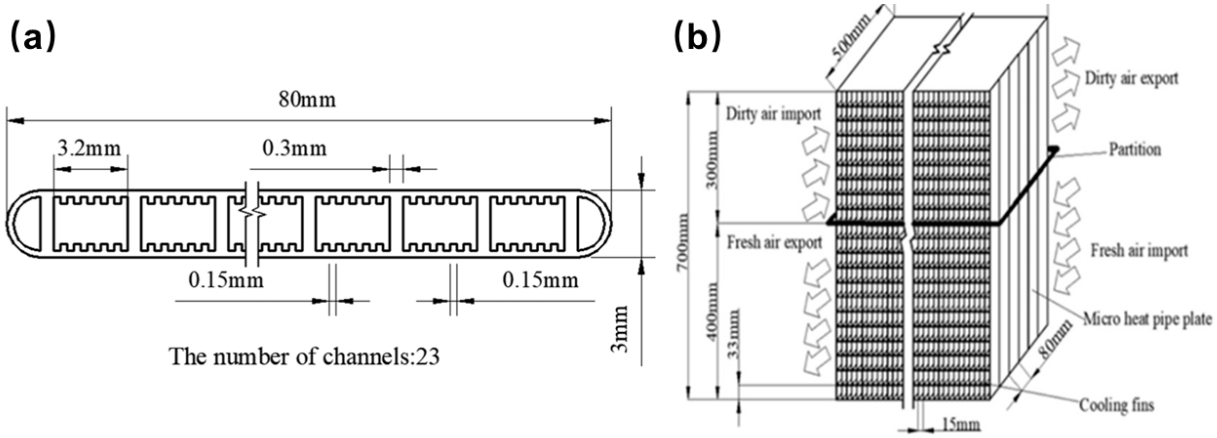

Figure 1.6. (a) Internal dimension of the microtube and (b) the sketch of the structure of micro heat pipe array. Reproduced from [29].

1.3 Scale effects in microsystems

The physical properties in micro systems are quite different from the macro systems. A classic example that demonstrates the difference of the physical behavior between micro and macro-scale

can be illustrated by means of the very first manufactured micro-motor [3]. It was discovered that for this application the frictional force at the microscale does not obey traditional frictional laws. Friction was proportional to the contact surface area between the micro-motor and the substrate instead of the applied normal force [5]. In general, when the scales are reduced, such as in the case of MEMS, the surface forces begin to be preponderant in respect to the body forces. Body forces are proportional to the third power of the characteristic length of the system, while surface forces rely on the first power or the second power of the length. Therefore, the surface-to-volume forces ratio is inversely proportional to the length scale of the system, thus having a big impact at the microscale.

1.4 Gas micro flows

In gas microflows, the gas can be in a state of rarefaction. Rarefaction increases when the scale of the microsystem is reduced and this effect will influence the macroscopic thermodynamic and kinematic properties of the gas flow. If the gas is rarefied, local thermodynamic disequilibrium will appear in the flow due to a low number of intermolecular collisions in respect to molecular collisions with the surfaces bounding the flow. Most of the applications that work with micro gas flows, relate to the slip flow rarefaction regime (low rarefaction). In this rarefaction regime, one can observe an evident thermodynamic non-equilibrium state of the gas in the vicinity of the walls. This produces a macroscopic velocity slip and temperature jump at the wall [30]. These rarefaction effects dramatically affect the mass and heat transfer at the micro scale, hence, an accurate modeling of the thermodynamic disequilibrium at the wall is vital for an accurate prediction of the mass flow rates and heat fluxes within the microdevice in order to improve the energy efficiency or optimize the energy consumption of such devices (rarefaction will be treated in more details in Chapter 2).

1.5 The motivation of this thesis

It is necessary to realize experimental observations on the rarefaction effects in order to verify the theoretical and numerical models of the boundary conditions proposed in the literature [31]. However, it is still a challenge to provide accurate local measurements on velocity and temperature distributions in gas microflows [32]. Most of the experimental analyses available in the literature

in channels are carried out by measuring global quantities, such as the mass flow rate, inlet and outlet pressures, and temperatures, which can only indirectly quantify the effects given by the velocity slip and temperature jump at the wall [33; 34].

To the best of our knowledge, there is not enough available experimental data on local velocity fields in the vicinity of the wall for confined microflows. The objective of this thesis was to obtain local velocity measurements for the case of confined rarefied gas flows. The Molecular Tagging Velocimetry (MTV) technique is based. The technique is based on a well-known photo-luminescent phenomenon: the flow is seeded with molecules at the vapor state which can absorb and re-emit light (fluorescence and phosphorescence). A comparison between the initial tagged line and the distorted line allows determining the displacement of the molecules in space and thus reconstructing a velocity profile.

The MTV technique has been successfully implemented for velocity measurements in a millimetric channel at low pressures [35]. These thermodynamic conditions corresponded to slight slip regime. However, low pressures are a source of higher molecular diffusion, which prevents computing experimental velocity profiles by simply dividing the displacement profile by the time of flight of the molecules. It was demonstrated that for higher pressures (continuum regime) velocity profiles can be correctly obtained through a reconstruction method which is based on the advection diffusion equation [36; 37]. Nevertheless, the reconstruction method has failed up to now to retrieve correct velocity profiles at low pressures. One source of great uncertainty for what concerns the correct application of the reconstruction method relies on knowing the correct values of diffusion coefficient at the required pressure, unfortunately, there is no clear consensus in the literature on the kinetic diameter values for the most common tracers, therefore calculating correct diffusion coefficients from the Chapman-Enskog equation can be troublesome. Motivated by this practical necessity, experimental work was conducted to measure the diffusion coefficient of acetone at low pressures. Moreover, measurements of velocity profiles by using the measured diffusion coefficients will be presented. The measurements were obtained for microflows in a newly fabricated millimetric channel which improved the previous one in terms of better control on the internal section geometries and dimensions and a leakage-free environment.

1.6 Structure of the thesis

The content of this thesis is organized into six chapters.

In chapter 2, the mathematical model, used to evaluate the experimental data, was mainly discussed. In this chapter, the definition of the important terms was described, such as dilute gas, collisions, mean free path, and rarefaction effect. Then, the analytical solution of rarefied Poiseuille flow were mainly discussed, considering different boundary conditions, and confined environment. Finally, the theoretical discussion on flow of gas mixture and diffusion effect was proposed.

Chapter 3 mainly reviewed the state of art of the molecular tagging velocimetry technique. A relatively comprehensive comparison between MTV technique and other popular velocimetry technique was presented in order to further explain why MTV technique is the most suitable technique for the specific need in this work. Then, the mechanism of molecular tagging and latest state of MTV application was debated.

In chapter 4, the experimental and post-processing methodology, and results of diffusion measurement of acetone vapor were mainly proposed. In this chapter, the necessity of this study was firstly introduced and the advantage of molecular tagging technique for this specific target was also reviewed. Later, the experimental setup and data treatment method were presented in detail. While dealing with the measured results, there are several important evolution parameters to be considered, the characteristic of photoluminescence of gaseous acetone, the mechanism of laser excitation, the quality of the image and curve fitting.

Chapter 5 mainly presents the experimental methodology and results of applying MTV technique to a novel channel at low pressure. The specific gas circuit and experimental methodology for MTV application was introduced at the commence. The post-processing method was improved while working with a novel transparent channel, especially the channel size measurement and channel wall detection method. The three-dimensional numerical simulation of the rarefied gas flow along the whole channel was conducted.

Chapter 6 summarized and evaluated all the work presented in this thesis. The direction and future work for further improvement of applying MTV work for rarefied gas flow were also discussed.

Chapter 2 Mathematical models of rarefied gas flow

2.1 Dilute gas

For the purpose of this thesis, it is of great interest to discuss the properties of gas at the molecular scale since for specific thermodynamic conditions, the gas might be considered as rarefied. This happens predominantly for gas flows at the microscale and at low-pressure. It is thus necessary to introduce several important microscopic characteristic lengths, such as the mean molecular or kinetic diameter d, the mean molecular spacing δ, and the mean free path λ [6; 30] (Figure 2.1).

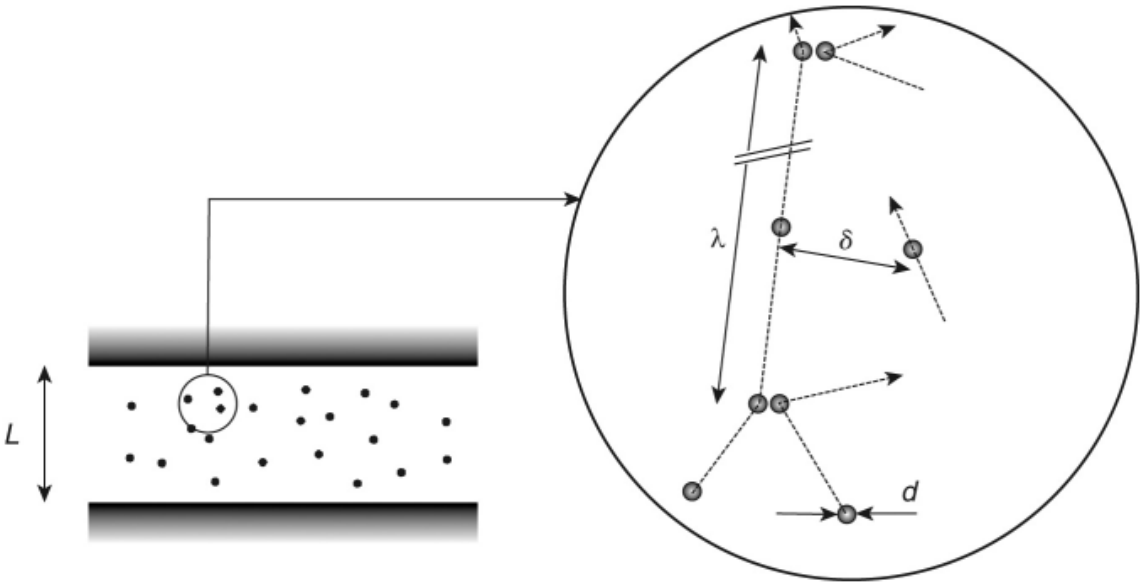

Figure 2.1. Semantics of the classical characteristic length scales at the molecular level. Figure from Colin *et al.* [1].

The number density n refers to the number of molecules per unit volume. The number density is dependent on the pressure and temperature, however independent of the composition of the gas [38]. The inverse $1/n$ can represent the average volume available for one single molecule. Therefore, the mean molecular spacing δ is defined as:

$$\delta = \frac{1}{\sqrt[3]{n}} . \tag{2.1}$$

A gas is thus in dilute conditions when the mean molecular spacing is much larger than the molecular diameter:

$$d \ll \delta . \tag{2.2}$$

On the contrary, if Eq.(2.2) is not satisfied, the medium can be considered as a dense gas.

The mean free path can be defined as the average distance that a molecule travels between two successive collisions. Mean free path and collision frequency are two important parameters to define the spatial and temporal scales of the intermolecular collision effects, when associated with number density, mass, size, velocity, and internal sate of each molecule. Mean free path is also a key parameter to describe the rarefaction effect.

A dilute gas can be described also via macroscopic thermodynamic parameters and its thermodynamic state is defined by the ideal gas state equation [6],

$$p = nk_B T , \tag{2.3}$$

where p is the absolute pressure, T is the thermodynamic temperature and k_B is the Boltzmann constant.

2.2 Intermolecular collisions

Based on Eq. (2.2), the distance between two adjacent molecules is significantly large in a dilute gas. Generally, the intermolecular forces can be neglected [6]. The motion of molecules can be characterized by constant velocity on straight trajectories. A binary intermolecular collision takes place when a molecule enters the cross-section zone of another molecule. In a dilute gas, the main form of intermolecular interactions is a binary elastic collision [6; 38-40]. The reason why intermolecular collisions are 'binary' is that the collision always happens between two molecules instead of ternary collisions (three-body collisions) in a dilute gas. An elastic collision means that there is no exchange of internal or translational energy caused by chemical reactions [6; 38]. The only possible energy exchange relates to kinetic energy. The mass, momentum and energy conservation equations are used to calculate the intermolecular collision dynamics in a dilute gas.

The definition of the mean free path is also dependent on the choice of the collision model. The mean free path can be defined as the ratio of the mean thermal velocity magnitude $\overline{c'}$ to the collision rate v_{rate},

$$\lambda = \frac{\bar{c'}}{v_{rate}} = \frac{\sqrt{\frac{8R_S T}{\pi}}}{v_{rate}} \,. \tag{2.4}$$

The mean thermal velocity magnitude is the average value of the molecular thermal velocity c', which is defined as the difference between the total velocity c and bulk macroscopical velocity u of the flow.

Different molecular models have been introduced in the literature in order to describe the electromagnetic potential of molecules for the purpose of correctly computing molecular collisions. The action of the molecular potential on other molecules can be translated via a force F which is repulsive for small distances and attractive for large distances. The real physical behavior of this force is of a complex nature, where its value for some models is defined as a function of the distance between molecules. The most used collision models are inverse power law (IPL), hard-sphere (HS), variable hard-sphere (VHS), variable soft-sphere (VSS) and Lennard-Jones (L-J).

For example, the inverse power law (IPL) model is a classic collision model, which is also called the center point of repulsion model. Only the repulsive component of the force F is considered in this model, which can be expressed by:

$$F = \frac{\kappa}{r^{\eta}}, \tag{2.5}$$

where r represents the distance between the center of two molecules, κ and η are constant values indicating that the force is inversely proportional to the intramolecular distance with a constant power. The collision model can also define the dynamic viscosity μ, which is a function of temperature, mean molecular diameter and the total collision cross-section $\sigma_T = \pi d^2$ in the collision plane.

A specific case of the IPL model is the hard sphere model, which is the simplest collision model. HS considers the molecular interaction as a purely elastic collision when two molecules are in contact with one another, that is when the distance between the centers of the two molecules is equal to the molecular diameter. For this specific case, η tends to infinity in Eq. (2.5).

Although the HS model can simplify the mathematical issue, in real gas, the collision cross section is inversely proportional to the relative velocity c_r between two colliding molecules [39; 40]. Bird [38] proposed a variable hard sphere model which partially solved this issue, since via this model the molecular diameter becomes a function of the relative molecular velocity. In order to improve the HS model and VHS model, Koura and Matsumoto [41; 42] proposed the variable

soft sphere model. The VSS model considered the variation in diameter for gas mixtures and the essential role of diffusion. The implementation of the VHS model is quite complex. Some models can include a long-range attractive component of the force at large distances between two molecules via combining a repulsive/attractive potential, such as the Lennard-Jones potential.

A second specific case of the IPL model is the Maxwell molecules (MM) model ($\eta = 5$). In MM model, the collision frequency is not dependent on c_r. However, the viscosity in MM model has a linear relationship with temperature, which is not realistic. Due to this unrealistic characteristic, the MM model has notable limitations [40]. Table 2.1 summarizes key coefficients in several classic IPL models.

Table 2.1 Force F, dynamic viscosity μ, collision rate ν_{rate}, and mean free path λ for classic IPL collision models. Adjusting parameter α is introduced for the VSS model and dependent on the gas species.

IPL model	η	ω	k_ν	k_λ
Hard Sphere (HS)	∞	$\frac{1}{2}$	$\frac{5}{4}$	$\frac{16}{5\sqrt{2\pi}} \cong 1.277$
Variable Hard Sphere (VHS)	η	$\frac{\eta+3}{2(\eta-1)}$	$\frac{30}{(7-2\omega)(5-2\omega)}$	$\frac{2(7-2\omega)(5-2\omega)}{15\sqrt{2\pi}}$
Maxwell molecules (MM)	5	1	2	$\sqrt{\frac{2}{\pi}} \cong 0.7979$
Variable Soft Sphere (VSS)	η	$\frac{\eta+3}{2(\eta-1)}$	$\frac{5(\alpha+1)(\alpha+2)}{\alpha(7-2\omega)(5-2\omega)}$	$\frac{4\alpha(7-2\omega)(5-2\omega)}{5(\alpha+1)(\alpha+2)\sqrt{2\pi}}$

Once the molecular model has been defined, some transport parameters of the flow can be computed, such as the dynamic viscosity, which is a function of temperature

$$\mu = \mu_0 \left(\frac{T}{T_0}\right)^{\omega}, \tag{2.6}$$

where ω is a parameter that depends on the molecular model, e.g., $\omega = 1$ for the MM model and $\omega = 0.5$ for the HS model, and μ_0 is the gas viscosity at reference temperature T_0.

To conclude, both the mean free path and the collision rate can be expressed through macroscopic thermodynamic quantities, such as

$$\lambda = k_\lambda \frac{\mu\sqrt{R_s T}}{p}, \tag{2.7}$$

$$\nu_{rate} = k_\nu \frac{p}{\mu}, \tag{2.8}$$

where k_λ is the mean free path coefficient and k_ν is the collision rate coefficient and both coefficients depend on the molecular model used.

2.3 Gas-surface collisions

The interaction between gas molecules and body surfaces gives rise to the drag, the lift, the force moment, and the heat transfer between the gas flow and the body surface [40].

Several gas-surface interaction models were proposed to describe the molecular motion a posteriori of a collision with a solid surface. One of the most popular and classic gas-surface interaction models is the one proposed by Maxwell [43]. In this model, the reflection of incident molecules on the solid body surface is modeled as an elastic sphere reflecting on an entirely elastic surface (Figure 2.2). In this context, Maxwell assumed that there were two limit cases of gas-wall interactions: the specular reflection and the diffuse reflection.

The specular reflection of molecules is much like a light ray reflecting on a mirror (Figure 2.2(a)). Only the normal component (to the surface) of related velocity reverses its direction. The molecular velocity vector intensity does not change, only its sign is changed to the opposite, which represents a change in direction normal to the wall. The components of the relative velocity parallel to the solid surface do not change, that is no tangential momentum exchange takes place between the molecules and the solid surface. For this case, also the total energy exchange between the molecules and solid surface equals zero. The specular reflection condition is an unrealistic assumption for industrial applications.

The complete diffuse reflection, so-called diffuse reflection with full accommodation, assumes that statistically the molecules leave the surface with the same tangential momentum accommodation coefficient of the solid surface (Figure 2.2(b)). The latter case scenario of diffuse accommodation at the wall is a more probable assumption for gas/surface interactions than the specular one.

The Maxwellian gas/surface interaction model (Maxwellian kernel), allows all possible configurations between specular and diffuse reflection. The tangential accommodation momentum coefficient (TMAC or σ_{TMAC}) translates the different possible states of gas/surface interactions, being σ_{TMAC} = 1 a full diffuse interaction at the wall, while σ_{TMAC} = 0 a full specular one. The values are dependent on the surface roughness, the surface material, and the gas molecular

structure [39]. If the TMAC value is in between 0 and 1, only a fraction $(1 - \sigma_{TMAC})$ of molecules are reflected secularly from the surface.

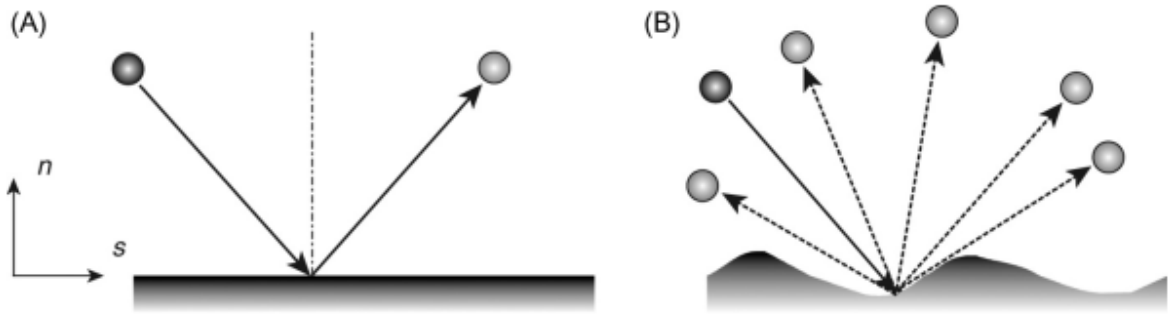

Figure 2.2. Schematic of (a) specular and (b) diffusive reflection of a molecule on a solid body surface. Figure from Colin *et al.* [6].

2.4 Rarefaction effects

In gas microfluidics, when the characteristic length of the device is of the same order of magnitude of the mean free path of the gas, rarefaction effects can modify substantially the kinematic and thermodynamic fields of the gas flow in respect to continuum gas flows [39]. Rarefaction effects can also be found at high altitude due to decreased atmospheric density (low pressure), e.g. rarefaction models are typically used to simulate atmospheric re-entry of space vehicles [44].

The continuum model assumption, also known as macroscopic model, assumes that a gas can be considered as a continuous medium. If rarefaction is strong, the continuum model can fail, and a molecular model is needed to describe the gas flow. The continuum assumption disregards the molecular discontinuities of matter and thus averages microscopic properties over a small sampling volume. In classic fluid mechanics, the variations of all macroscopic quantities, such as velocity, pressure, temperature, density (ρ) , are considered to be continuous from point to point within the flow domain.

For satisfying the continuum medium assumption, the averaged macroscopic parameters should be not affected by microscopic fluctuations within the small sampling volume. As a result, the size of the sampling volume should be large enough in order to eliminate microscopic fluctuations, and small enough to identify the important macroscopic variations, like velocity and pressure gradients (Figure 2.3).

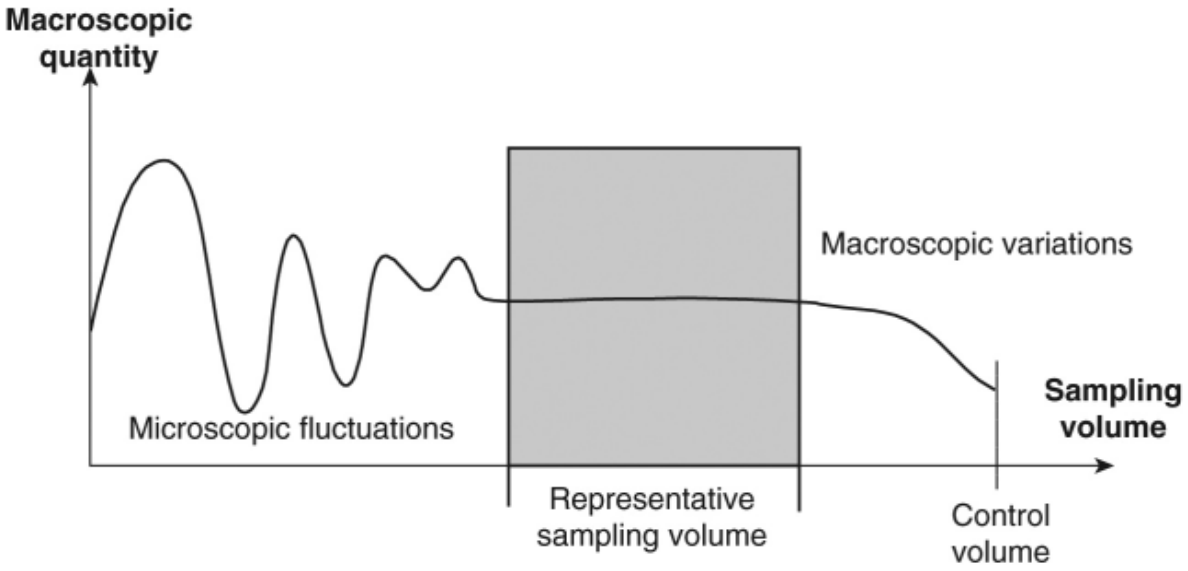

Figure 2.3. The dependence of the validity of the continuum assumption on the presence of a balanced representative sampling volume (shaded middle ground zone). Figure from Kandlikar *et al.* [39].

Inside the sampling volume, the gas is considered to be in thermodynamic equilibrium, this is achieved if the molecular collision frequency is high in respect to the perturbations of the flow. In this case, the characteristic time of intermolecular collisions ($\tau \propto 1/\nu_{rate}$) needs to be smaller than the macroscopic characteristics times of the gas flows. As defined by Eq. (2.4), the collision frequency (or characteristic time of collision) is directly related to the mean free path of the gas, thus the rarefaction regime of the medium can be obtained by comparing this parameter to the characteristic length of the sampling volume. Therefore, the non-dimensional parameter Knudsen number Kn, which is defined as the ratio of the molecular mean free path (λ) and the characteristic length of the system (L_C)

$$Kn = \frac{\lambda}{L_C} \ll 1\,, \tag{2.9}$$

can gives us a quantification of the rarefaction effect. Rarefied flows have a preponderant transmission of kinematic or thermodynamic information through gas/surface collisions rather than via intermolecular collisions. These flows are thus characterized mainly by having a momentum or thermodynamic disequilibrium in the proximities of the walls.

Let us add, that as expressed by Eq. (2.7), the mean free path λ is affected by the thermodynamic conditions in the flow, thus by modifying pressure and temperature one can affect

the rarefaction regime in devices that have relatively large dimensions. The rarefaction regimes can be classified as follows [30] (Figure 2.4):

i. Continuum (hydrodynamic) regime (Kn < 0.001)

The gas can be considered as a continuum medium and the flow can be modeled via the Navier-Stokes-Fourier equations by imposing classical no-slip boundary conditions.

ii. Slip flow regime (0.001 < Kn < 0.1)

In this moderate rarefied regime, the classical continuum assumptions hold. The Navier-Stokes-Fourier equations can be used if accompanied by the appropriate velocity-slip and temperature-jump boundary conditions at the walls.

iii. Transitional regime (0.1 < Kn < 10)

The continuum assumptions are invalid. A statistical molecular description is needed for simulating the gas flow, such as the Boltzmann equation, kinetic models, or direct simulation Monte Carlo (DSMC). In this regime, intermolecular collisions are still to be considered.

iv. Free molecular regime (Kn > 10)

This is the highest level of rarefaction achievable. Intermolecular collisions are negligible in respect to gas/surface collisions. Modeling a gas flow in free molecular regime is rather simple, since there is no need to consider intermolecular collisions.

In classic microsystems, gas flows are often in the slip flow regime or early transition regime, which corresponds to the Knudsen number ranging from 0.001 to 0.1 [39; 45]. Analytical or semi-analytical models can be used to represent these rarefied gas flows in simple geometries.

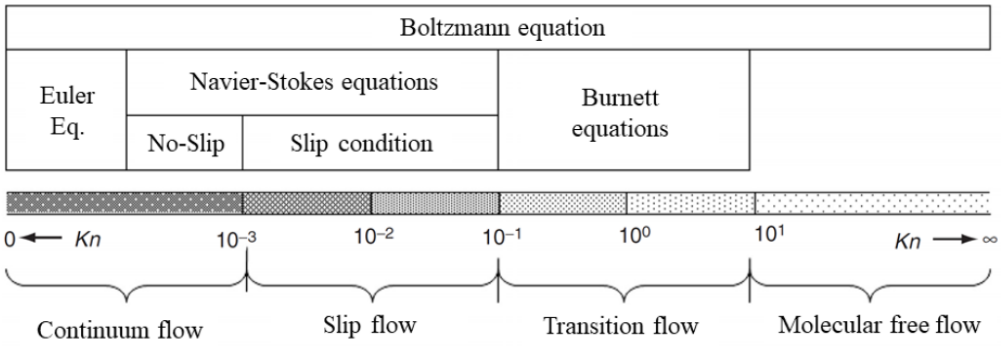

Figure 2.4. Flow regimes and corresponding mathematical models as a function of the Knudsen number. Figure from Agrawal *et al.* [46].

2.5 Slip regime boundary conditions

When the gas is rarefied, molecular collisions at the wall are preponderant in respect of intermolecular collisions at the bulk of the flow, thus thermodynamic and kinematic disequilibrium phenomena arise on the wall. These effects significantly affect the macroscopic velocity and temperature distributions of the flow. Two dominant effects take place: velocity-slip and temperature-jump at the wall. These effects are significantly dependent on the nature of the wall and the characteristics of the gas molecules. Let us underline that no matter the level of rarefaction of the flow, a local thermodynamic disequilibrium region always exists in the proximities of the wall (Knudsen layer). The thickness of the Knudsen layer (KL) is on the order of the mean free path. These effects can be neglected when the mean free path is small in respect to the characteristic length of the device, while they must be considered when the depth of the KL is of the same order of magnitude of the device. In slip regime, velocity slip and temperature jump near the wall can be described by modifying the classic NS boundary conditions. A general definition of the first order boundary condition that describes velocity slip at the wall for isothermal flows can be expressed as

$$u_{\text{slip}} = u_{\text{s}} - u_{\text{wall}} = \xi \left.\frac{\partial u_{\text{s}}}{\partial n}\right|_{\text{w}}, \tag{2.10}$$

where u_{slip} represents the slip velocity, u_{s} is velocity of the gas flow, u_{wall} is the velocity of the wall, the index s represents the direction tangent to the wall, while n represents the direction normal to the wall, and ξ represents the velocity slip length or the so-called coefficient of slip [39; 45]. Knudsen layer and slip velocity are illustrated in Figure 2.5, u_{gas} represents the real velocity of the gas flow at the wall, u_s represents the gas velocity out of the Knudsen layer. The velocity difference $\left(u_{\text{gas}} - u_{\text{wall}}\right)$ does not correspond to the slip velocity. In the general assumption, slip velocity represents the virtual velocity for accurately predicting the velocity distribution outside the Knudsen layer.

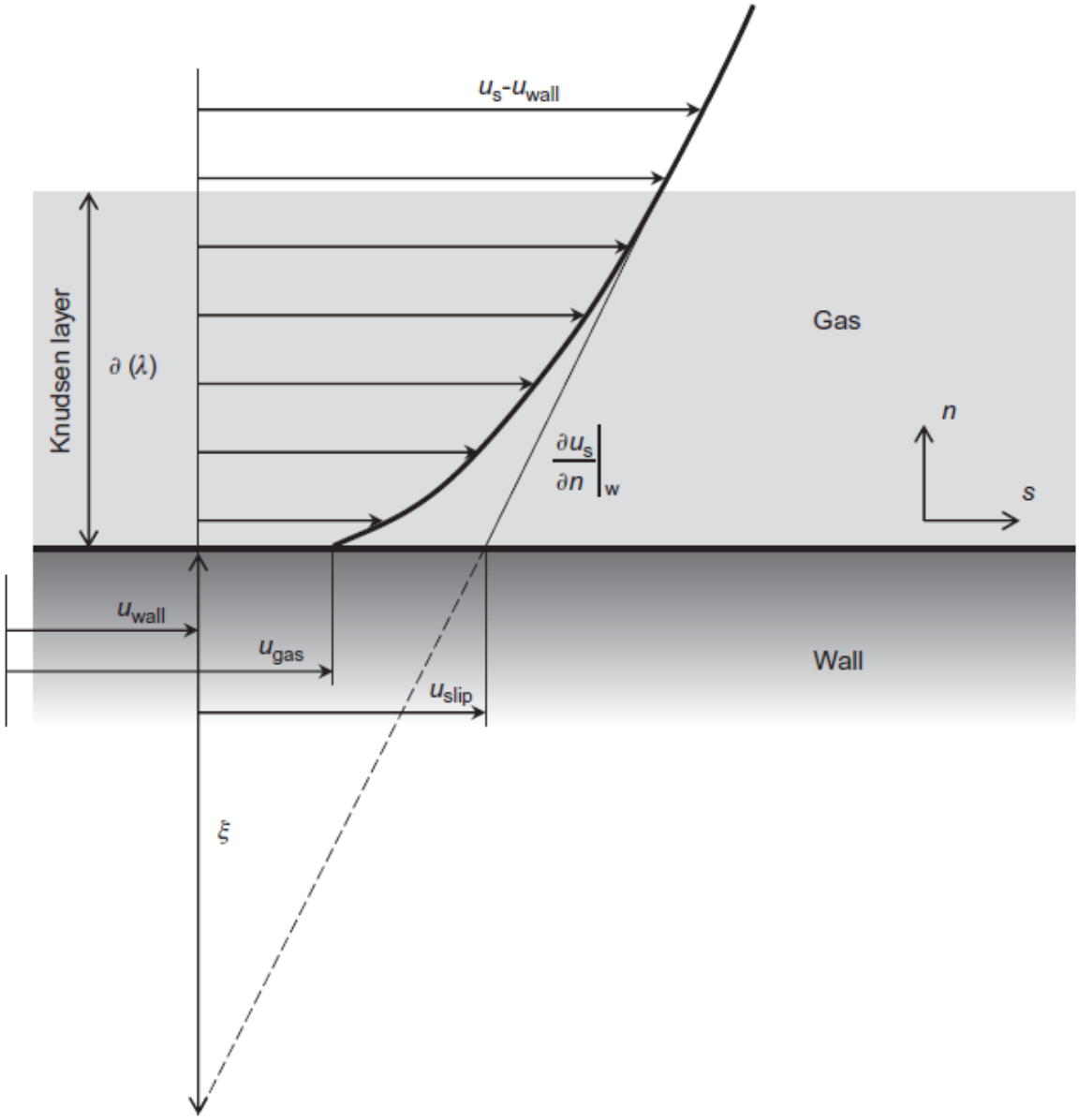

Figure 2.5. Schematic for structure of Knudsen layer, and slip velocity near the wall. Figure from Kandlikar *et al.*[39].

The velocity slip length can be defined as

$$\xi = \beta_{u1} \frac{2 - \sigma_{TMAC}}{\sigma_{TMAC}} \lambda \,, \tag{2.11}$$

where σ_{TMAC} is the tangential accommodation coefficient (Section 2.3) and β_{u1} is a corrective coefficient, which is added for a precise description of velocity distribution out of the Knudsen layer based on the numerical work of Cercignani et al. [47]. Unlike the initial model proposed by Maxwell, β_{u1} has a minor deviation from unity. The value of β_{u1} is dependent on the choice of

mean free path coefficient, which has various values (Table 2.1). First-order boundary conditions are adequate for the slip flow regime (Kn < 0.1).

Higher-order boundary conditions are necessary for rarefaction regimes at higher Kn. A general form of the second order slip boundary conditions can be expressed by:

$$u_{\text{slip}} = u_s - u_{wall} = C_1 Kn \left[\frac{\partial u_s}{\partial n}\right]_w - C_2 Kn^2 \left[\frac{\partial^2 u_s}{\partial \text{n}}\right]_w , \qquad (2.12)$$

where the values of C_1 and C_2 have been obtained in the literature via analytical, numerical, and experimental approaches (Table 2.2). Let us point out that there is still no general consensus on the value of the second-order term C_2.

Table 2.2 Slip coefficients acquired via different methods for main models for second-order boundary condition ($\sigma_{TMAC} = 1$).

References (Author, year)	C_1	C_2
Maxwell, 1879 [43]	1	0
Schamberg, 1947 [48]	1	-5π/12
Chapman and Cowling, 1952 [49]	$\kappa_0 (\approx 1)$	$\kappa_0^2/2 (\approx 1/2)$
Deissler, 1964 [50]	1	-9/8
Cercignani, 1964 [51]	1.1466	-0.9756
Hsia and Domoto, 1983 [52]	1	-1/2
Mitsuya ,1993 [53]	1	-2/9
Karniadakis and Beskok, 2002 [48]	1	1/2
Hadjiconstantinou, 2003 [54]	1.11	-0.61
Pitakarnnop et al., 2010 [33]	1.1466	-0.647
Cercignani and Lorenzani, 2010 [55]	1.1209	-0.2347
Lorenzani, 2011 [56]	1.1366	-0.69261

2.6 Analytical solutions of pressure driven flow in slip regime

Hereafter two Poiseuille flow analytical solutions are described. These solutions are used in this work for comparison against the experimental results produced. It is possible to obtain analytical solutions of pressure driven gas flows in simple geometries by solving the system of fundamental equations of conservation of mass, conservation of momentum (Navier-Stokes equation) coupled to the modified boundary conditions for slip flow and the ideal gas equation of state. In the following analytical description, the pressure-driven flow is assumed as laminar, steady, isothermal, and fully developed. The schematic of the channel geometry is sketched in

Figure 2.6. In Figure 2.6, H is the channel height, b is the channel width, L is the channel length. The axis of the channel is represented by coordinate x axis, and the cross-sectional plane lies in the (y,z) plane.

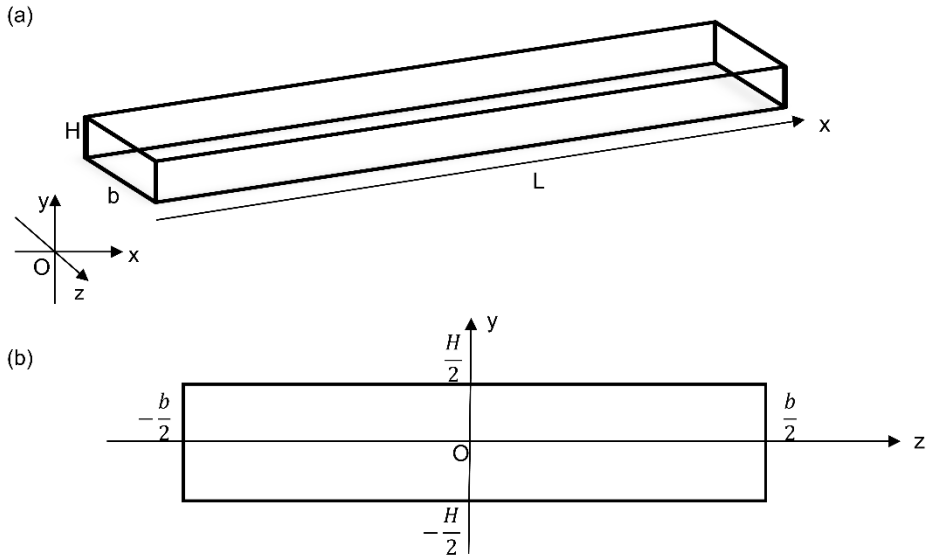

Figure 2.6. Channel geometry sketch. The Cartesian coordinates systems for the channel (a) and cross-section (b).

The Knudsen number in this thesis is defined as the mean free path over the minimal characteristic length

$$K_n = \frac{\lambda}{L_{C,min}} = \frac{\lambda}{H}. \tag{2.13}$$

2.6.1 Poiseuille flow between two parallel flat plates

The flow through a rectangular channel can be considered as a planar Poiseuille flow between two infinite parallel plates if the aspect ratio ($a = H/b$) of the cross-section of the microchannel is sufficiently small (b $\gg$ H). For this case, the conservation of momentum expression can be simplified as

$$\frac{\mathrm{d}^2 u}{\mathrm{d}y^2} = \frac{1}{\mu}\frac{\mathrm{d}p}{\mathrm{d}x}\ . \tag{2.14}$$

By using the second-order boundary condition (Eq.(2.12)), and the condition of symmetry on the axis of the flow, the dimensionless solution of the velocity profile is

$$u^* = 1 - 4{y^*}^2 + 4C_1\mathrm{Kn} + 8C_2\mathrm{Kn}^2,$$

where the non-dimensional quantities are defined as

$$y^* = \frac{y}{H} \in \left[-\frac{1}{2}, \frac{1}{2}\right]$$
$$u^* = \frac{u}{u_{cp}}, \tag{2.15}$$

being $u_{cp} = -\frac{H^2}{8\mu}\frac{dp}{dx}$ the centerline velocity of Poiseuille flow in the case of flow in hydrodynamic regime (no-slip). Figure 2.7 illustrates different velocity profile solutions by changing the values of C_1 and C_2 [57].

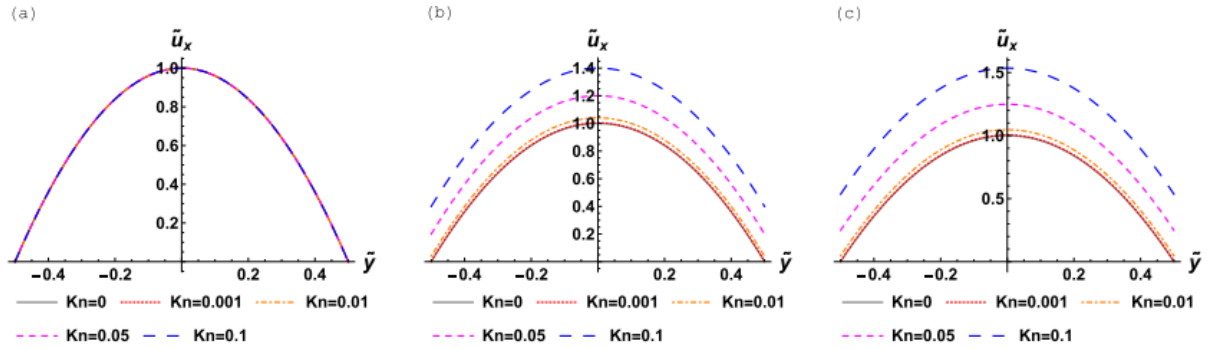

Figure 2.7. Normalized velocity profile of planar Poiseuille flow at different Knudsen number with different slip boundary conditions (Eq.(2.19)). (a) No-slip boundary condition ($C_1 = C_2 = 0$), (b) First-order slip boundary condition ($C_1 = 1$, $C_2 = 0$, Maxwell [58]), (c) Second-order slip boundary condition ($C_1 = 1.1466$, $C_2 = 0.9576$, Cercignani [51]). Figures from Silva *et al.* [57].

From the velocity profile solution, it is thus possible to obtain the mass flow rate expression

$$\dot{m} = A\bar{u}(x)\rho(x) = -\frac{bH^3}{8\mu}\frac{dp}{dx}\frac{p}{RT}\left[\frac{2}{3} + 4C_1Kn + 8C_2Kn^2\right], \tag{2.16}$$

where $A = bH$ represents the area of the cross-section. A more practical expression of $\dot{m}$ can be obtained by integrating Eq.(2.16) along the channel length. Since the mean free path is always inversely proportional to the pressure, it is possible to state that along the axis of the channel the quantity $Kn(x) \cdot p(x)$ remains constant, thus it is possible re-write the expression as a function of $Kn_{\text{out}} \cdot p_{\text{out}}$, which corresponds to values at the outlet of the channel. The integration can thus be expresses as

$$\dot{m} = \frac{1}{L}\int_0^L \dot{m}\mathrm{d}x = -\frac{bH^3}{8\mu L}\frac{1}{RT}\int_{p_{in}}^{p_{out}}\left(\left(\frac{2p}{3} + 4C_1Kn_{out}\,p_{out} + \frac{8C_2Kn_{out}^2p_{out}^2}{p}\right)\right)\mathrm{d}p. \tag{2.17}$$

And the dimensional and dimensionless solutions are:

$$\dot{m} = \frac{H^3 b}{8\mu L}\frac{p_{\text{out}}^2}{RT}\left(\frac{\Pi^2 - 1}{3} + 4C_1Kn_{\text{out}}(\Pi - 1) + 8C_2Kn_{\text{out}}^2\ln\Pi\right), \tag{2.18}$$

$$\dot{m}^* = \frac{\dot{m}}{\frac{H^3 b}{8\mu L}\frac{p_{out}^2}{RT}\left(\frac{\Pi^2-1}{3}\right)} = 1 + 12C_1 Kn_{out}\frac{1}{\Pi+1} + 24C_2 Kn_{out}^2 \frac{\ln\Pi}{\Pi^2-1}, \tag{2.19}$$

where $\Pi = p_{in}/p_{out}$ is the pressure ratio between the inlet and the outlet of the channel.

2.6.2 Poiseuille flow in a rectangular channel

For a rectangular channel with a higher aspect ratio ($a > 0.01$) the influence of the lateral walls becomes significant. Thus a three-dimensional rectangular channel model is needed since the axial velocity $u(y,z)$ depends both on the y and z position [30]. For this case, the momentum conservation equation can be expressed as:

$$\frac{d^2u}{dy^2} + \frac{d^2u}{dz^2} = \frac{1}{\mu}\frac{dp}{dx}, \tag{2.20}$$

and its dimensionless form as

$$a^2\frac{\partial^2 u^*}{\partial y^{*2}} + \frac{\partial^2 u^*}{\partial z^{*2}} = -1, \tag{2.21}$$

where the dimensionless variables are defined as

$$y^* = \frac{y}{\frac{H}{2}}, z^* = \frac{z}{\frac{b}{2}}, u^* = \frac{u}{2u_{cp}}.$$

Consequently, the slip boundary conditions are to be applied on the lateral walls $z = \pm b/2$ and $y = \pm H/2$ in addition to the symmetric condition on the axis of the channel.

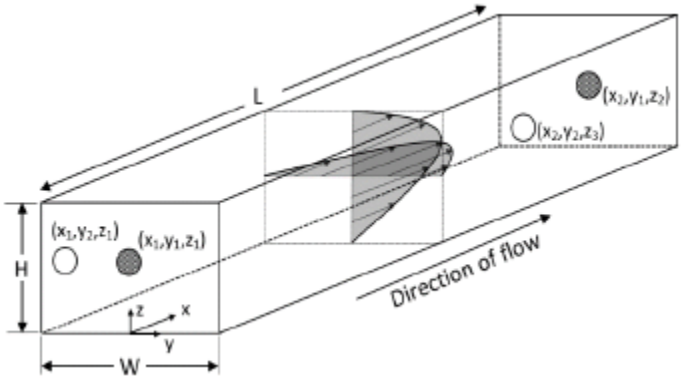

Figure 2.8. Double-parabolic velocity profile in a rectangular channel. Figure from Winer *et al.* [59].

Within a rectangular channel, the first-order boundary conditions can be expressed as:

$$u^*|_{y^*=1} = -\beta_{u1}\frac{2-\sigma_{TMAC}}{\sigma_{TMAC}} 2Kn \left.\frac{\partial u^*}{\partial y^*}\right|_{y^*=1}, \tag{2.22}$$

$$u^*|_{z^*=1} = -\beta_{u1}\frac{2-\sigma_{TMAC}}{\sigma_{TMAC}}2Kn'\left.\frac{\partial \mathrm{u}^*}{\partial z^*}\right|_{z^*=1}, \tag{2.23}$$

with the symmetric condition:

$$\left.\frac{\partial \mathrm{u}^*}{\partial y^*}\right|_{y^*=0} = 0, \tag{2.24}$$

$$\left.\frac{\partial \mathrm{u}^*}{\partial z^*}\right|_{z^*=0} = 0, \tag{2.25}$$

In the work of Ebert and Sparrow [60], a single Fourier series form of velocity distribution was proposed as :

$$u^*(y^*, z^*) = -\sum_{i=1}^{\infty} \Psi_i(z^*)\cos(\alpha_i y^*), \tag{2.26}$$

where α_i are a series of eigenvalues, and Ψ_i is a function of position z^*. In order to satisfy the slip boundary condition (Eq. (2.39) and (2.44)) and prevent the emergence of a trivial velocity solution, α_i and Ψ_i should satisfy the following equations:

$$\alpha_i \tan\ \alpha_i = \beta_{u1}\frac{\sigma_{TMAC}}{2-\sigma_{TMAC}}\frac{1}{2Kn}, \tag{2.27}$$

$$\sum_{i=1}^{\infty} \Psi_i(z^*)\left[\cos\left(\alpha_i\right) - 2\alpha_i\beta_{u1}\frac{2-\sigma_T}{\sigma_T}Kn\sin\ \alpha_i\right] = 0. \tag{2.28}$$

Based on Eq.(2.35) and Eq.(2.47), a solution of Ψ_i can be expressed as:

$$\Psi_i = -\frac{\Omega_i}{\alpha_i^2}\left(1 - \frac{\cosh\left(\frac{\alpha_i z^*}{a}\right)}{\cosh\left(\frac{\alpha_i}{a}\right) + 2\beta_{u1}\left(\frac{2-\sigma_T}{\sigma_T}\right)Kn\alpha_i\sinh\left(\frac{\alpha_i}{a}\right)}\right), \tag{2.29}$$

with

$$\Omega_i = \frac{2\sin\alpha_i}{\alpha_i + \sin\alpha_i\cos\alpha_i}. \tag{2.30}$$

From the work of Aubert and Colin [61], the second-order slip boundary conditions can be defined in a normalized expression:

$$u^*|_{y^*=1} = -\frac{2-\sigma_{\mathrm{TMAC}}}{\sigma_{\mathrm{TMAC}}}2\mathrm{Kn}\left.\frac{\partial u^*}{\partial y^*}\right|_{y^*=1} - \frac{9}{4}\mathrm{Kn}^2\left(a^2\left.\frac{\partial^2 u^*}{\partial y^{*2}}\right|_{y^*=1} - 1\right), \tag{2.31}$$

and

$$u^*|_{z^*=1} = -\frac{2-\sigma_{\mathrm{TMAC}}}{\sigma_{\mathrm{TMAC}}} 2a\mathrm{Kn}\left.\frac{\partial W^*}{\partial \mathrm{z}^*}\right|_{z^*=1} - \frac{9}{4}\mathrm{Kn}^2\left(\left.\frac{\partial^2 W^*}{\partial z^{*2}}\right|_{z^*=1} - 1\right) \tag{2.32}$$

Since the single Fourier series velocity distribution proposed by Ebert and Sparrow [60] does not satisfy the second-order boundary conditions. Based on the boundary conditions (Eq.(2.31), Eq.(2.32)), Aubert and Colin [61] proposed the double Fourier series normalized velocity distribution:

$$u^*(y^*, z^*) = \sum_{i,j=1}^{\infty} A_{ij}N_{ij}\cos\left(\varphi_i\frac{y^*}{a^*}\right)\cos(\psi_j z^*) + \frac{9}{4}Kn^2, \tag{2.33}$$

with

$$\begin{aligned}
&A_{ij}N_{ij} \\
&= \frac{1}{\varphi_i^2+\psi_j^2}\left\{\frac{4\sin(\varphi_i/a)\sin\psi_j}{\varphi_i\psi_j} + \frac{9}{22-\sigma}Kn\left(\frac{\sin(\varphi_i/\mathrm{a})\cos\psi_j}{\varphi_i} + \frac{\cos(\varphi_i/\mathrm{a})\sin\psi_j}{\psi_j}\right)\right\} \\
&\times\left\{\left(\frac{1}{\mathrm{a}} + \frac{\cos(\varphi_i/\mathrm{a})\sin(\varphi_i/\mathrm{a})}{\varphi_i}\right)\left(1 + \frac{\sin\psi_j\cos\psi_j}{\psi_j}\right)\right. \\
&+ \frac{9}{42-\sigma}Kn\left(\cos^2\psi_j\left[\frac{1}{a^*} + \frac{\cos(\varphi_i/\mathrm{a})\sin(\varphi_i/\mathrm{a})}{\varphi_i}\right]\right. \\
&\left.\left.+\cos^2\left(\frac{\varphi_i}{\mathrm{a}}\right)\left[1 + \frac{\sin\psi_j\cos\psi_j}{\psi_j}\right]\right)\right\}^{-1}.
\end{aligned} \tag{2.34}$$

In order to satisfy the second-order boundary conditions Eq.(2.31) and Eq.(2.32), and need to be the solutions of following equations:

$$1 - 2Kn\frac{(2-\sigma_{TMAC})}{\sigma_{TMAC}}\psi_j\tan\psi_j - \frac{9}{4}\mathrm{Kn}^2\psi_j^2 = 0, \tag{2.35}$$

and

$$1 - 2Kn\frac{(2-\sigma_{TMAC})}{\sigma_{TMAC}}\varphi_i\tan\frac{\varphi_i}{\mathrm{a}} - \frac{9}{4}Kn^2\varphi_i^2 = 0. \tag{2.36}$$

The velocity solution with second-order slip boundary conditions (Eq.(2.31) and Eq.(2.32)) are suitable for any aspect ratio.

The mass flow rate $\dot{m} = \iint_{(\Sigma)} u\rho$ through each cross-section can be defined by:

$$\dot{m} = \frac{bH^4p_{\mathrm{out}}^2}{4a\mu RTL}\left[\frac{a_1}{2}(\Pi^2-1) + a_2Kn_{out}(\Pi-1) + a_3Kn_{\mathrm{out}}^2\ln\Pi\right], \tag{2.37}$$

where the coefficients a_1, a_2, and a_3 are dependent on aspect ratio of the cross-section and σ_{TMAC}, whose values can be found in the references [39].

2.6.3 Compressibility and rarefaction effects on pressure distribution

The pressure distribution of rarefied gas flow in a channel can be significantly affected both by compressibility and rarefaction. In 1965, Ebert & Sparrow [60] emphasized the compressibility effect on the axial pressure drop. In their work, they proposed that compressibility can enhance pressure drop mostly via increasing the viscous shear instead of increasing the momentum flux. An analytical solution was derived with a first-order correction of wall slip also considering compressibility effect. Both in the work of Prud'homme *et al.* [62] in 1986 and Van den Berg [63] in 1993 proposed that compressibility has a significant effect on the pressure drop inside a channel, that is a nonconstant-pressure gradients exists, even without rarefaction effect. Also in 1993, Beskok and Karniadakis [64] proposed that rarefaction effect can simultaneously enhance the mass flow rate in the channel through slip and thermal creep effects. In 1997, Arkilic and co-authors [65] found that the effect of slip can lead to an increase in the observed mass flow with a decrease in pressure ratio. A novel solution of pressure distribution was proposed by Arkilic considering both rarefaction and compressibility effect.

However, the analytical solution proposed by Ebert & Sparrow and Arkilic *et al.* are quite sophisticated. In 2001, Aubert & Colin [61] propose a simpler mathematical approach to describe the pressure distribution along centerline of channel both considering compressibility and rarefaction effect. The dimensionless pressure distribution along x-axis can be described by the following polynomial equation:

$$p^{*2} + \alpha_1 p^* + \alpha_2 + \alpha_3 x^* = 0, \tag{2.38}$$

with normalized quantities

$$p^* = \frac{p}{p_{out}}, x^* = \frac{x}{L},$$

and parameters

$$\alpha_1 = 24\beta_{u1}\frac{2-\sigma_{TMAC}}{\sigma_{TMAC}}Kn_{out}; \alpha_2 = -\Pi(\Pi+\alpha_1); \alpha_3 = (\Pi-1)(\Pi+1+\alpha_1).$$

This solution enables the analysis of the separate effects on pressure distribution due to compressibility or rarefaction. Rarefaction and compressibility affects oppositely on the pressure distribution curves, higher rarefaction decrease the curvature in pressure distribution (Figure 2.8 left), while higher pressure ratios can increase the non-linearity (Figure 2.8 right) [39].

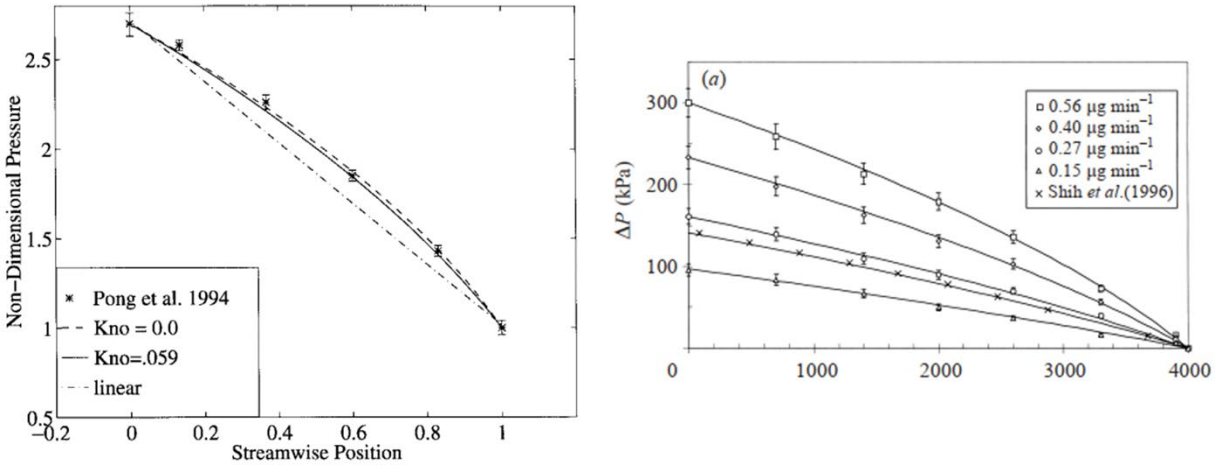

Figure 2.9. The effect of rarefaction (Left) and compressibility (Right) on pressure distribution along the centerline of a channel. Reproduced from [65] (Left) and [66] (Right).

In a conclusion, the actual pressure distribution along the channel axis shows a non-linear behavior (Figure 2.9). When evaluating pressure distribution in microchannels, both compressibility and rarefaction should be considered.

2.7 Conclusion

In this chapter, we have reviewed the present mathematical models to describe rarefied gas flows in microchannels. Firstly, we have discussed the importance of rarefaction effects in low-pressure and micro gas flow. The intermolecular collision models and the mean free path definition methods are discussed in details. The key part of this chapter is the slip boundary conditions and analytical solutions for gas flow in slip flow regime ($0.001 < Kn < 0.1$). The author also summarized and discussed analytical solutions considering different slip boundary conditions of velocity distribution, pressure distribution, and mass flow rates in a rectangular channel. In the next chapters, we will introduce a promising experimental technique which allows measurements of slip velocity near the wall.

Chapter 3 Molecular tagging velocimetry technique

The molecular tagging velocimetry technique (MTV) is an excellent tool to obtain local measurements of velocity, temperature, and pressure in confined gas flows. This chapter mainly introduces the state of art on MTV and more generally on optical velocimetry techniques devoted to gas micro flows.

3.1 Introduction to optical velocimetry techniques

The flow visualization measurement techniques can be separated mainly into intrusive and non-intrusive techniques. On the one hand, intrusive techniques induce a modification of the kinematic and thermodynamics parameters of the flow while performing the measurement, typical examples could be the pitot tube or hot-wire anemometers since these sensors inevitably bring a direct disturbance into the measured flow, like distortion and shockwaves [67]. This specificity can be considered as a major drawback for gas flows in micrometrical confined systems. On the other hand, less intrusive or non-intrusive techniques are able to offer local measurements with no direct interaction with the flow, such as laser diagnostics techniques [68], which comprehend particle image velocimetry (PIV) [69-71], Laser Doppler velocimetry (LDV) [72-74], and molecular tagging velocimetry (MTV) [75]. PIV and LDV reconstruct velocity fields from the measurement of the displacement of particles seeded in the flow, while MTV follows the displacement of fluorescent and phosphorescent gas molecules seeded in the flow. Since introducing solid particles in a confined gas micro flow can be consider as intrusive, the molecular tagging counterpart offers great advantages at this scale. The comparison between the main non-intrusive laser-based diagnostics techniques is summarized in Tab 3.1.

Table 3.1. The measurement properties comparison between μPIV, LDV, and μMTV technique.

Measurement technique	μPIV	μMTV	LDV
Tracers	Nano-sized particles	Molecules	Particles
Illuminated test section	Plane or volume	Line or grid	Single point
Measurement resolution definition parameters	Depth of the test section	Diameter of the laser beam	Diameter of the laser beam
Limitations	Difficulty in generating nano-sized particles, high background noise from particles out of focus or test section, highly sensitive to Brownian noise, unavoidable scattered light noise near the wall, difficulty in following the high-speed flow because of particle lag effects, particle sedimentation on the walls.	The resolution is limited to the minimum diameter of laser beam, the uncertainty brought by high molecular diffusion	Only averaged velocity at single point can be acquired. If velocity distribution are necessary, a complex optical system are necessary.
Advantages	Suitable for microliquid flow	Direct velocity measurement of the gas, avoid the limitations brought by seeding particles, Red-shift phenomenon, long luminescence lifetime	Strong light scattering signals

3.1.1 Particle image velocimetry

The velocity fields provided by the PIV technique correspond to velocity measurements realized on seeded tracer particles. The velocity measurements are obtained by optically acquiring a series of pictures which are taken at certain time intervals. An intense light source is necessary in order to have a sufficiently intense signal for the acquisition of the scattered light coming from the tracer particles, or to have an elevated contrast between dark particles and illuminated areas of the channel. The velocity vectors are deduced from the particle displacement over two sperate time intervals. The typical PIV experimental setup is illustrated in Figure 3.1. Usually, the test section is illuminated by a light sheet obtained from a laser source. The camera is positioned perpendicular to the sheet plane for signal acquisition purposes. Several other different configurations of this

technique have been proposed in the literature [18; 70; 71; 76]. At the micro-scale the technique is called micro particle image velocity (μPIV) [69].

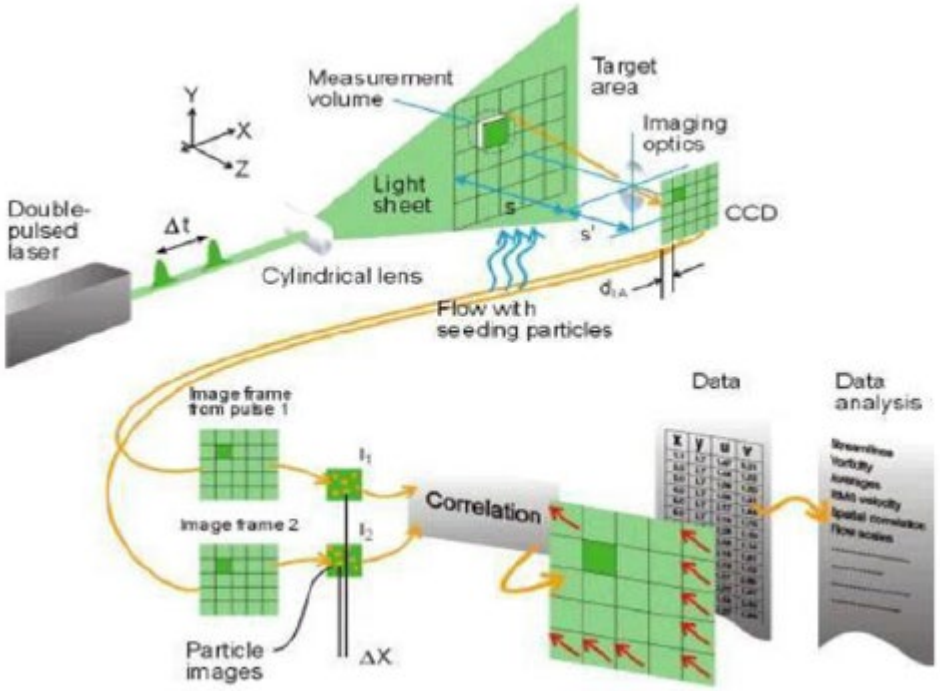

Figure 3.1. Typical PIV experimental arrangement. Reproduced from [77].

The main difficulty in respect to applying this technique to confined gas micro flows is related to the seeded particles themselves, which can i) modify the characteristics of the flow in such confined environments (particle diameter, particle concentration) and/or ii) insufficiently track the flow , e.g. rarefied gas flows [78]. The diameter of the particles should not be too big in order to follow the flow motion, and not too be small for avoiding Brownian motion and ensure the signal intensity of the light scattering [73]. Also, the light scattering near the wall is also a source of noise during acquisition [79], together with the uncertain behavior of particles in the near-the-wall region, making parameters such as the slip velocity at the wall of very difficult extraction. In order to obtain velocity fields in gas micro flows, the particle sizes should decrease to the order of hundreds of nanometers, which increase the difficulty of displacement acquisition and increase the

Brownian motion. Although μPIV has been widely applied in micro liquid flow [71; 76; 80], these limitations prevent its application to gas micro flows [45; 81; 82].

3.1.2 Laser doppler velocimetry

Contrarily to the PIV and MTV technique, the laser doppler velocimetry (LDV) technique can acquire velocity data just in a single point. As described in the previous section, the same limitations of seeding particles inside confined micro flows are to be considered also for this technique. In a typical LDV experimental setup, as shown in Figure 3.2, a fringe pattern with periodic bright and dark stripes is formed by two coherent continuous focused laser lights. The measured velocity is dependent on the spacing between two fringes and the frequency of the scattered light created by the seeding particles passing through the fringes [73].

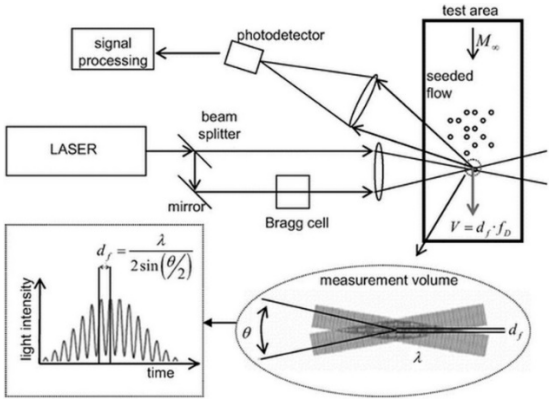

Figure 3.2. A schematic of the LDV experimental setup. Reproduced from [73].

Kerherve *et al.* [74] used the single-point and two-point LDV measurement to get the flow properties of a Mach 1.2 cold supersonic jet. The radial distribution of mean axial velocity was obtained by the single-point LDV. The two-point LDV measured the velocity correlation tensors. Even with a multi-point LDA measurement, it is not possible to measure a complete velocity profile or the local velocity near the wall. Matsunuma and coworker [83] used LDV technique to measure the temporal distribution of time-averaged relative velocity of unsteady gas flow with low Reynolds number near and in a turbine rotor, in order to understand the correlation between turbine stator wake and gas flow in the turbine rotor. Kyoden et al. [84] proposed a multipoint laser Doppler velocimetry (MLDV) system to measure the velocity distribution of blood flow in a

continuously expanding intersection region with high spatial and temporal resolution. The basic idea of velocity distribution measurement by MLDV is still based on single-point LDV. In order to accurately measure velocity at multi-points simultaneously, the system was based on a cross-sectional MLDV (CS-MLDV) [85] with a much complex and precise optical system, mainly including two laser sheets created by a complicated light transmission system and an array of optical fibers as multi receiving points (Figure 3.3). The main limitation of LDV other than the use of seeded particles, can be considered as the complexity introduced by the experimental setup and methodology.

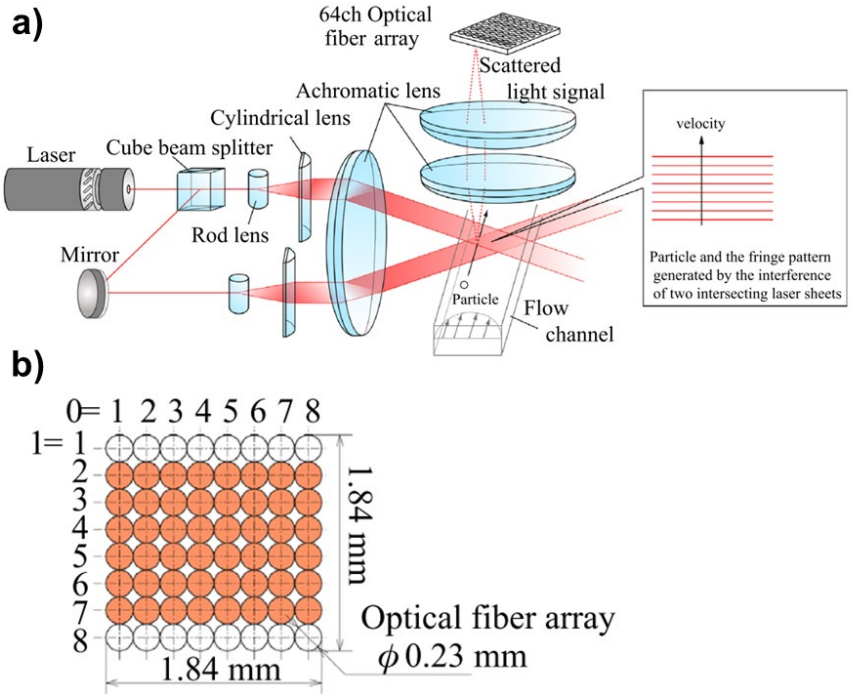

Figure 3.3. Sketch of CS-MLDV setup. (a) Isometric view and (b) the optical fiber array. Reproduced from [84; 85].

3.2 Molecular tagging velocimetry technique

The molecular tagging velocimetry technique is a non-intrusive quantitative velocity field measurement technique. It can be both applied to liquid and gas flows. It consists on acquiring the signal emitted by tracer molecules. The emitted light is obtained by exciting the tracer molecules

through a pulsed laser beam at a specific wavelength. The position of the molecular tracer is recorded at successive time intervals (Figure 3.4). The velocity vectors can be obtained through reconstruction algorithms.

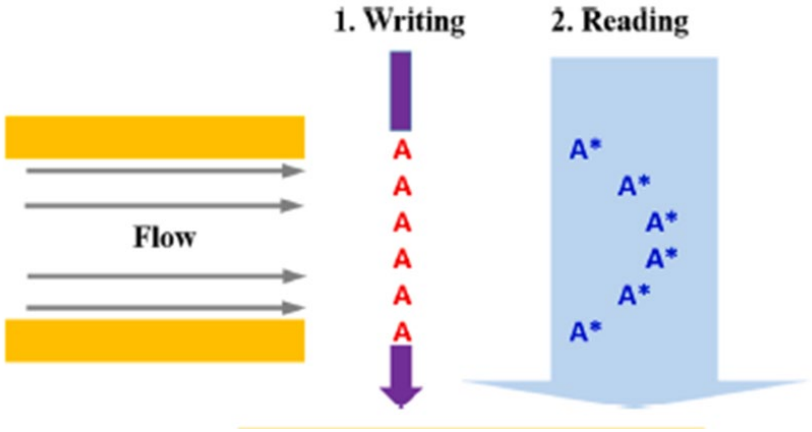

Figure 3.4. Molecular tagging velocimetry technique mechanism. Reproduced from [79].

This technique can be considered as the molecular counterpart of PIV [4; 86]. However, the molecular nature of the tracer overcomes the limitations encountered by seeding the flow with particles. Since µMTV is a molecular-based technique, the problem caused by the seeding particles in the flow tracking of µPIV or LDV are avoided. Another advantage is that the acquired photoluminescence signal has a different wavelength in respect to the laser shots used for excitation, which is the so-called red-shift phenomenon [79]. Making it thus easy to distinguish the laser induced fluorescence (LIF) or phosphorescence (LIP) in respect to noise generated by the incident laser source. For these reasons, MTV is one of the most promising techniques for measuring local velocity fields in confined flows at the micrometric scale. Different variants of MTV techniques exist:

- Direct phosphorescence MTV (implemented in this work) is to be considered as the more straightforward variant of this technique, since it requires only one photon source. Normally, only one single laser beam is required to tag tracer molecules along a line [35; 37; 81; 87], but grid configurations are also possible [88]. Different implementations of the MTV technique can be found in the literature (summary at Table 3.2):

- Laser induced photochemical anemometry (LIPA) or laser photochemical velocimetry (LPV) relies on measuring the absorbance of a photochromic dye tracer [75]. To the best of our knowledge this MTV technique is limited to liquid flows.
- Raman excitation coupled to laser-induced electronic fluorescence (RELIEF) has been used in the past for molecular tagging air flows [89; 90]. The technique requires three photon sources with different frequencies, two for tagging and one for interrogating, which is quite complicated to implement. In addition, its use is limited to oxygenated flows.
- Photo-activated nonintrusive tracking of molecular motion (PHANTOMM) technique, requires two or three laser sources. The initial excitation pulse is used to produce the tracer, which is tracked by detecting emitted light, instead of transmitted light as in the case of LIPA. Although this technique was initially developed for liquid flows, gas phase flows can also be imaged by the PHANTOMM technique (or its variants). Tracers can vary from ozone in the oxygen tagging velocimetry (OTV) technique [91], and nitric oxide generated from nitrous oxide in the N_2O MTV technique [92]. As the common mechanism of these variants are based on the fluorescence and not on the phosphorescence of a tracer, and because of the intense and short lifetime of fluorescence, the technique is very little sensible to oxygen quenching, which is an advantage. However, the relative low lifetime of the generated tracers limits its use to high-velocity gas flow, typically supersonic gas flows.

Table 3.2. Comparison between different MTV mechanisms.

MTV technique	LIPA	RELIEF	PHANTOMM	MTV by direct phosphorescence
Measurement mechanism	Detecting absorbance	Vibrational excited state fluorescence	Photoproduct fluorescence	Re-emitted phosphorescence
Tracer	Photochromic dye	Oxygenated flows	Laser dye	Non oxygenated flows
Advantages	Reusable tracer, long tracer lifetime	Ability to measure supersonic and subsonic flow	Can be used in both gas and liquid phase, insensible to oxygen quenching	Simplicity in setup, long luminescence lifetime;
Limitations	Only limited to liquid flows	A complicated setup, three photon sources in need, only limited to oxygenated flows	A complicated setup - two or three laser sources in need, low luminescence lifespan	Quite sensitive to oxygen and gaseous water

3.2.1 Photoluminescent principle of MTV

MTV is based on following in time the fluorescence and phosphorescence signal of tracer molecules after laser excitation. These are well-known photoluminescent phenomena and they are based on the absorption of a photon at a specific wavelength and the re-emission of a photon in the visible spectrum. An efficient approach for describing the molecular energy absorbance and energy emission after excitation is the Jablonski diagram, which represents the energy level variation process of molecules (Figure 3.5). If the molecule absorbs a photon, an energy "jump" is produced from the ground state (S_0) to an upper electronic state (excited molecule, $S_1, S_2, \ldots$). The lowest energy level of each electronic state corresponds to the vibrational ground state, inside an electronic state the molecule can have different vibrational states. Once the molecule is in its excited state, it necessarily comes back to its initial ground state through radiative (light-emission) or non-radiative transitions. The radiative transition corresponds to fluorescence and phosphorescence, while the non-radiative transition can be of a vibrational relaxation nature.

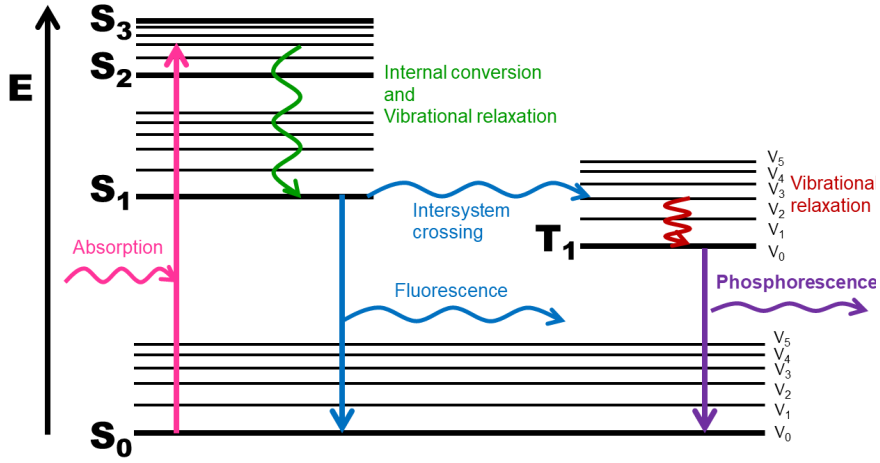

Figure 3.5. Energy diagram showing absorption of photon and the processes involved in the emission of light as fluorescence and phosphorescence.

- Absorption: the tracer molecule absorbs energy provided by the photon at a specific wavelength. Through this exchange, the molecule is able to reach a novel energy state. Depending on the nature of specific tracer molecule, the required energy between two

different energy states is well defined, thus only specific wavelengths of laser are absorbed by the molecule and can thus be used for excitation. This specific requirement underlines the necessity of knowing the absorption spectrum of each tracer molecule [93]. The absorption process happens very quickly, its time scale is on the order of 10^{-15} s. The very initial molecular electronic state is in the ground singlet state S_0 before exposure to a specific wavelength of light, after the absorption, the low-lying electrons jump to an excited electronic state (higher energy level) S_i ($i \geq 1$) and excited vibrational state. For example, S_1 is the so-called electronic first excited singlet state.

- Vibrational relaxation and internal conversion (non-radiative transitions): at higher energy states (S_i) the molecule is metastable. This occurs since the molecule is in thermodynamic disequilibrium in respect to the surrounding environment, thus it has to exchange energy with the surroundings to come back to its equilibrium ground state (S_0).The energy stored in the excited state can be dissipated through vibrational relaxation and internal conversion. Both these relaxation modes do not remit a photon, but relax through heat dissipation to a novel vibrational state. This implies that an excited molecule has higher temperature that its surroundings (local temperature rise). The triggering event for relaxation through heat dissipation is molecular collisions. The vibrational relaxation is very fast, that is in between 10^{-14} and 10^{-11} s. The molecule relaxes to different vibrational states within the same electronic state. The probability of this kind of dissipation is quite high and it is directly linked to this very fast transition. Internal conversion is a transition to a lower vibrational state belonging to another electronic state. The internal conversion is more probable to happen when the exited electronic state is higher than S_1. The internal conversion occurs in the same time scale of the vibrational relaxation, however, the internal conversion to the ground state can be slower allowing for other energy relaxation modes to occur at its place.
- Fluorescence (radiative transition): once the molecule is excited at a higher electronic state, it can fall back to the ground state S_0 by emitting a photon. The most probable fluorescence transition is a $S_1 \rightarrow S_0$ transition. Compared to the lifespan of the possible non-radiative relaxation, the lifespan of fluorescence is much slower, in the order of 10^{-9} to 10^{-7} s,

nearly four orders of magnitude slower than vibrational relaxation. The wavelength of the emitted fluorescence corresponds to the energy difference between the vibrational state at S_1 and the vibrational state at S_0, the energy of the emitted photon is always lower than the energy of exciting photon. The energy loss between exciting photon and photon emission is caused by vibrational relaxation and internal conversion. Since the molecule can move down to multiple vibrational states, the fluorescence emission spectrum can contain a wide wavelength range (Section 3.2.3).

- Phosphorescence (radiative transition): this radiative emission involves an intersystem crossing, where the spin multiplicity varies from an excited singlet state to an excited triplet state ($S_1 \rightarrow T_1$). From here on the molecule decays to the ground state, emitting a photon ($T_1 \rightarrow S_0$). Due to the intersystem crossing, the phosphorescence emission is the slowest transition, that is between 10^{-4} to 10^{-1} s. The energy difference between S_0 and S_1 is larger than the one between S_0 and T_1, thus the phosphorescence emission wavelength is higher than fluorescence.

From the perspective of the state transition, the time scale underlines the probability of each energy transformation process to occur. An occurrence is more probable to happen when the characteristic time of the transition is shorter. Based on the point of velocimetry measurements, the time scales of light emission are of critical importance. Tab 3.3 summarizes the time scale of the main radiative and non-radiative process, being phosphorescence the phenomenon with the most suitable lifetime for measurements in confined gas flows.

Table 3.3. The time scale of each transition state.

Transition	Time Scale
Absorption	10^{-15} s
Internal conversion	10^{-14} s - 10^{-11} s
Vibrational relaxation	10^{-14} s - 10^{-11} s
Fluorescence	10^{-9} s - 10^{-7} s
Intersystem crossing	10^{-8} s – 10^{-3} s
Phosphorescence	10^{-4} s - 10^{-1} s

3.2.2 Intensity and lifetime of LIF and LIP

Fluorescence and phosphorescence can be laser induced. As described by Thurber et al. [94], the signal obtained from a fluorescence emission depends on several parameters:

$$I_{f,ph} = \eta_{opt} \frac{E}{hc/\lambda_{ex}} dV_c n_{\text{abs}}(T) \sigma_{f,ph}(\lambda, T) \phi_{f,ph}(\lambda, T), \tag{3.1}$$

where η_{opt} is the overall efficiency of the collection optics (quantum yield), E is the laser fluence, $\frac{h\,c}{\lambda_{ex}}$ is the energy of a photon at excitation wavelength λ_{ex}, and dV_c is the collection volume. The temperature-dependent quantities are the number density n_{abs} of absorbing molecules, the molecular absorption cross-section $\sigma_{f,ph}$ of the tracer, and the quantum yield $\phi_{f,ph}$. Note that both $\sigma_{f,ph}$ and $\phi_{f,ph}$ depend on the excitation wavelength λ_{ex} as well as on the temperature T. Eq. (3.1) can also be extended to phosphorescence emission, and the subscripts f and ph represent fluorescence and phosphorescence, respectively.

The quantum yield depends on the exciting light wavelength, temperature, pressure, conversion velocity, and gas composition [95]. The quantum yield can be modeled as

$$\eta_{opt} = \frac{k_r}{k_r + k_{nr}} \tag{3.2}$$

where k_r and k_{nr} are the radiative and non-radiative rate constants, respectively. These quantities can be directly correlated to the lifetime τ_{lf} of the luminescent signal

$$\tau_{lf} = \frac{1}{k_r + k_{nr}} \tag{3.3}$$

According to the Eq.(3.2) and Eq.(3.3), the quantum yield of fluorescence is higher than phosphorescence, while the lifetime of fluorescence is lower than phosphorescence. This is due to the fact that for fluorescence the radiative rate constant $k_r \approx 10^9$ s^{-1} is higher than its non-radiative constant k_{nr}. While the radiative rate constant of phosphorescence is comparable to its non-radiative counterpart [79].

3.2.3 Tracer choice and behavior

Acetone is one of the most frequently-used molecular tracers for MTV, because of its appealing physical characteristics and luminescence properties [4; 35-37; 81; 86; 87; 93; 95-101].

Since acetone is a least toxic molecular tracer compared to diacetyl and toluene, no specific protection is required while dealing with acetone. Acetone is also a low-cost choice.

The molecular composition of acetone is $(CH_3)_2CO$, which is the simplest and smallest molecule in the ketone family being its molar mass of 58.8 g/mol. The saturation pressure of gaseous acetone is around 24 kPa at room temperature [102], which offers the possibility of relatively high-pressure experimental conditions at the gaseous state.

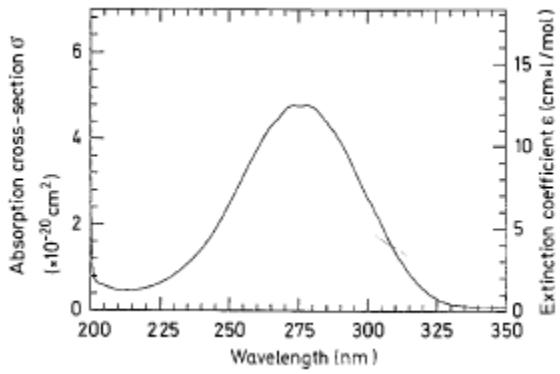

Figure 3.6. Gaseous acetone absorption spectrum. Reproduced from [95].

Gaseous acetone has a broad absorption spectrum, from 225 nm to 325 nm (UV light) [95], and the peak is around 275 nm (Figure 3.6). The emitted photons after excitation are mostly in the visible spectrum, ranging from 350 to 550 nm. To the best of our knowledge, the results on the absorption and emission spectrum of gaseous acetone is lacking in the literature [45; 102]. Nevertheless, even if the absorption peak of acetone is at around 275 nm, it has been observed that the highest emission peak is obtained for an incident monochromatic light source of around 310 nm [93]. The phosphorescence signal of gaseous acetone can be observed even at 0.1 ms [93], while the fluorescence signal can last at most 4 ns. Previous work realized by our group, showed that the phosphorescence signal emitted acetone vapor is still strong and durable also for partial pressures of acetone as low as 50 Pa in gas mixture [93], making it a more than effective tracer to be employed in rarefied gas flows. The intensity of laser-induced fluorescence and phosphorescence is both linear with the laser energy while not reaching its saturation state. An

oxygen-free environment is required since the acetone photoluminescence signal can be strongly quenched by oxygen [95].

3.3 MTV applications to gas flows

Due to its appealing characteristics, the MTV technique is considered as an effective tool for mini or micro liquid [103-107] and gaseous flows [81; 86; 100; 108-112]. In this section we will review the existing state of the art on external rarefied gas flows and internal gas flows in hydrodynamic conditions at the millimetric scale [90; 108; 113-115], and internal rarefied gas flows in mini-channels [35-37; 81; 93].

3.3.1 MTV application on external gas flows

MTV was used by Lempert et al [100],[116] in order to obtain two dimensional velocity maps of free jet flows at the exit of a supersonic micro-nozzle. The nozzles were inserted and then tested inside a visualization chamber (Figure 3.7) and the velocity fields were acquired by tagging a single line at several positions along the nozzle axis [116]. The experimental results were in good agreement with DSMC numerical results. The accuracy of velocity measurement can reach a 3.5% fractional uncertainty. This research verified the ability of acetone-based MTV diagnostics for the application of supersonic external micro gas flow by laser induced fluorescence.

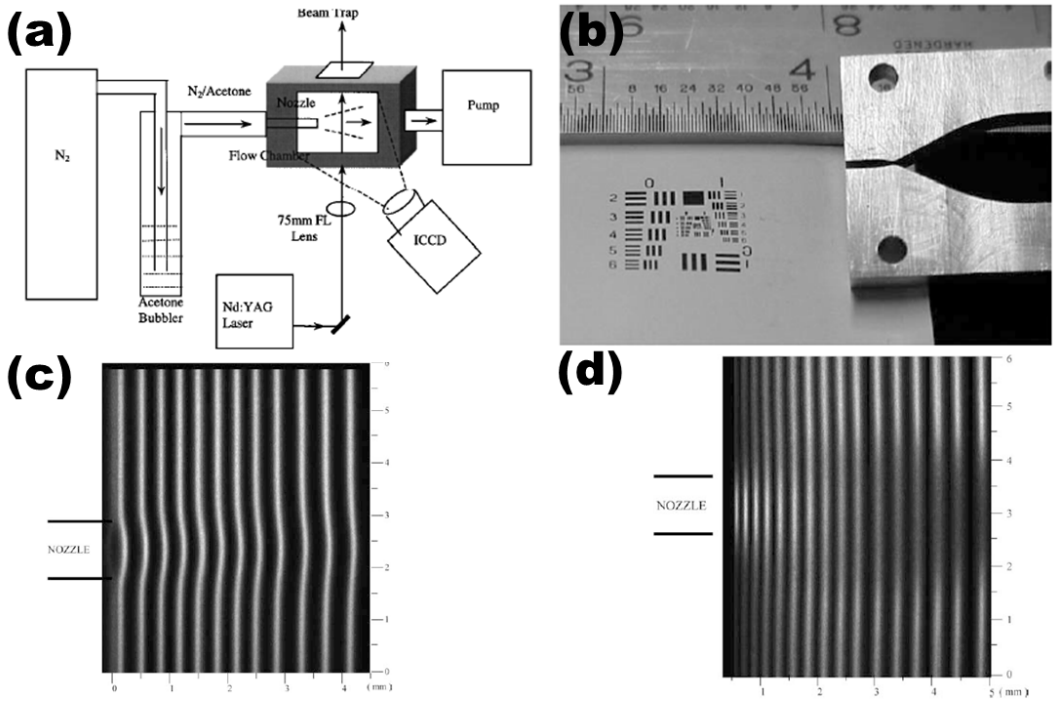

Figure 3.7. Acetone-based MTV application on external micro-jet flow: (a) the schematic of experimental apparatus; (b) photograph of the Mach 2 micronozzle; (c),(d) MTV images collage of individual images obtained at tagging positions along the nozzle exit with different pressure conditions. Reproduced from [100; 116].

Bathel and coworkers [115] used Nitric-oxide (NO) MTV to measure velocity profiles of a hypersonic flow via planar laser-induced fluorescence (PLIF). The velocity was acquired from the cross-correlation analysis of the deformation of a single tagged line displacement as the gas advection occurs. The images were acquired by a single double-frame camera. A new gating method was applied to get images with and without delay time in order to prevent the hardware limitation of the camera. The spatial, temporal, and signal uncertainty were also calculated. This novel experimental and post-processing method were successfully applied to acquire the velocity distribution and uncertainties for of Orion CEV yaw RCS jet and a 10 deg half-angle wedge in a gas air flow with Mach number as 10. The MTV measurement results on Orion CEV yaw RCS jet are shown in Figure 3.8.

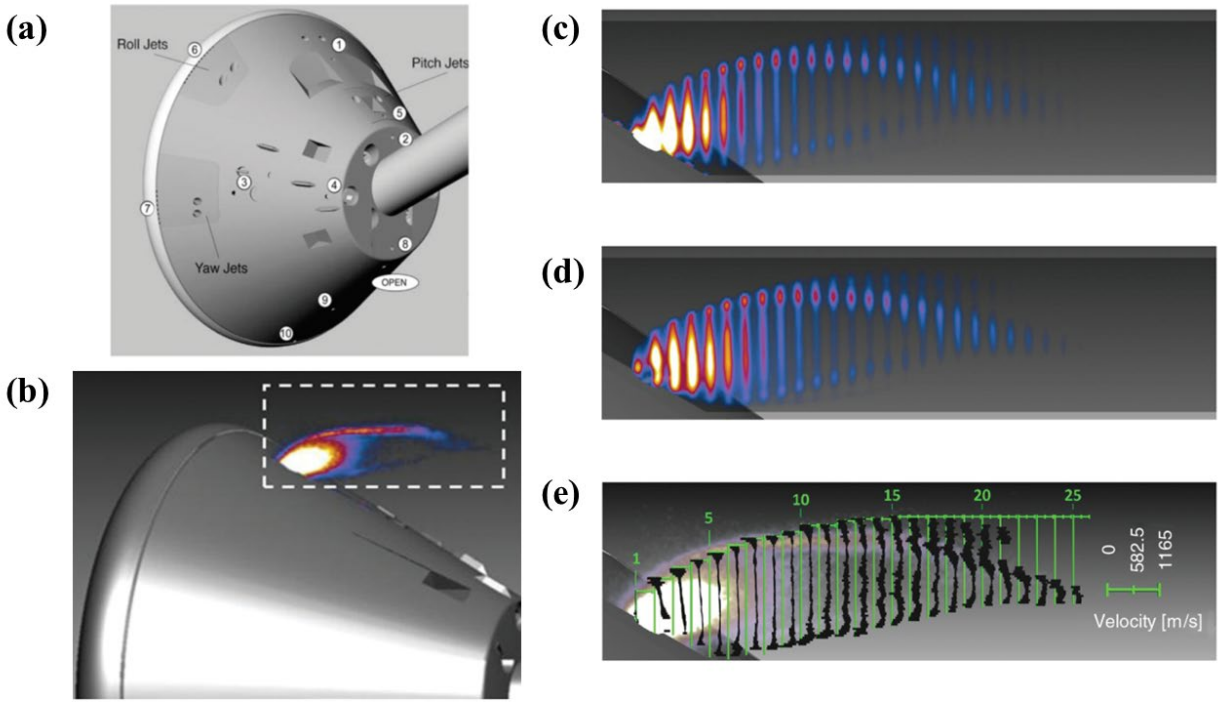

Figure 3.8. MTV application in Orion CEV: (a) the model of Orion CEV with close-up of yaw RCS jet, (b) test section, (c) undelayed displacement image acquired by MTV, (d) delayed displacement image acquired by MTV, and (e) measured average velocity with uncertainty results. Reproduced from [115].

3.3.2 MTV application on millimetric internal gaseous flow

The works that are going to be presented hereafter, were realized in rectangular channels using one dimensional molecular tagging velocimetry (1D-MTV). Although 1D-MTV has some limitations compared with 2D-MTV and stereoscopic (3D-) MTV, its advantages are also considerable, in respect to simpler implementation and a higher spatial resolution in the vicinity of the wall [37; 117]. This is why 1D-MTV is considered to be a promising technique for capturing velocity slip at the wall in slightly rarefied regimes. A classical schematic of 1D-MTV mechanism is summarized in Figure 3.9, which comprises an excitation laser, an intensified CCD camera, the rectangular channel and related gas system to create the internal flow.

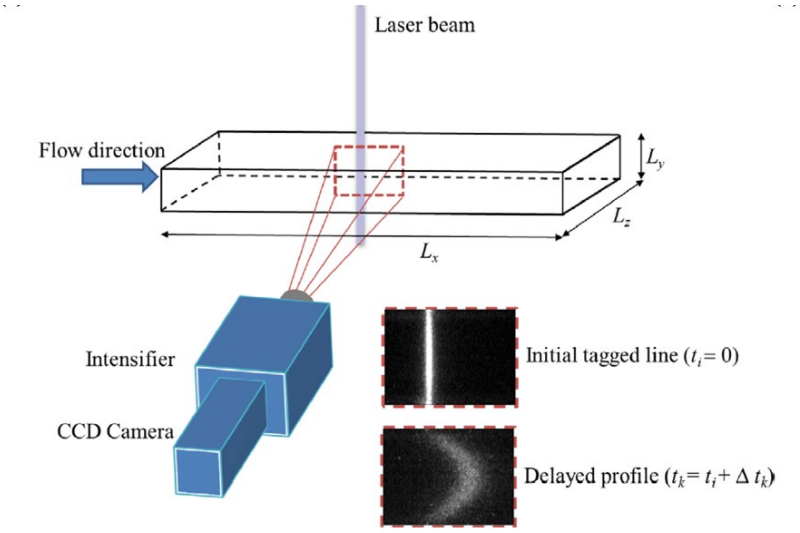

Figure 3.9. 1D-MTV mechanism. Reproduced from [37]

Samouda *et al.* [81; 87; 118] were the first to measure confined internal gas flows velocity profiles with µMTV by direct phosphorescence inside a rectangular channel of 1×5 mm^2 cross-section. The rectangular duct was a multiple material design with two optical accesses both for laser excitation and emitted light collection. Acetone vapor was chosen as tracer due its long luminescence lifespan. The experimental measurement of the velocity distribution at atmospheric pressure was comparable to the compressible Poiseuille flow in rectangular duct. However, the experimental results pointed out an unexpected velocity slip at the wall in hydrodynamic regime (Figure 3.10 (b), (c)).

Later on, Yamaguchi *et al.* [82] was the first to measure a confined internal gas flow at the microscale with a dual-laser µMTV by photoproduct fluorescence using nitric oxide (NO) as tracer. This work demonstrated that the experimental results of velocity profile in rectangular microchannel whose height was 513 µm and micronozzle whose throat width was 100 µm by µMTV at approximately atmospheric pressure and room temperature, which were only qualitatively comparable to numerical results. The work of Yamaguchi and coworkers validated the feasibility of dual-laser µMTV technique in velocity distribution measurements of the internal micro gas flows. Yamaguchi's results, even if of great interest, had still great uncertainties in respect to the theoretical velocity profiles to be expected for a classic Poiseuille flow and did not

show the ability of this dual-laser μMTV technique to measure the slip velocity of the rarefied micro gas flow, since all the measured micro gas flow were in continuum flow.

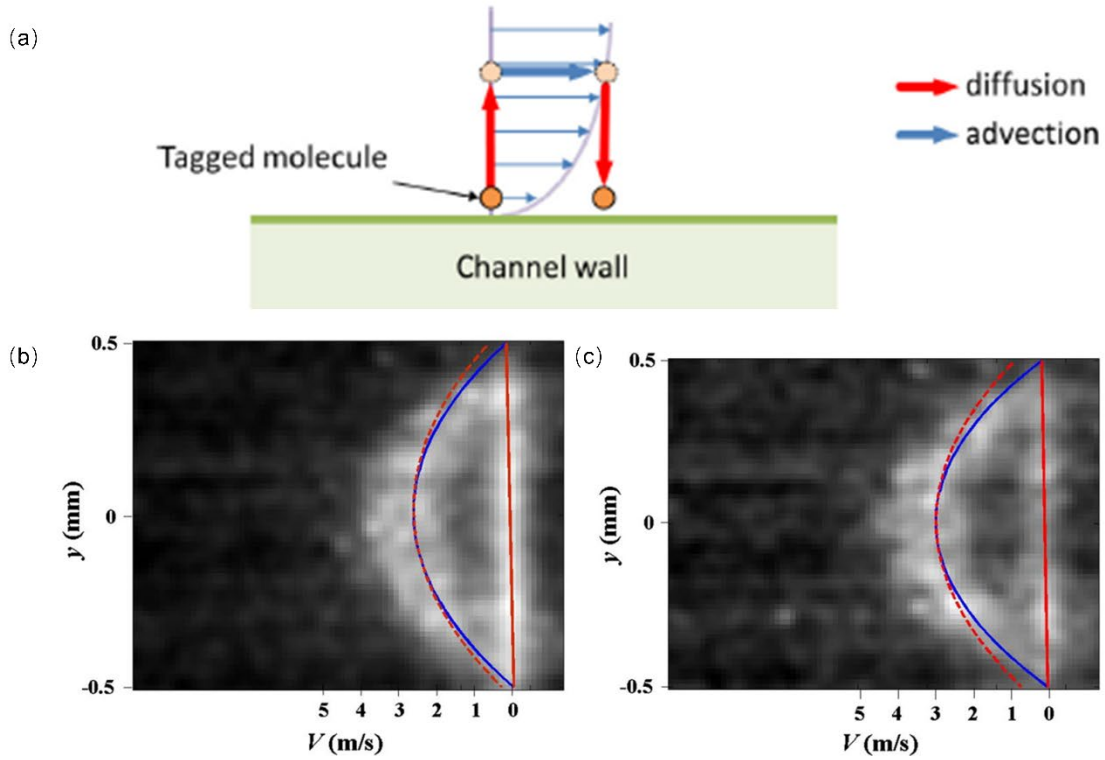

Figure 3.10. Unexpected molecular slip on the wall. (a) Molecular slip at the wall caused by Taylor dispersion; Experimental measurement results (red dashed line) of velocity profile of acetone-argon gas mixture flow in the middle plane of a rectangular channel compared with the corresponding theoretical results (blue solid line), indicating the initial tagged line (red solid line): (b) mean pressure $p_m = 50\ kPa$, pressure difference $\Delta p = 195\ Pa$, (c) mean pressure $p_m = 30\ kPa$, pressure difference $\Delta p = 220\ Pa$. Reproduced from [37; 81].

In the first MTV experimental data of gaseous flows in a millimetric rectangular channel [81; 87; 118], the velocity profile was simply deduced from the derivative in time of the streamwise displacement profile. With this approach the velocity profiles appeared more flattened than the expected theoretical velocity profile and an unexpected velocity slip was observed at the wall in (Figure 3.10 (b), (c)). The unexpected additional molecular displacement at the wall even for continuum flow was caused by the combined effect of diffusion and advection, which is commonly known as Taylor dispersion (Figure 3.10 (a)). This is also the reason for the unexpected non-zero velocity profile (Figure 3.10 (b), (c)).

Frezzotti *et al.* [36] verified via DSMC that the diffusion of tracer molecules can lead to a non-parabolic displacement profile. This effect increases with decreasing pressure. The authors proposed a velocity reconstruction method, based on the advection-diffusion equation, able to extract the velocity field from a displacement field by considering Taylor dispersion. The method was validated via DSMC for Kn < 0.1.

Si-Hadj-Mohand *et al.* [37] applied the reconstruction method to µMTV experimental data and successfully measured gas velocity profiles of Poiseuille flows in a rectangular channel, whose depth was of 960 µm. Velocity profiles of acetone-seeded helium flow were correctly extracted at atmospheric and sub-atmospheric pressures down to a minimum average pressure of 42 kPa (Figure 3.11). The measured velocity profiles were quantitatively validated by numerical results. However, the experimental results obtained were still limited to hydrodynamic regime.

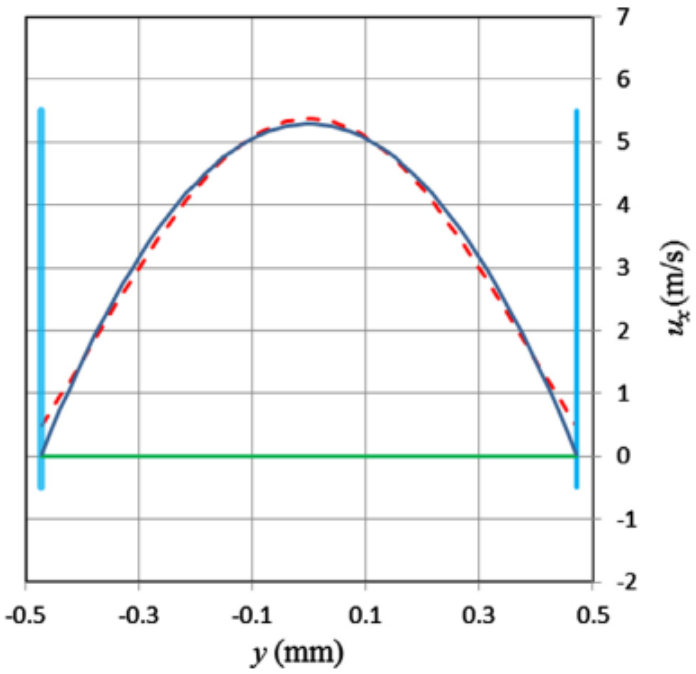

Figure 3.11. Comparison between experimental results of acetone-seeded helium flow at p_m= 42 kPa extracted from different method: reconstruction method (blue solid line), simple division from measured displacement profile by time of flight (red dashed line). Reproduced from [37] .

3.3.3 MTV for rarefied gas flows

In order to study the rarefied gas flow in slip regime, Fratantonio *et al.* [93] studied the lifetime and intensity of phosphorescence emitted by acetone and diacetyl vapor at low pressure. This work demonstrated that the maximum phosphorescence signal intensity that could be obtained by exciting acetone did not correspond to the absorption peak wavelength of acetone. The authors proved that acetone vapor excited at 310 nm and diacetyl vapor excited at 410 nm could be used in order to obtain a more intense and durable phosphorescence signal even for low pressures. The investigated pressures allowed reaching slip regime conditions for gas-tracer mixture flows in a 1-mm deep rectangular channel. The experimental results of this work also proved that acetone and diacetyl vapor were more than suitable candidates for applying MTV in internal gas flows at low concentrations. This work was also coupled with a numerical analysis obtained via DSMC that proved that the equipment processed by the team was sufficient in order to extract velocity profiles of rarefied gas flows.

Later on, Fratantonio *et al.* [35] measured via μ-MTV velocity profiles in a slightly rarefied acetone-helium mixture (the molar fraction of acetone vapor was 20%, the partial pressure is around 184 Pa) at around 1 kPa in a 1-mm deep rectangular channel. The Kn number range was comprised between 0.008 and 0.014. A good agreement was reached between the measured average velocity by MTV and average velocity offered by simultaneous measurements of mass flow rate via constant volume (CV) technique. The observed temporal evolution of displacement profiles of rarefied gas flow acquired by MTV are illustrated in Figure 3.12. This work reports the very first flow visualizations of an acetone-helium gas mixture in a confined domain and in the slip flow regime. In this work also preliminary results of the slip velocity at the wall were computed from the MTV data by means of the reconstruction method provided by Frezzotti *et al.* [36]. The velocity slip results, which are the first in its genre, are qualitatively in good agreement with theory. However, in order to be able to obtain information in respect to gas molecular interactions with the surface, further work needs to be realized in respect of measuring velocity slip at the wall with low uncertainty.

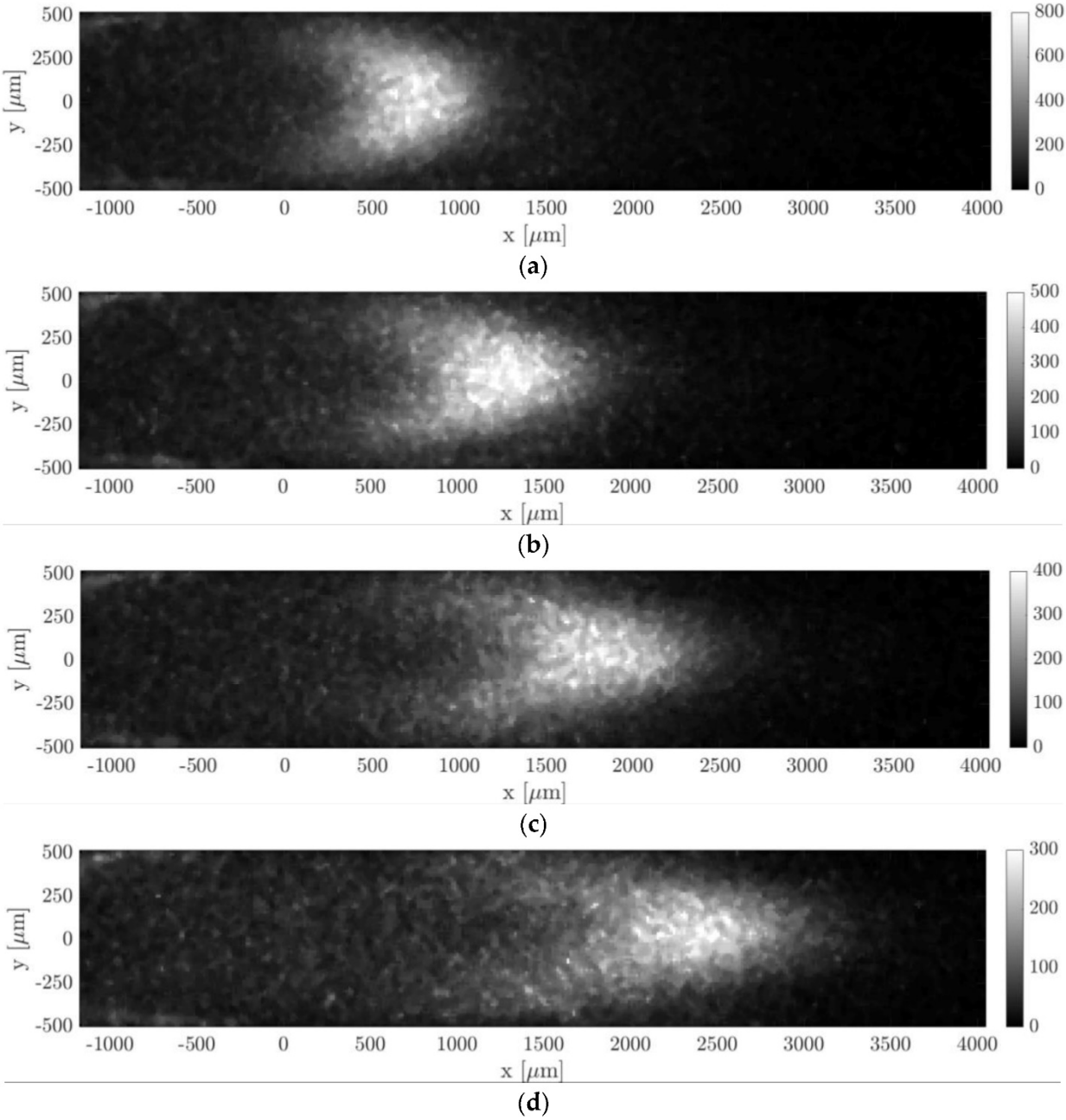

Figure 3.12. Displacement profile evolution with time acquired by MTV: rarefied acetone-helium flow at around 1.6 kPa with Knudsen number as 0.008, the acquisition time after laser excitation was (a) 20 μs, (b) 30 μs, (c) 40 μs, and (d) 50 μs. Reproduced from [35].

The experimental work of Fratantonio *et al.* [35] also demonstrated that in non-rarefied flows and for pressure conditions at which the effects of the molecular diffusion on the evolution of the molecular displacement profile were limited, the reconstruction method could provide a correct

velocity profile along the channel height and could correctly predict a negligible slip velocity at the wall. However, when the gas pressure was low enough (slip regime) the Taylor dispersion significantly distorted the tagged line, and thus the reconstruction method was unable to provide accurate information of the local velocity near the wall. Preliminary analysis [35; 37] revealed that the reconstruction method has a significant sensitivity to the height of the channel H and diffusion coefficient D of the tracer molecules through the carrier gas. Furthermore, Figure 3.13 illustrates the importance of correctly applying the reconstruction method, since the measured velocity profiles by simply following the macroscopic molecular trajectory in time are not representative of the gas flow.

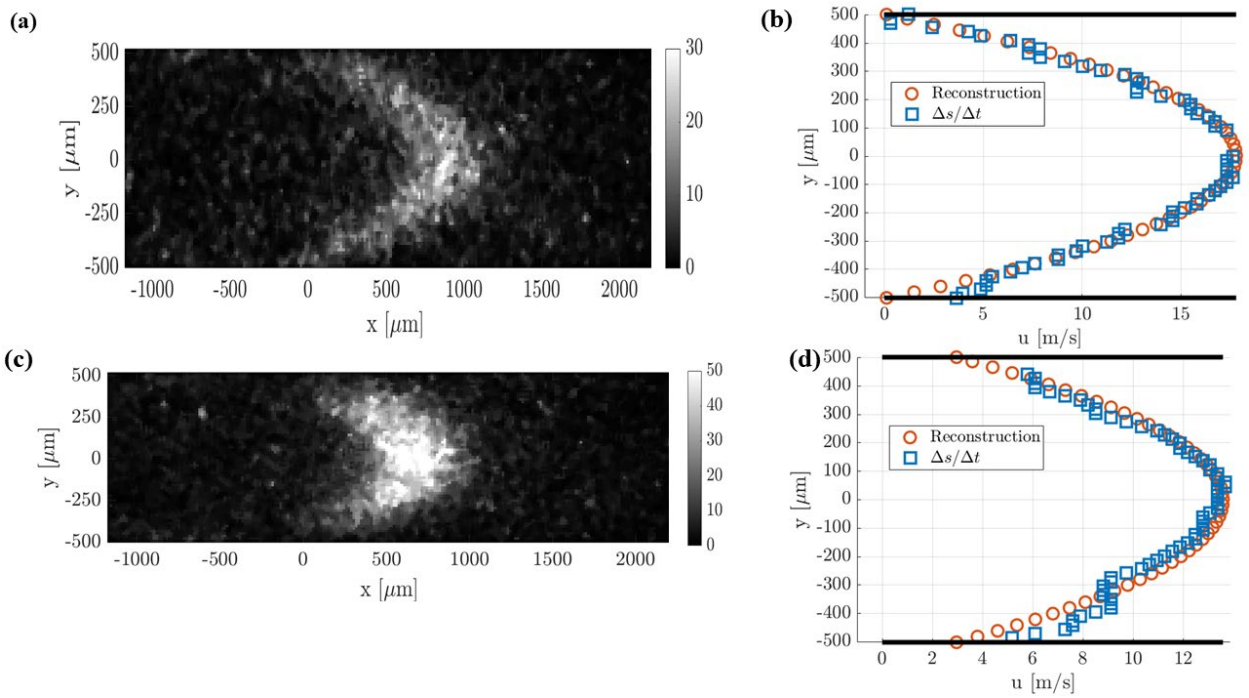

Figure 3.13. Reconstructed velocity profile at high pressure and at low pressure: displacement profile of acetone-argon flow at (a) 28 kPa and (b) 6 kPa acquired at 50 μs after laser excitation, velocity profile extracted from reconstruction method (orange circle) and displacement divided by time of flight (blue square) corresponding to overall pressure 28 kPa (c) and 6 kPa (d), separately. Reproduced from [35].

3.4 Conclusions

In this chapter, a state of the art on the optical velocimetry technique was presented, The MTV technique was compared with PIV and LDV techniques. From this comparison it was possible to argue that the MTV advantages are considerable, especially for measuring local velocity fields near the wall of hydrodynamic and rarefied gas flows. Of crucial importance is the choice of the molecular tracer to be employed, thus a summary of the most important photochemical processes was proposed. Furthermore, some applications of the MTV technique for external and confined flows were presented. A special focus was realized in respect to rarefied gas flows. As a conclusion, it is important to notice that further efforts need to be realized in order to better characterize the sensitivity of the post-processing algorithm and to improve the accuracy on the measurements. In order to apply the reconstruction methodology, of great importance is the correct determination of the diffusion coefficient of the tagged molecules. Since no consensus is to be found in the literature in respect to diffusion of acetone or diacetyl in single species or gas mixtures flows, further work is needed on the subject. This is why an original experimental setup based on the molecular tagging technique was developed in situ in order to measure diffusion coefficients of acetone non-intrusively for non-confined flows. To conclude, it is possible to argue that the present state of the art sufficiently demonstrates the ability of the MTV technique to obtain local measurements in rarefied gas flows. In the next chapter, the detailed description of the experimental setup is presented.

Chapter 4 Measurements of diffusion coefficient and kinetic diameter of acetone vapor via molecular tagging

As discussed in the last chapters, the molecular tagging technique is a promising methodology for local velocity and temperature measurement of rarefied gas flow. MT has been successfully applied to velocimetry measurements in mini-channels from continuum to slightly slip regime (lower pressures). A reconstruction method based on Taylor dispersion was developed to extract the velocity profile from displacement profiles by considering the diffusion effect of the tracer molecules through the carrier gas. The reconstruction method succeeded in extracting correct velocity profiles in continuum flow, however, failed in the slip regime. One possible cause of the divergence between results provided by the reconstruction method and theory can be related to an incorrect estimation of the diffusion coefficient, caused by a large discrepancy in the kinetic diameter value of acetone vapor in the literature. In this chapter, on the basis of MT, we optically measured the diffusion coefficient of acetone for a large pressure range. Indirectly, through the Chapman-Enskog equation, the kinetic diameter of gaseous acetone was estimated. The measurements were realized by recording the temporal evolution of the spatial photoluminescence distribution of acetone vapor.

4.1 Kinetic diameter and diffusion coefficient of gaseous acetone

Provided that the kinetic diameter of the molecule is known, via the Chapman-Enskog diffusion equation [119] it is possible to calculate the diffusion coefficient of gas at fixed thermodynamic conditions as

$$D = \frac{3\sqrt{\pi}}{8}\sqrt{\frac{k_B\,T}{m}}\frac{k_B T}{\sqrt{2}\pi d^2 p}, \tag{4.1}$$

where d is the kinetic molecular diameter.

However, in the literature there is a large discrepancy in respect to the correct estimation of the kinetic diameter value for acetone. Initially, when applying the reconstruction method to our molecular tagging data, the value provided by Van der Perre et al.[120], that is $d = 470$ pm, was considered to be appropriate, since it was also supported by several other authors [121; 122]. However, at lower pressures, the reconstruction method started failing and we started questioning if the value provided by [1] was still appropriate. Other works provided quite different estimations of the gaseous acetone kinetic diameter and its value ranged between 460 pm and 730 pm (Table 4.1). These discrepancies in the molecular diameter introduce relative deviation on the value of diffusion coefficient D that can be as large as 100%.

Table 4.1. Kinetic diameter of gaseous acetone molecules published in the literature and the corresponding diffusion coefficient value at p = 1 kPa, T = 293 K computed via Eq.(4.1).

References	Kinetic diameter of acetone (pm)	Diffusion coefficient at p = 1 kPa (m^2/s)
Hu et al. [123]	460	5.8565×10^{-4}
Frezzotti et al. [35]	730	2.3254×10^{-4}
Nadykto & Yu [124]	616	3.2658×10^{-4}
Bowen et al. [125]	416	7.1609×10^{-4}
Almy & Anderson [96]	590	3.5600×10^{-4}

That is why it was of crucial importance for the purpose of obtaining reliable velocity measurements via MTV, to shed light on the correct estimation of the diffusion coefficient at low pressures. In this chapter we present new experimental measurements of diffusion coefficient via molecular tagging technique and an indirect estimation of the kinetic diameter of acetone vapor through the Chapman-Enskog equation. The diffusion effect can be represented by the temporal evolution of spatial broadening of the tagged line of tracer molecules. The experimental setup and methodology are summarized in Section 4.2 and Section 4.3, separately. The measured results are described in Section 4.4.

4.2 Experimental setup

The main objective of the experimental work described in this chapter was to visualize the self-diffusion of gaseous acetone after laser excitation inside a visualization chamber. The static thermodynamic conditions of the tracer were regulated during the whole duration of one experiment. The main elements of the experimental setup used in this work can be classified as laser and optics (Section 4.2.1 & 4.2.2), acquisition system (Section 4.2.3), and gas circuit (Section 4.2.4).

4.2.1 Laser system

As discussed in Chapter 3, one of the most popular tracers used for gas flow visualization studies is acetone vapor [35; 37; 108]. In this thesis, an OPOlette HE355LD (Figure 4.1) laser was used for all the experiments, since it allowed us to provide the proper wavelength excitation for acetone vapor, which was set to 310 nm, for obtaining an optimum signal intensity and phosphorescence lifetime [93].

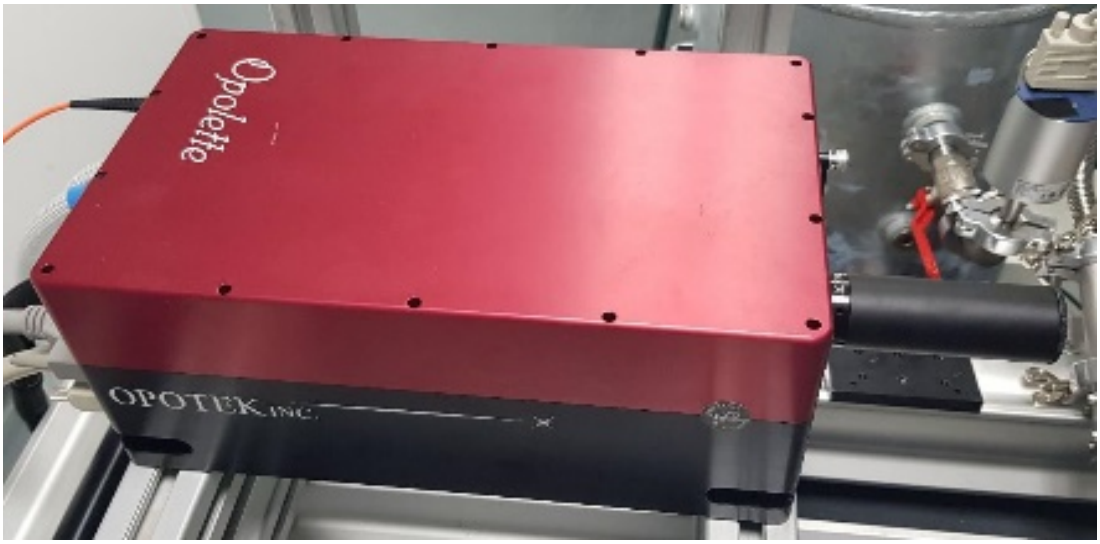

Figure 4.1. OPOlette HE355 LD. Figures from Opotek Inc.

The laser system with Optical Parametric Oscillators (OPO) technology is a passive, non-linear optical device, which converts the output of a pump laser into two beams of longer wavelengths, Signal, and Idler beam. The OPO device consists of a non-linear optical crystal

placed within an optical cavity. The high-intensity pump laser beam at frequency $1/\lambda_p$ is injected into the cavity containing the non-linear crystal. As a result of the interaction between the laser radiation and the crystal, two beams at different frequencies $1/\lambda_s$ (Signal) and $1/\lambda_i$ (Idler) are generated, the relationship between λ_p, λ_s and λ_i is $1/\lambda_p = 1/\lambda_s + 1/\lambda_i$ (Figure 4.2). The OPOlette laser that we used is a tunable laser system, and the pump laser wavelength is 355 nm. Thus, we could get the output signal wavelength in the ultraviolet (210-355 nm) and visible (410-710 nm) ranges, also the idler laser in the infrared (710-2400 nm) range.

A precise synchronization between triggering the laser pulse and recording the images was needed. The software to operate and trigger the laser provided by the laser manufacturer (La Vision®). The OPOlette laser could provide a repetition rate of 10 Hz or 20 Hz. The main technical features of the laser system are summarized in Table 4.2. The beam quality factor, M^2, is provided by the manufacturer only for laser beam at 500 nm.

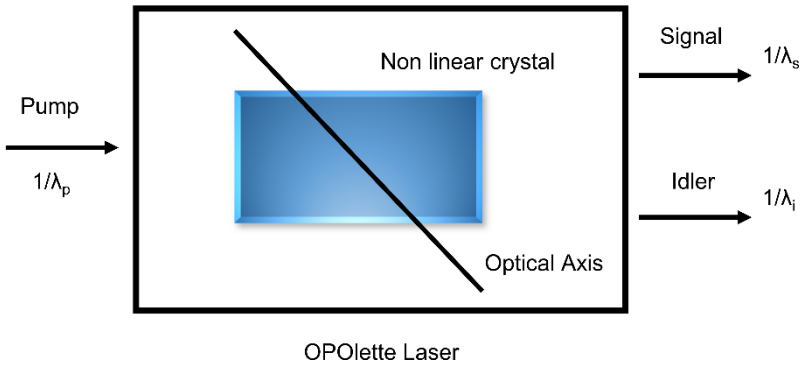

Figure 4.2. Mechanism of OPOlette laser.

Table 4.2. Main technical features of OPOlette HE355 laser.

Wavelength	210-355 / 410-710 nm
Pulse duration	7 ns
Repetition rate	10 or 20 Hz
Beam diameter at the exit	4 mm
Highest energy at 450 nm	8 mJ
M^2 at 500 nm	3.94
Beam divergence	< 0:5 mrad

4.2.2 Beam focusing and laser energy monitoring devices

The laser beam had to be focused inside the visualization chamber so that the excited molecules remained in the field of view (FOV) of the camera during the whole duration of one diffusion experiment. This required a thin laser beam diameter at the commencement of the experiments. The OPOlette system provided a laser beam of a 4 mm diameter, thus an optical path was necessary to focus (reduce) the laser beam into the visualization chamber. However, if the laser diameter is greatly focalized this might cause damages to the optical accesses of the gas chamber. This is why an equilibrium between laser focalization and laser energy was needed in order to protect the integrity of the optical accesses.

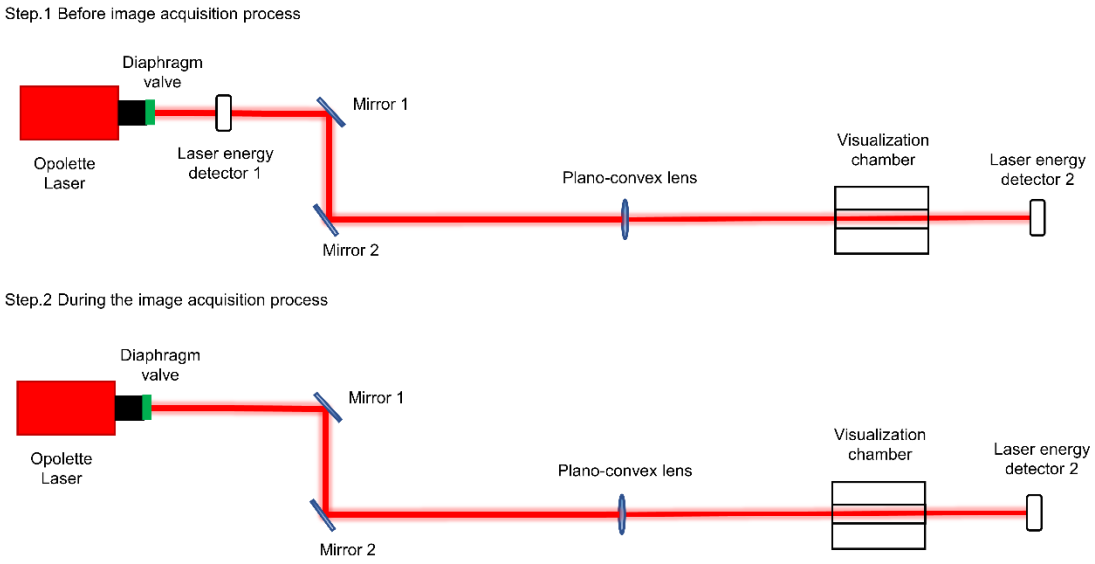

Figure 4.3. The schematic optical path for laser alignment and energy detection.

For these reasons, we used a series of optics in front of the OPOlette laser, composed of a diaphragm valve and a plano-convex lens to focus the laser beam. A pair of laser energy detectors were used to monitor the laser energy variation during the experiments. Finally, a pair of mirrors were placed at 45°, in a Z-Fold configuration, in order to align the UV beam. Figure 4.3 shows the optical system, red solid lines represent the optical path passing through the optics. Let us underline that it is also important to avoid the laser beam reflections back into the laser system. This might

damage the OPOlette laser. For this reason, the optical system should be positioned far enough from the laser system exit to avoid dangerous reflections.

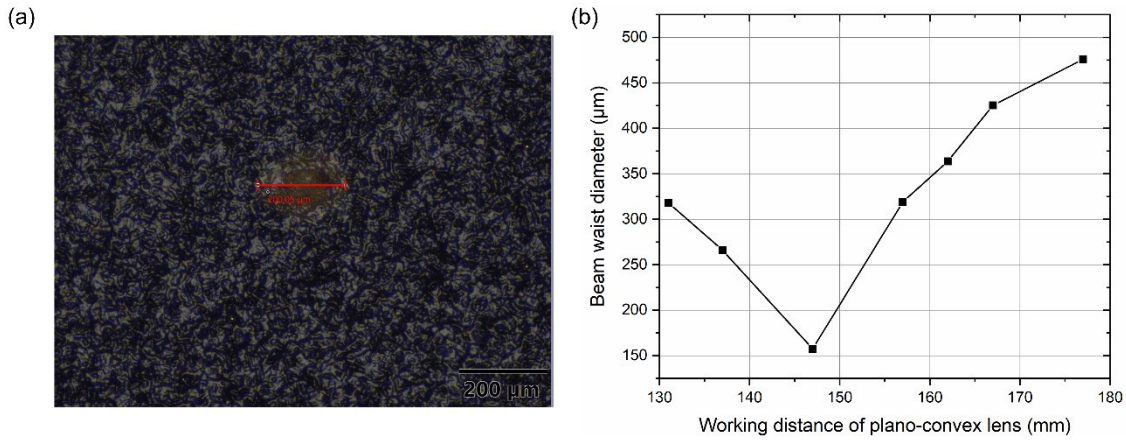

Figure 4.4. Plano-convex lens working distance definition with laser alignment paper. (a) An example of laser burn mark with working distance as 15.1 cm; (b) Laser beam diameter evolution with working distance of plano-convex lens.

The diaphragm valve controls mechanically the diameter of the laser beam at the exit of the OPOlette laser. It decreases the diameter of the laser beam when decreasing the diaphragm dimension. The diaphragm valve also helps to prevent the idler beam. To further reduce the beam waist of the laser, a plano-convex lens was used in order to focus the laser beam into the visualization chamber. The asymmetry character of plano-convex lens also allows to reduce spherical aberrations. There is an anti-reflective (AR) coating on the lens surface, which can increase the transmission of UV light. The focusing length of the plano-convex lens, provided by manufacturer, is 15 cm for a 266 nm wavelength, while at 310 nm, the focal length was measured to be 14.7 cm. The focusing distance of the plano-convex lens at a wavelength of 310 nm was defined with a laser alignment paper (black burn paper). The laser beam burns the laser alignment paper and leaves a mark. The shape of the burn marks can indicate the profile of the laser beam. The laser beam profile of the OPOlette laser was considered to be a perfect Gaussian distribution, however, the measurements showed a slightly elliptical shape (Figure 4.4 (a)). The optimum focalizing distance of the plano-convex lens was defined by comparing the dimension of the major axis of the ellipse-shape in respect to different focalizing distances. The measurements were

realized for same laser energy and paper burning time. The final value is the average value of several tests. The beam waist diameter evolution with varying plano-convex lens working distance is shown in Figure 4.4 (b).

Pyroelectric laser energy detectors Gentec-EO® were used for real-time monitoring of the energy stability of the UV laser beam during the experiments before and after passing through the visualization chamber (Figure 4.3). The full-scale energy density of the sensor varied from 8 to 1 J cm^{-2} at 1064 and 266 nm, respectively. While the sensitivity provided by the manufacturer was 103 V/J at 1064 nm, with an uncertainty of ±3% expressed with a 95% level of confidence. In average, the measured values ranged between 30 and 70 µJ in this study. In order to reduce the laser fluctuations, the laser system needed to warm up during around 50 minutes before use. Other characteristics provided by the manufacturer are presented in Table 4.3. As shown in Figure 4.3, the laser energy was monitored in front ($E_{1,init}$) and on the back ($E_{2,init}$) of the visualization chamber under vacuum conditions, and while performing the experiments on the back of the visualization chamber ($E_{2,img}$). By these means it was possible to calculate the laser energy loss due to the optics and acetone absorption.

Table 4.3. Main technical features of energy detector.

Spectral range for measurement	193 to 2100 nm
Maximum repetition frequency (for pulsed laser)	300 Hz
Energy sensitivity	103 V/J at 1064 nm
Energy calibration uncertainty	± 3% of measured value
Maximum energy density	8 to 1 J cm^{-2} at 1064 and 266 nm, respectively
Aperture width of sensor	9 mm
Aperture height of sensor	9 mm

4.2.3 Acquisition system

The image acquisition system was composed of a photodetector with a 25-mm intensified relay optics (IRO) and a 12-bit Imager Intense (LaVision®) progressive scan charge-coupled device (CCD), the overall system is defined as ICCD. The internal structure of the ICCD could be divided into six parts: 1) the external lens system for collecting the emitted light of the tagged

tracer; 2) the photocathode, which converts the incident photons into electrons; 3) the micro channel plate (MCP), which amplifies the electron flux generated by the photocathode; 4) the phosphor plate, which reconverts in "green" photon the electron bombarding coming from the MCP; 5) the lens coupling system, which collects the light emitted by the phosphor plate; 6) the CCD, which accumulates electrical charges proportionally to the light received. The schematic of the internal structure of ICCD is shown in Figure 4.5 (b).

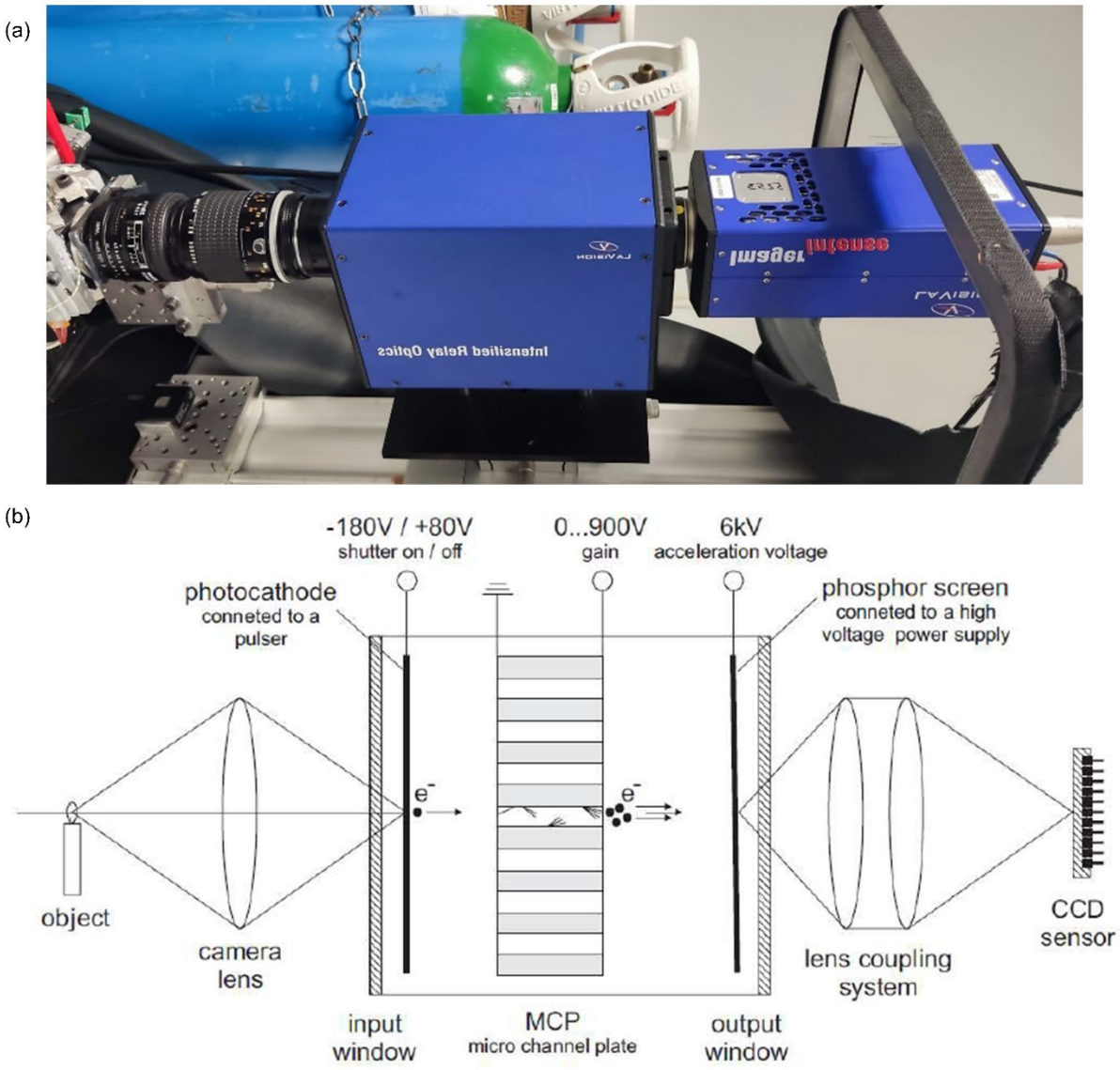

Figure 4.5. The photo of ICCD system (a) and schematic of the internal structure of the ICCD from LaVision® (b). Figure from LaVision® documentation.

i. External lenses

The external lenses collect the photoluminescent light emitted by the tracer. The optical system was composed of two external 105 mm f: 2.8 and inverted 28 mm f: 2.8 Micro Nikkor® lenses. At low pressure, the fluorescence and phosphorescence signal are very low, thus, the two objectives were set to the maximum aperture. The focal length was measured to be 32.3 cm.

ii. IRO

The IRO is an electro-optical device which provides the amplification of the light received and high-speed gating imaging. It is an essential element for the detection of phosphorescence of acetone vapor at low pressures, since the low tracer concentration and the high molecular diffusion weakens the signal intensity. The IRO is composed by a photocathode which is a photoelectric device that emits electrons when it is hit by an incident photon. The physical properties and capacity of S20 photocathode mounted on the ICCD allows minimum gate times of 100 ns. The lifetime of ICCD is also mainly determined by the photocathode.

The electrons emitted by the photocathode are multiplied by the MCP, which is a circular plate of 25-mm diameter, of 400-μm thickness, and formed by more than 1 million microchannels of 6 μm in diameter. The regulation of the MCP voltage difference provides the control on the intensity of the light amplification, that is the gain G of the IRO. The electrons coming out from the MCP micropores are accelerated towards the P46 phosphor plate. Differently from the photon-electron conversion of the photocathode or of the CCD, the electron-photon conversion provided by the phosphor plate amplifies the signal, and for each received electron, more than one photon is generated. The photons emitted by the phosphor plate are collected by a system of lenses and directed towards the cells of the CCD. Differently from the external optical collector, the projected image is not inverted. While the minimum exposure time of a CCD is usually of the order of milliseconds, the image intensifier can reduce the exposure to a hundred of nanoseconds by means of an electronic shutter device.

iii. CCD

At last, photons collected by the lenses system arrive at the charge-coupled device. The CCD accumulates internal charges proportional to the received light. The spatial resolution was 1376

(horizontal) × 1040 (vertical) pixels. For the specific case of the lenses used, the size of each single cell of the CCD is 3.8 × 3.8 μm^2, which provided a field of view of 5.23 × 3.95 mm^2. The maximum photon-electron conversion is 65% when incident photons have a wavelength of 500 nm. The signal conversion, from analogy to digital, is accomplished by the line-by-line readout process as shown in Figure 4.6.

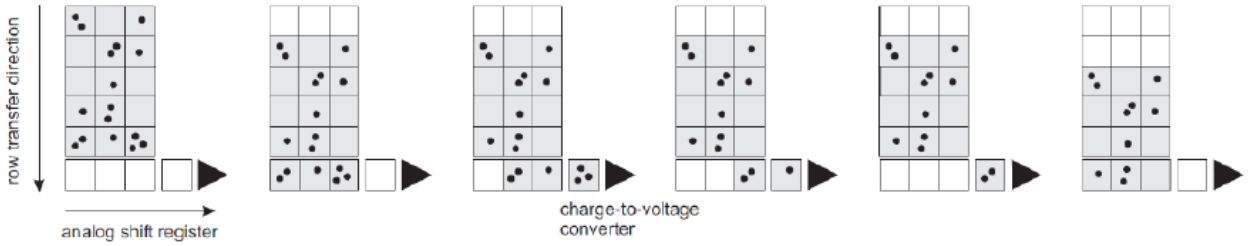

Figure 4.6. Readout process in each single cell of the CCD. Figure from LaVision® documentation.

Binning is a process that combines several adjacent pixels into a single larger pixel. The process of 2 × 2 and 4 × 4 binning are illustrated in Figure 4.7. The aggregation of pixels reduces the amount of data, thus simplifying the image processing, and increasing the read-out speed. Binning also decreases the readout noise, therefore, the value of signal-to-noise-ratio (SNR) is increased, for example, a 4 × 4 binning will increase the SNR of 16 times. Only when the light intensity is low enough like our case, the readout noise could not be neglected.

Most of the work in this study is obtained employing a 4 × 4 binning whereas at cost of spatial resolution, that is the size of a single pixel increases from 3.8 × 3.8 μm^2 to 15.2 × 15.2 μm^2.

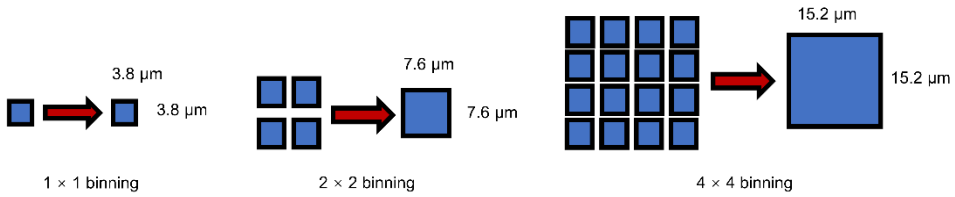

Figure 4.7. Combination of photosites by binning.

4.2.4 Gas circuit

The main part of the gas system used in this study is the visualization chamber. Since acetone vapor has a saturated vapor pressure of 24 kPa at 20 °C, the experiments can be realized from this pressure down to several hundred Pascals. The visualization chamber had the goal of keeping gas in static thermodynamic conditions while providing optical accesses for the laser tagging line and signal acquisition. The chamber is fabricated with aluminium alloy, which is chemically insensitive to acetone vapor. The laser access and exit are made of Suprasil®, a fused silica grade UV transparent material [87]. The optical access for the camera is the Borofloat® glass plate, located on top side of the gas chamber, which is thermally stable glass grade and has a very good chemical resistance to acetone (Figure 4.8 (a)). This chamber is also suitable for molecular tagging thermometry applications. This passing-through design both reduced the reflections of the laser beam inside the chamber and permitted a real-time control of the energy of the laser via an energy detector located at the end of the optical path.

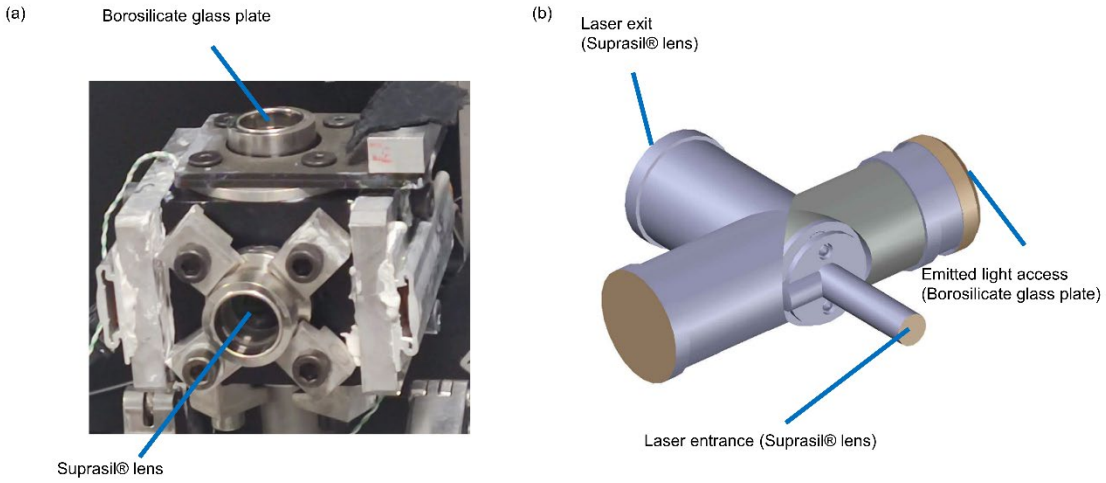

Figure 4.8. Visualization chamber: (a) External look and (b) inside structure.

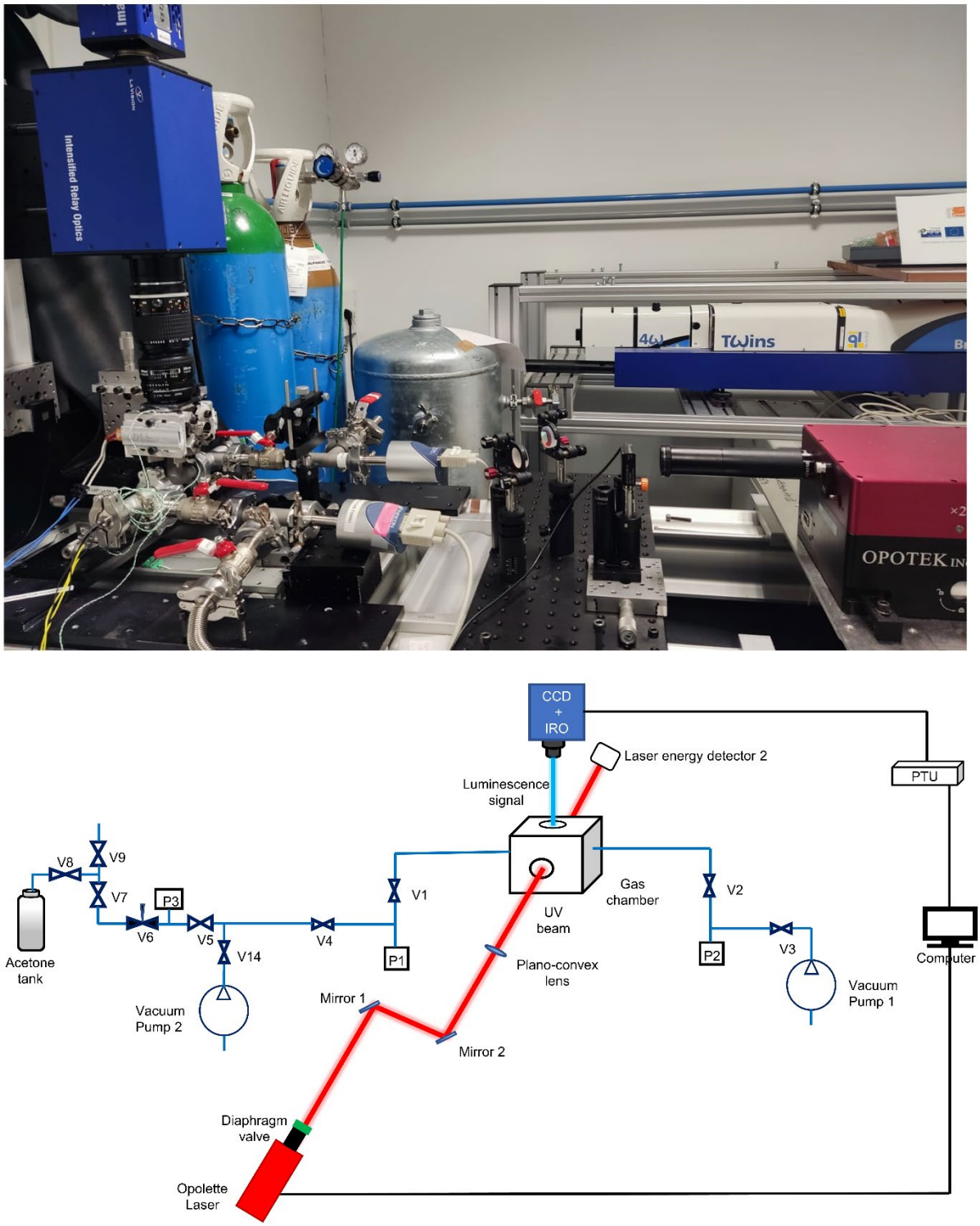

Figure 4.9. Physical photo (top) and Schematic (bottom) of experimental setup for phosphorescence analysis.

The configuration of the experimental setup is shown in Figure 4.9. The different components are connected via Swagelok® fittings and Kalrez® O-rings to ensure good sealing properties. The connecting elements are chemically compatible with acetone molecules. Two Inficon® capacitance diaphragm sensors with different scales (P1 of 100 torr, P2 of 10 torr) were used to monitor pressure inside the gas chamber. The 100 torr sensor could be replaced to a 1000 torr sensor depending on the pressure range that we investigated. The 10 Torr pressure sensor was used to monitor the leakages and the temporal stability of the chamber at low pressures. The resolution of the pressure sensors is 0.03% of the full scale, and the uncertainty on the measurements is 0.15% of the reading. The minimum characteristic time response of these sensors is 30 ms, smaller than the characteristic time of pressure variations recorded during the image acquisition process, which is in the order of minutes.

The gas chamber was connected to a tank containing liquid acetone at room temperature. The acetone tank was kept in a vertical position in order to guarantee that only acetone vapor is drown into the chamber. The thermodynamic conditions in the inlet gas line were monitored via pressure sensor P3. Two GEFI® rotary vacuum pumps were used to regulate the pressure of the system. Vacuum pump 1 was used to evacuate the visualization chamber while vacuum pump 2 was used for controlling pressure in the gas line. All the valves were Pfeiffer® valves, except for valve V6, which was a HEF® dosing valve for precisely controlling the amount of acetone vapor introduced into the gas chamber.

4.3 Experimental Methodology

Diffusion experiments were performed inside a static visualization chamber filled with acetone at stationary thermodynamic conditions. The investigated pressure range was between 500 Pa and 10 kPa at room temperature $T = 294 \pm 0.5\ K$. The starting moment of the experiment (t_0) corresponded to the UV laser beam excitation of acetone molecules inside the chamber. After excitation, the acetone tracer emits light in the visible spectrum. The luminescent signal was used to visualize and measure the macroscopic displacement of the molecules. The phosphorescent emission can last up to the millisecond range, depending on the molecular concentration, which is

enough to measure molecular diffusion. After the initial tagging instant, the signal acquisition was realized at 0.005 µs, 0.5 µs, 1 µs, 2.5 µs, then every 2.5 µs until 10 µs, then every 10 µs until 100 µs and finally every 50 µs until 500 µs for a total of 24 acquisitions per each experiment. Typically, the maximum time intervals used in previous MTV works were of 50 µs for pressures as low as 180 Pa of partial pressure of acetone in the gas mixture [15]. Thus, the time intervals used in these experiments are definitively longer than what can be found in the literature.

4.3.1 Static thermodynamic conditions

Static and well-controlled thermodynamic conditions are needed in the visualization chamber during the experiments. Before the beginning of one experimental campaign experiment, the chamber was vacuumed during 2-days in order to remove any unwanted gas molecules trapped by the walls of the chamber, especially oxygen which is a catalyser for quenching the luminescent signal of acetone. This procedure is also applied to all the connection elements of the gas circuit.

Table 4.4. Pressure variation over time during the image acquisition process

Mean (Pa)	Standard Deviation (Pa)	Max Value (Pa)	Min Value (Pa)	Percentage Variation (%)
587	11.3	606.5	567.5	±3.3
1098.8	14.6	1124.1	1073.5	±2.3
1530.9	9.7	1547.7	1514.1	±1.1
2015.6	7.3	2028.3	2002.8	±0.6
2504.1	10.3	2522.1	2486.2	±0.7
3006.4	5.2	3015.4	2997.4	±0.3
3475.3	8.2	3489.5	3461.1	±0.4
4015.9	2.1	4019.6	4012.3	±0.1
4493	6.5	4504.3	4481.7	±0.3
4988.1	0.3	4988.6	4987.5	±0.0
5995.3	2.2	5999.1	5991.5	±0.1
6909	17.7	6939.6	6878.3	±0.4
8076.2	15.9	8103.8	8048.7	±0.3
9011.6	16.5	9040.2	8983	±0.3
10028.3	16.4	10056.7	9999.9	±0.3

Theoretically pressure should remain constant during one experiment. However, absorption and desorption of acetone molecules in respect to the inner walls of the visualization chamber and leakages of air might affect slightly the pressure stability. Measurements showed a slight variation of pressure in the chamber (Table 4.4). The variation was calculated as |Final Value - Initial Value| / (2*Mean Value), which indicates how pressure varied during one experiment. The strongest pressure variation was found at lower pressures for a maximum of ±3.3% variation in respect to the nominal pressure, while the variation was always lower than ±1% for pressures higher than 1.5 kPa.

4.3.2 The on-chip integration technique

Since the luminescent signal provided by the tracer after laser tagging was very low, the signal acquisition was realized through an on-chip integration technique [37]. By utilizing this technique, it is possible to integrate more than one laser pulse in each single image. To integrate more laser pulses, the CCD shutter keeps open, until we collect enough number N_l of laser pulses in one image. Several N_i images are then averaged together to form one final image (Figure 4.10). The main parameters to be set were:

1) The exposure time of the CCD detector is t_{CCD} and it stays open during the whole duration of one experiment, being the IRO gate the real exposure time to the luminescent signal.
2) The gate time Δt_{gate} is the duration of the IRO opening, during this time interval the signal is integrated on the CCD. Let us remind here, that the IRO has the goal of intensifying the luminescent signal for it to be "seen" by the CCD.
3) The delay time t is the time between the laser Q-switch trigger and the IRO trigger, in other words the delay between the laser shot and start of image acquisition.
4) N_l is the number of laser shots per image;
5) N_i is the number of images, which are then averaged to provide a final image;
6) The IRO gain G is the signal amplification;

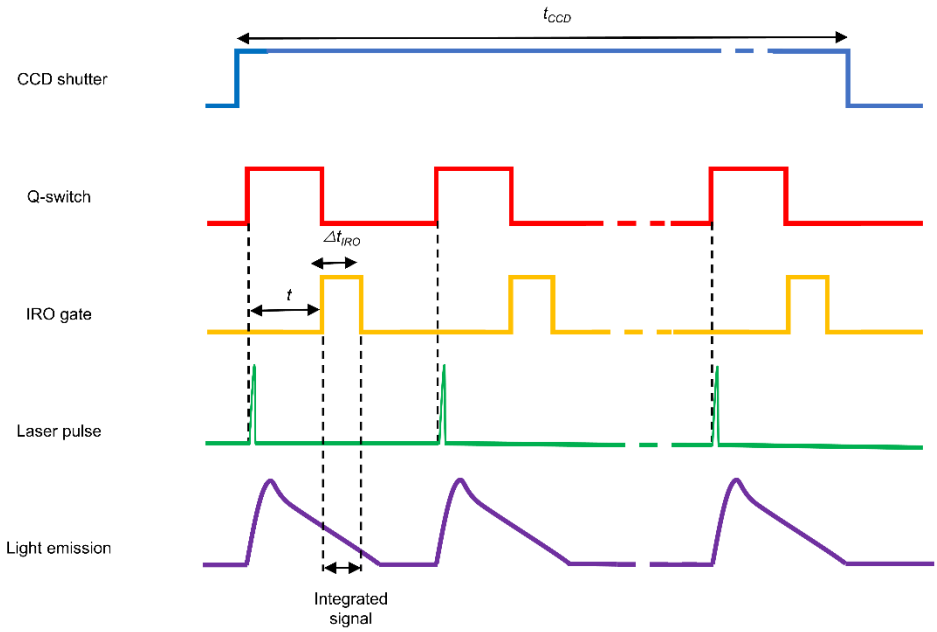

Figure 4.10. Sequence of operations for image acquisition.

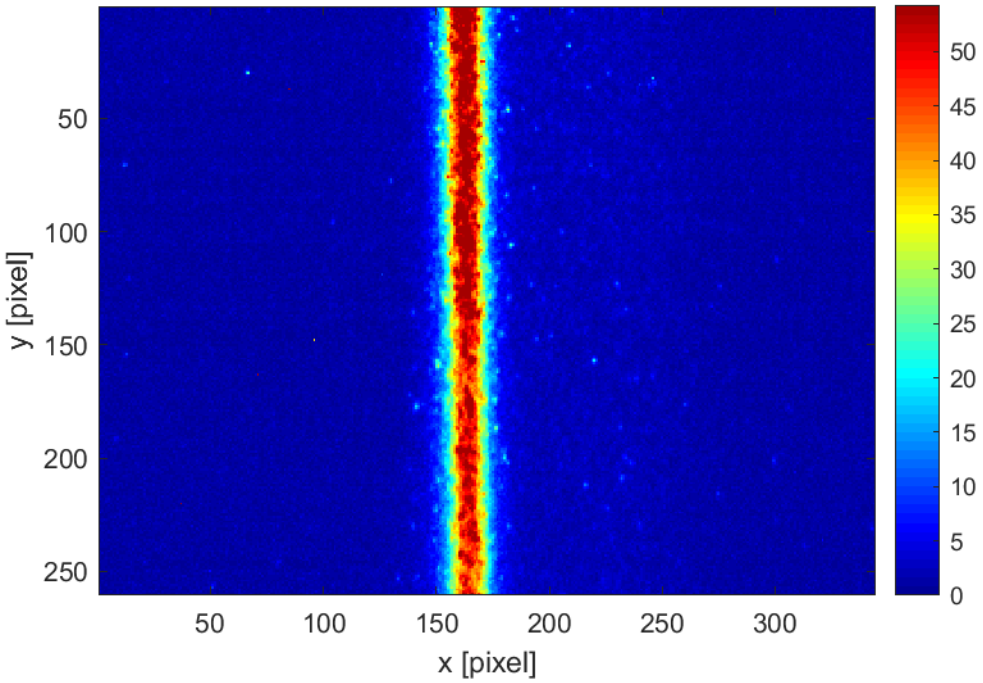

Figure 4.11 Example of a raw image of the tracer luminescence induced by laser beam.

For the current experiments, the IRO amplification is always set at its maximum for phosphorescence signal acquisition (delay time $t > 5ns$), which means $G = 100\%$. The signal to

noise ratio (SNR) is increased by averaging a large number of images. The CCD exposure time t_{CCD} is defined indirectly by the quantitative value of N_l and the laser repetition rate. The whole acquisition time is thus determined by t_{CCD} times N_i. A typical acquisition example is given in Figure 4.11 which images the luminescence emission of pure acetone vapor at p = 2 kPa for a delay time $t = 7.5\,\mu s$, $N_l = 100$, $N_i = 30$, $\Delta t_{gate} = 100\,ns$, and G = 100% with a laser repetition rate of 20 Hz. In these conditions $t_{CCD} = 5\,s$, and the total image recording time is $t_{CCD} \times N_i = 150\,s$.

4.3.3 Image post-processing procedure

In this work the number of laser shots per images was $N_l = 100$, and the averaged images per experiment was $N_i = 30$. The duration of a single signal acquisition (IRO shutter open), or gate time, was set to $\Delta t_{gate} = 500\,ns$, while the IRO amplification gain was set to $G = 100\%$.

As shown in our previous work [35; 99], the emitted signal distribution after excitation corresponds to the light distribution of the laser beam, which corresponds to a Gaussian profile

$$f(x,t) = a_1(t) + \frac{a_2(t)}{\sqrt{2\pi a_3(t)}} e^{-\frac{(x-a_4)^2}{2a_3(t)}}, \tag{4.2}$$

where a_1, a_2, a_3, and a_4 are the fitting parameters of the Gaussian function [93]. The $a_1(t)$ parameter represents background emission offset caused by excited tracer molecules out-of-beam or adsorbed by the internal walls, which is never zero and decreases in time. Coefficient $a_2(t)$ stands for the amplitude of the Gaussian signal, whose time evolution is strictly linked to the phosphorescence lifetime of the excited tracer, the variation of this parameter in time is also affected by the diffusion mechanisms. Parameter $a_3(t)$, which can be considered as the most important parameter of these experiments in this chapter, corresponds to the variance of the Gaussian function and its evolution in time gives information about the diffusion rate of the excited tracer molecules. This parameter directly represents how the tagged line profile is broadening with time. Finally, parameter a_4 represents the position of the Gaussian peak. The value of a_4 can slightly differ in each acquisition, caused by the possible small fluctuations in the position of the laser beam and small undulations in the laser energy evolution [93], the accurate measurement of $a_4(t)$ is underlying for the MTV technique.

Another parameter of interest is the Gaussian peak value, which corresponds to the highest intensity of the photoluminescence signal at every instant, and it can be defined as

$$S_{max} = f(a_4, t) = a_1(t) + \frac{a_2(t)}{\sqrt{2\pi a_3(t)}}, \tag{4.3}$$

From Eq. (4.3) we can notice that at a certain t, the Gaussian peak value is mainly based on the a_1, a_2, a_3. The Gaussian peak is mainly affected by the phosphorescence lifetime and diffusion effect; thus, this parameter can give us important information on the exploitable signal on the full measured pressure range.

Inside the visualization chamber, the laser was focused to a 175 μm beam waist. The beam diameter was determined by the full width at half maximum (FWHM),

$$\text{FWHM} = 2\sqrt{2\ln 2 a_3(t)}, \tag{4.4}$$

which was calculated via the signal acquisition of the fluorescence distribution at the beginning of the experiment ($t = 5ns$).

An example of diffusion measurements at constant pressure via the molecular tagging technique at different instants is presented in Figure 4.12. Via this optical technique it was possible to follow in time the emitted light of acetone molecules and to measure its evolving distribution with time due to diffusion effects. The acquired raw images are shown in the odd-numbered rows of Figure 4.12, while the post-treated Gaussian profiles are shown in the even-numbered rows. The Gaussian profiles were obtained by averaging the signal acquired by every pixel along the y-direction. This procedure decreased the statistical fluctuations of the light emission distribution. As a matter of example, at $p = 1000\ Pa$ the FWHM beam diameter evolved due to diffusion from around 175 μm at $t = 0.005\ \mu s$ to around 1376 μm at $t = 500\ \mu s$.

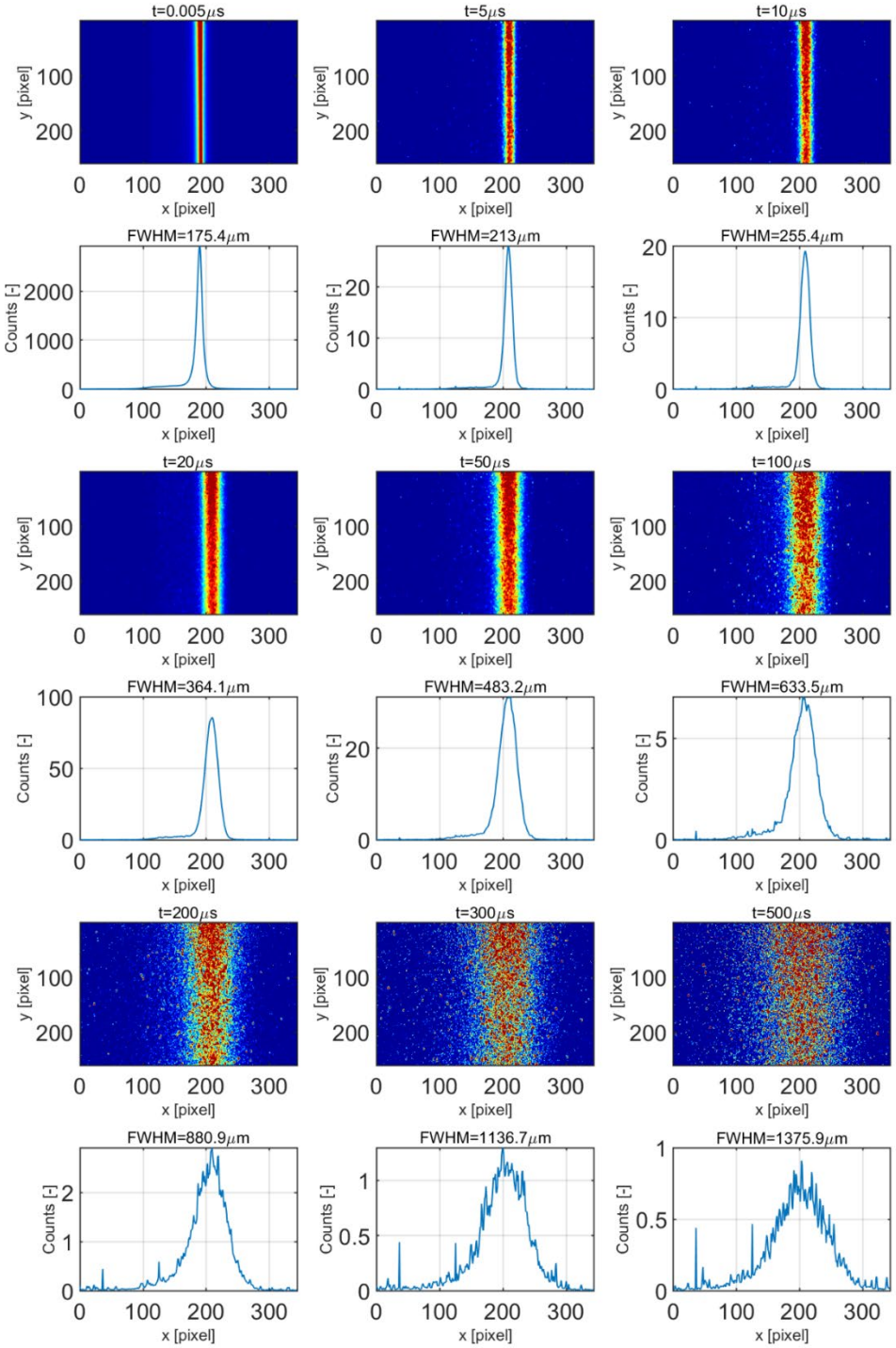

Figure 4.12. Temporal evolution of photoluminescence signal images and corresponding light distribution profile (blue solid line) for p = 1000 Pa.

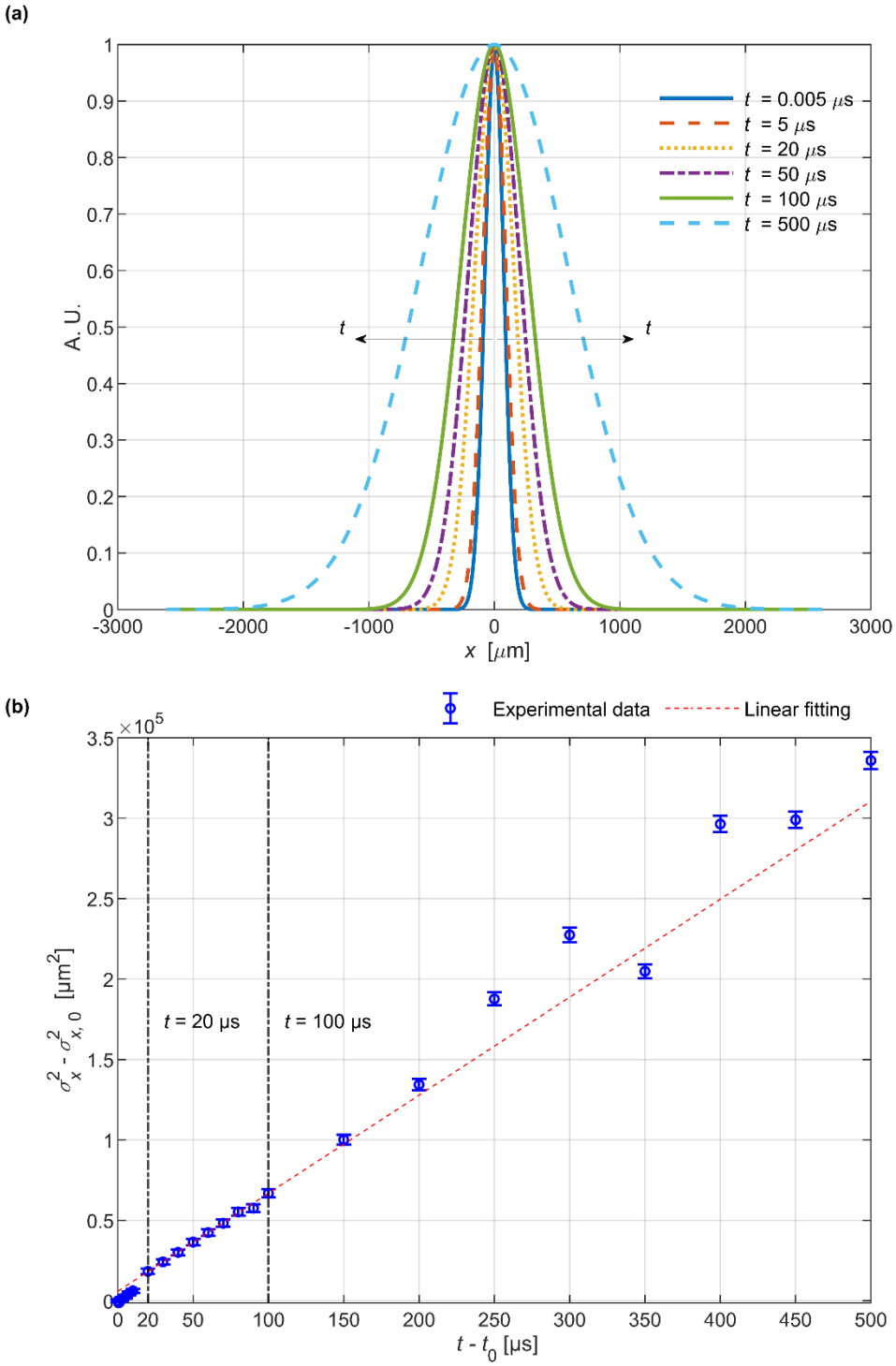

Figure 4.13. Experimental results at $p = 1$ kPa. (a) Gaussian fitting of the emission profile evolution with time normalized by each Gaussian peak; (b) linear fitting to variance variation over time from Figure 4.13 (a).

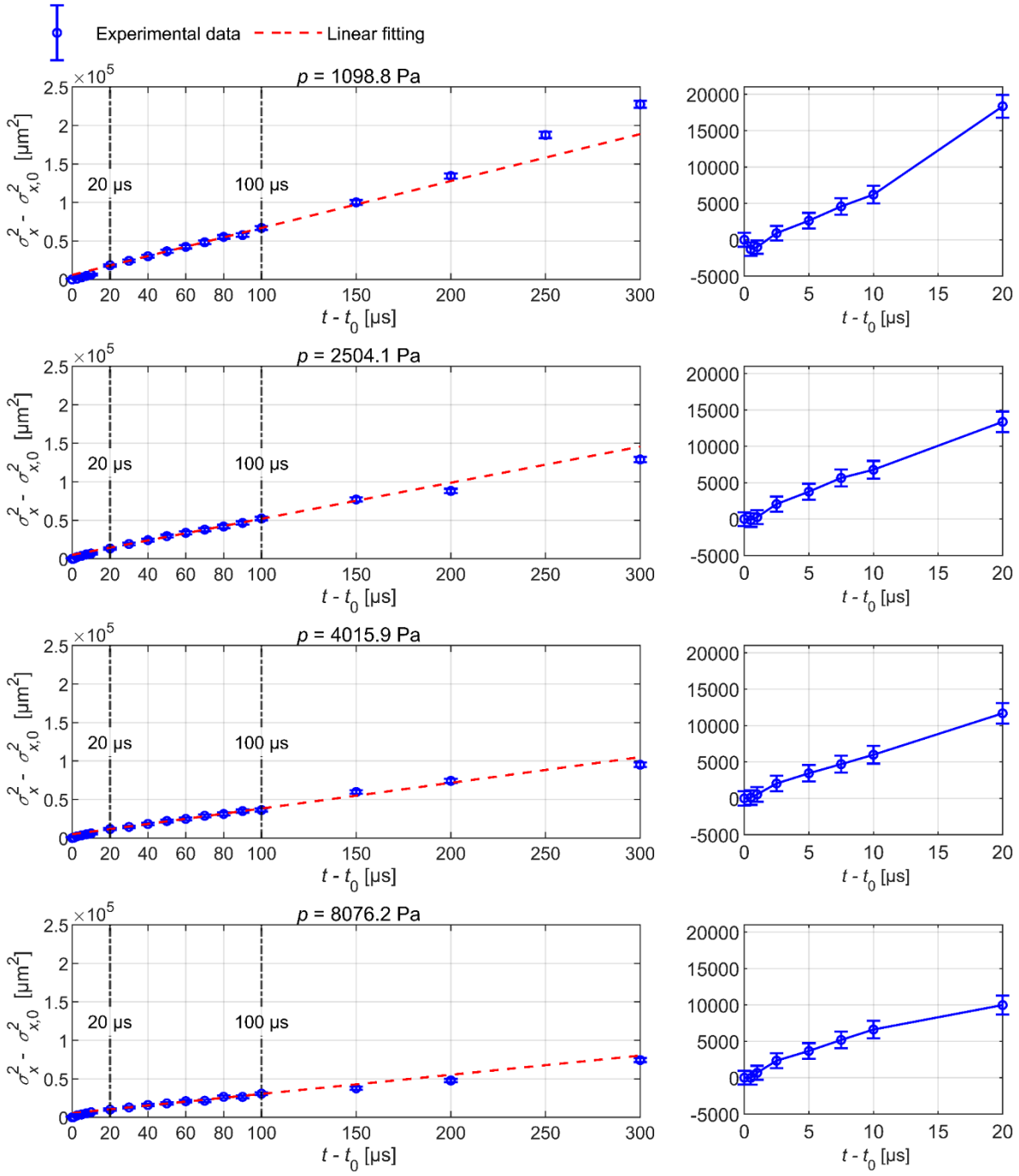

Figure 4.14. Temporal evolution of variance and corresponding linear fitting for different pressures p = 1 kPa , 2.5 kPa, 4 kPa and 8 kPa. Left: up to a delay time of 300 µs; Right: zoom on the early delay times up to 20 µs..

The diffusion coefficient calculation was realized through the Einstein-Brownian motion equation, which relates the diffusion coefficient to the evolution with time of the variance of the tagged molecules distribution of the tagged line, as

$$\sigma_x^2(\mathrm{t}) = 2D_m(t - t_0) + \sigma_{x,0}^2, \tag{4.5}$$

where $\sigma_x^2(\mathrm{t}) = a_3(t)$ is the variance evolution with time, D_m represents the measured results of diffusion coefficient, t is the time after the laser excitation, $\sigma_{x,0}^2$ is the variance of the initial light distribution at $t = t_0$ [126]. This equation implies that the variance should evolve linearly with time, with a slope proportional to the diffusion coefficient. Therefore, the experimental results of diffusion coefficient can be extracted from the slope of the linear fitting to the temporal evolution of variance. As an example, Figure 4.13 (a) illustrates the variation with time of the tagged line distribution at constant pressure p = 1 kPa from the time of tagging to 500 µs later. The Gaussian shape is modified in time by molecular diffusion. A linear fit is then used in order to characterize the variance evolution with time and thus extract diffusion.

4.4 Measurement results of diffusion coefficients and kinetic diameter

4.4.1 Linear evolution of variance over time

The Gaussian distribution fitting equation (Eq.(4.2)) was applied to the experimental acquisitions of the tagged line at different instants for a large pressure range. To the best of our knowledge, the time range of phosphorescent signal acquisitions presented in this work is the longest one currently available in the literature for such a wide range of low pressures. In Figure 4.13 (a), the results are presented by normalizing the acquired signal with the peak value of the Gaussian distribution (S_{max}) at each time delay. From the Gaussian fitting, it was possible to extract the variance at different times, $\sigma_x^2(\mathrm{t}) = a_3(t)$. As shown in Figure 4.13 (b), a linear equation was then used to fit the variance evolution with time, which slope can be directly linked to the diffusion coefficient. The experimental results verify for a wide temporal range the linear behaviour of the variance evolution with time, as predicted by the Einstein-Brownian (Eq.(4.5)).

The same method was applied to a wide pressure range, demonstrating the efficiency of the technique (Figure 4.14).

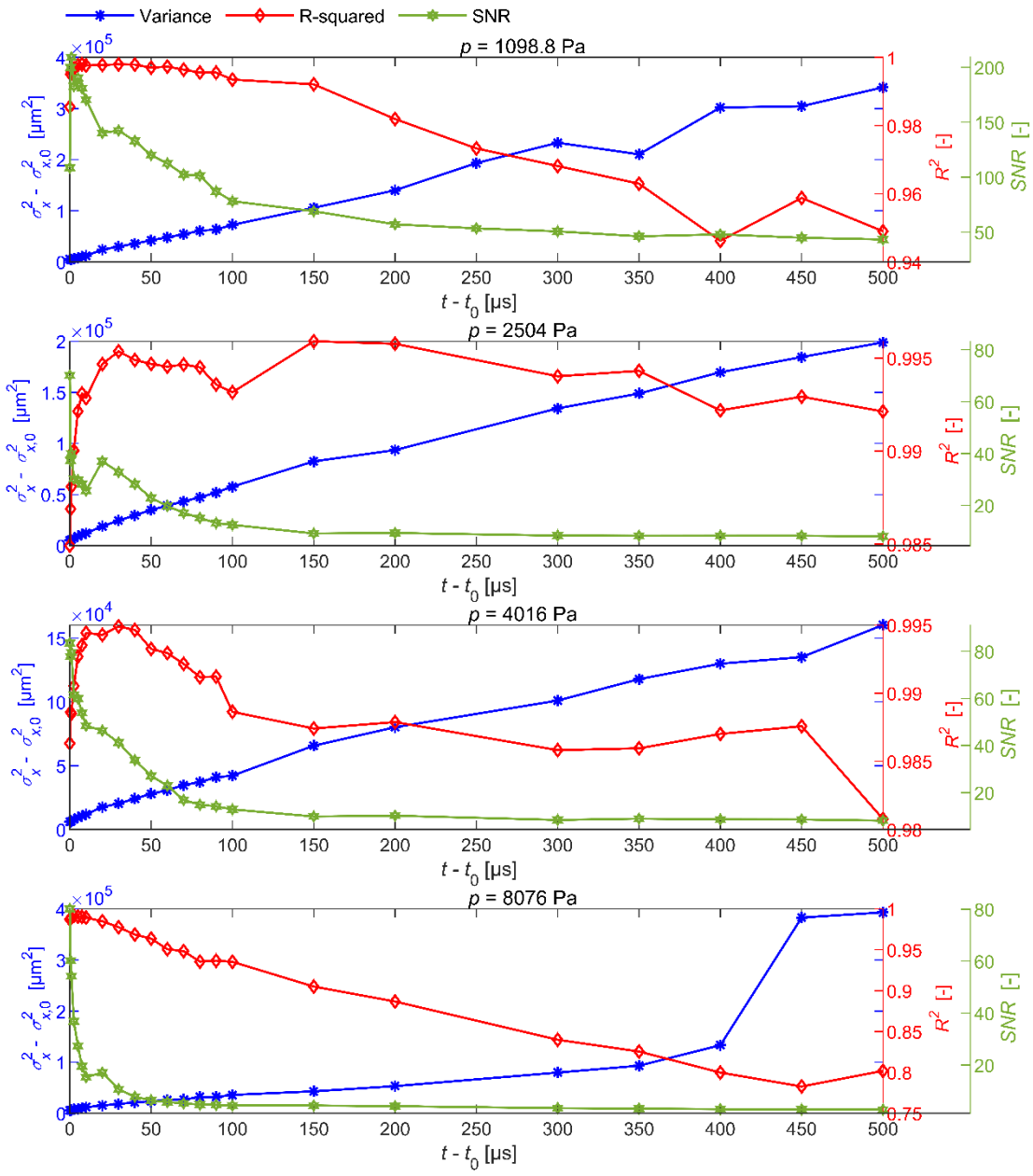

Figure 4.15. Temporal evolution of variance, R^2 and SNR at p = 1 kPa, 2.5 kPa, 4 kPa and 8 kPa.

4.4.2 The quality of Gaussian fitting and light emission image

A regression model was used to fit the Gaussian equation to the signal distribution, the parameter R-squared (R^2) was employed to evaluate the quality of the fit [127]

$$R^2 = 1 - \frac{SSE}{SST}, \tag{4.6}$$

where SSE represents the Sum of Squared Errors, SST is the Sum of Squares Total. SSE is the sum of the squared differences between the actual experimental results and predicted fitted results. SST is a statistical term, defined as the sum of squared differences between the practical dependent variables and its overall mean. The value of R^2 can range between 0 and 1, with R^2 = 1 corresponding to a perfect match between experimental data and the fitting function. For all pressures investigated, the experimental sample size $n_x = 344$, which is the number of pixels along the x-axis direction of the image, was constant. The $x - axis$ corresponded to the transversal direction in respect to the laser beam trajectory. Some researchers [128; 129] have suggested that the adjusted R-squared value is a more accurate fitting evaluation parameter as an improved version of R-squared,

$$Adjusted\ R^2 = 1 - (1 - R^2)\frac{n_x - 1}{n_x - n_{iv} - 1}, \tag{4.7}$$

where n_x is the sample size, and n_{iv} is the number of independent variables. For the experimental data discussed in this chapter, since n_{iv} = 1, the Adjusted R-squared and R-squared almost coincide to the same value.

The experimental signal to noise ratio was used, too, to estimate the quality of the acquired signal. In this chapter, SNR was defined as the ratio between the Gaussian peak S_{max} and the background emission offset of the image $a_1(t)$,

$$SNR(t) = \frac{S_{max}}{a_1(t)}. \tag{4.8}$$

The overall quality of the experimental data was evaluated based on the R^2 and SNR parameters. Low values of R^2 and SNR implied that the Gaussian fitting represented poorly the signal distribution and that the intensity of emitted light is too weak for obtaining reliable information from the acquired images, respectively.

As an example, Figure 4.15 summarizes the temporal evolution of the variance, R^2 and SNR at every instant of one experiment for four different pressures. As it can be seen from this figure, both the R^2 and SNR parameters decrease with time, and it was therefore necessary to delimit a time range of confidence where the quality of the acquired dataset could be considered exploitable for the full range of the investigated pressures. In the context of extracting the diffusion coefficient from the acetone phosphorescence signal, we have considered that the acquired data was trustworthy until 100 μs after the laser excitation for the whole set of experiments, which guarantees a minimum SNR of 2.1 and a minimum R^2 of 0.75 .

4.4.3 Triplet-triplet annihilation

In accordance with the Einstein-Brownian equation (Eq.(4.5)), for relatively low pressures, the experimental data provided a variance $\sigma_x^2(\mathrm{t})$ that evolved linearly with time, from the initial tagging instant onwards. Nevertheless, at higher pressure, a pronounced non-linear behavior of the variance with time was observed immediately after the initial tagging instant (Figure 4.14).

The non-linear behavior of the variance with time could be related to the occurrence of triplet-triplet annihilation (TTA), a phenomenon that consists in de-excitation of molecules in the triplet state via intermolecular collisions with other triplet molecules. This could explain why the non linear variation was more evident at higher pressures, since the collision frequency increases due to relatively high molecular concentration. The triplet state is a meta-stable energy level from which a molecule can transit to the ground state either through the emission of one photon (phosphorescence) or through a non-radiative de-excitation process, such as TTA. In the same way that oxygen is considered to be an efficient molecular quencher due to its paramagnetic characteristics, acetone or diacetyl in its tripelet state can produce self-quenching [102; 130].

It is possible to summarize the specific light-induced reaction pathways of acetone vapor after laser excitation:

$$\mathrm{Ac} + h\nu \rightarrow \quad {}^1\mathrm{Ac}, \tag{4.9a}$$

$${}^1\mathrm{Ac} \rightarrow \mathrm{Ac} + h\nu_{\mathrm{f}}, \tag{4.9b}$$

$${}^1\mathrm{Ac} \rightarrow \quad {}^3\mathrm{Ac}, \tag{4.9c}$$

$${}^3\mathrm{Ac} \rightarrow \mathrm{Ac} + h\nu_{\mathrm{ph}}, \tag{4.9d}$$

$$^3\mathrm{Ac} + Q \rightarrow \mathrm{Ac}, \tag{4.9e}$$

$$^3\mathrm{Ac} + \quad ^3\mathrm{Ac} \rightarrow \mathrm{Ac}^* + \mathrm{Ac}, \tag{4.9f}$$

where Ac represents the acetone molecules in ground state, ^{1}Ac, ^{3}Ac, Ac* corresponds to acetone molecules in the singlet state, triplet state, and ground vibrational state; hv, hv_{f}, hv_{ph} represent the energy absorbed from the laser shot, emitted light in the form of fluorescence and phosphorescence, respectively; Q can be considered as another molecular species, such as oxygen .

After laser exication, acetone molecules at the ground-state are excited to a singlet-state energy level (Eq.(4.9a)). A portion of this excited molecules will emit fluorescence and come back to the ground-state (Eq.(4.9b)). A portion of the excited molecules in the singlet-state will transfer to a triplet-state energy level through intersystem crossing transitions (Eq.(4.9c)). A portion of triplet molecules will choose to emit phosphorescence and come back to the ground-state (Eq.(4.9d)). Other triplet molecules will be quenched by other molecular species, such as oxygen and come back to ground state (Eq.(4.9e)). While other triplet molecules will come back to its ground vibrational state and ground-state after colliding with other triplet molecules (Eq.(4.9f)) (triplet-triplet annihilation).

To the best of our knowledge, the influence of TTA on the light distribution evolution with time from an initial Gaussian distribution still remains unexplored for gaseous acetone, while some work has been conducted for diacetyl vapor [27]. Due to their similar molecular structure, diacetyl can be considered as an adequate reference for acetone. In [27] a theoretical model was proposed for predicting the light emission distribution after molecular tagging in the case of diacetyl vapor by considering several de-excitation processes, including TTA. The model considered radiative de-excitation (phosphorescence), quenching generated by inter-species collisions (usually oxygen) and self-quenching generated by triplet acetone molecules collisions. The time evolution of the triplet population concentration was defined as

$$\frac{\partial n_{T_1}}{\partial t} = -k_1 n_{T_1} - k_{TTA} n_{T_1}^2 + D\nabla^2 n_{T_1}, \tag{4.10}$$

where n_{T_1} represents the temporal concentration of triplet acetone molecules, $k_1 = k_{ph} + k_{nr,T_1} + n_Q k_Q$ represents the rate constant of linear decay, comprising radiation k_{ph} and quenching caused by molecular collisions between acetone molecules k_{nr,T_1}(Internal non-radiative rate constant in

the triplet state) and other species k_Q, n_Q indicates the concentration of other molecular species, k_{TTA} is the triplet-triplet annihilation reaction, D is the diffusion coefficient. The value of k_{TTA} for acetone vapor, has not been found out in the literature.

Due to the non-linear TTA term, this equation cannot be reduced to the Einstein-Brownian equation which considers a linear variance evolution with time. That is why for low pressures, the $k_{TTA}n_{T_1}^2$ term becomes weaker faster. Sidebottom et al. [131]pointed out that also high laser energies could increase the triplet population, being this a catalyser for TTA. Thus, in order to avoid a nonlinear variation of the variance with time, low pressures and low laser energies are needed. In respect to the current experimental work, the non linear variation with time of variance tended to disappear after some time. Diffusion in this case had a positive effect since it diluted with time the concentration of triplet molecules close to the initial tagged line. In the current study it was observed that the non linear variation lasted until 20μs from the initial tagging line for all pressures. For low pressures the detected non-linear range was shorter, or even non detectable for the lower pressures. This observation coincided with the work of Mirzaei et al [27].

4.4.4 Local heat releasement in molecular tagging

Another potential factor of interest to be considered for explaining the non-linear behavior is the influence of temperature increase due to molecular absorption at the laser shot. The presence of local gas heating caused by laser absorption has been witnessed in several techniques, such as air photolysis recombination tracking (APART) [132], vibrationally excited nitrous oxide (NO) monitoring (VENOM) [133], ozone tagging velocimetry (OTV) [91], Raman excitation plus laser-induced electronic fluorescence (RELIEF) [90] and femtosecond laser electronic excitation tagging (FLEET) [134; 135]. The energy absorbed by the molecule is dissipated via heat generation due to inter-molecular collisions, electronic excitation, dissociation [136], and chemical reactions [137]. Local heat depends on the tracer molecular species, that is the absorption spectra and the different excitation processes (e.g. energy transformation rate between internal and translational degree of freedom), laser energy density [138] and collision frequency [137].

The work of Limbach et al. [135] verified there was a correlation between the temperature rise caused by local heating and the beam width widening, changes in the evolution with time of

the spatial profile of the beam and the signal intensity. They also proposed that at early time (first microseconds), the widening of tagged line is mainly dominated by hydrodynamic expansion, which verifies the linear correlation between line widening and initial temperature rise. The local heat can also create flow perturbation, such as shock waves and a high-temperature area with low density. This is why, low-energy laser pulses should be preferred in order to avoid local heat [111; 135]. The enhanced beam waist of [26] can be associated to the increasing laser energy in the work of DeLuca et al. [139]. Beam width widening and larger temporal widening of tagged line was also verified by Bominarr et al.'s work [137]. This unexpected beam width increase was also due to vertical convection engendered by density gradients in the gas. This work also mentioned that the temperature rise was the reason for the variance of gaussian profile of tagged line evolves nonlinearly with time at high pressures and early delay time. This experimental finding has highly agreement with the non-linear behavior in our experimental results.

Burns et al. [140] verified that buoyancy caused by local heat had no substantial effect on the velocity or trajectories measurement by PLEET, and only vertical velocity were slightly altered but with a 1000 K temperature rise. The buoyancy had no impact on the PLEET signal, and the lifetime of PLEET signal had an inverse correlation with pressure and temperature. The work of New-Tolley et al. [141] verified that the local heat effect on velocity measurement by FLEET can be neglected in boundary layer of laminar flow, however, numerical work pointed out that it can be a partial reason of an artificial increase of the thickness of shear layer.

Since temperature variations modify molecular diffusion (Eq. 4.1), the temperature rises generated by laser beam absorption increase the speed at which the variance evolves with time [137]. This conclusion corroborates the findings of our work, for which we observed a rapid increase of the variance immediately after the laser excitation. Nevertheless, this effect may be relevant only for the first few microseconds following the excitation since the temperature rise is limited [142] and the heat is rapidly dissipated through intermolecular collisions, especially at relatively high pressure.

4.4.5 Effective time internal choice

In the current work, experimental data showed that the non-linear trend for the variance disappeared after a certain time. This can be explained by the diffusion of the excited molecules towards the outskirts of the initial tagged line, which locally decreases the triplet population, thus reducing the strength of the TTA phenomenon. Also, the initial local temperature rise drops back to ambient temperature. Hence, after analyzing the entirety of the dataset at our disposal, it was concluded that the non-linear effects vanished after 20 μs after laser excitation for the here studied pressure range. This time interval is in agreement with the findings of [103; 142].

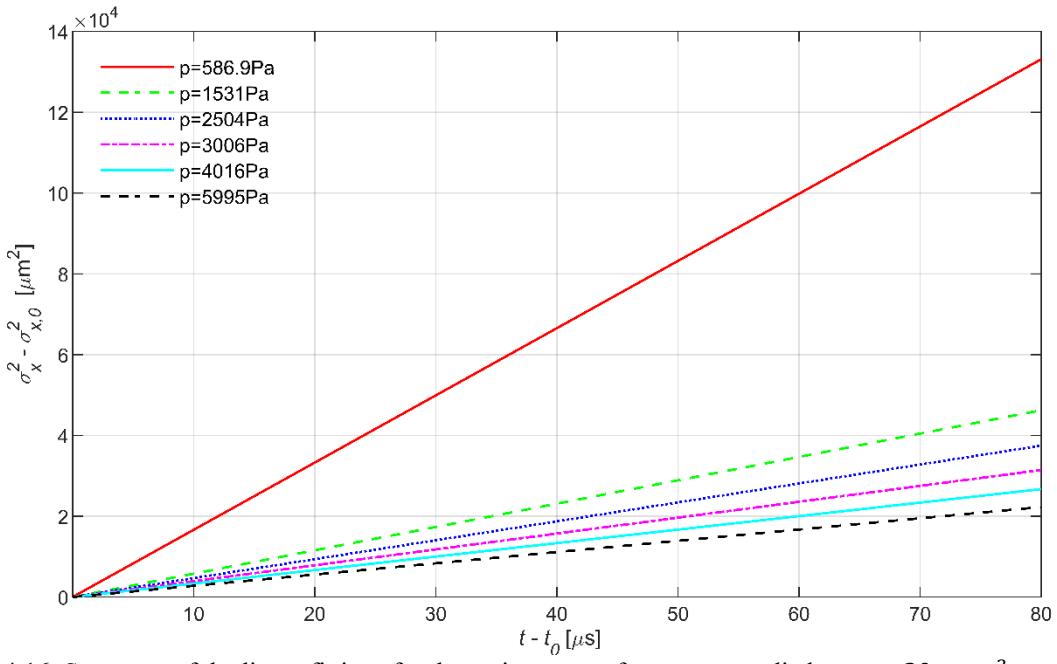

Figure 4.16. Summary of the linear fittings for the entire range of pressures studied at $t_0 = 20\ \mu s$, $\sigma_{x,0}^2 = \sigma_x^2(t_0 = 20\mu s)$.

In order to define the upper time limit to be used for the diffusion coefficient measurement. The SNR and R-squared parameters were used. The upper limit was chosen to be 100 μs. This is in accordance with the characteristic lifetime of phosphorescence which can be defined by

$$\tau_{T_1} = \frac{1}{\mathrm{k}_{ph} + k_{Q,T_1} + k_{nr,T_1}}. \tag{4.11}$$

For both acetone [143] and diacetyl [131], the typical time of phosphorescence is around $\tau_{ph} = 1/k_{ph} = 10\,ms$. However, for acetone, the lifetime τ_{T1} of the phosphorescence emission and, equivalently, of the triplet population is approximately 200 μs [95]. In the work of Kaskan & Duncan [97], the experimental data of phosphorescence lifetime of acetone vapor is between 200 and 250 µs, which varies with different pressures because of TTA. In a conclusion, the value of phosphorescence lifetime for acetone vapor is around 200 μs, which is quite close to the upper limit of our effective time internal.

Based on these considerations along with those of the previous paragraph, we selected the time range 20-100 µs that follows the laser excitation as the time interval for which the non-linearity on the variance can be considered negligible and the quality of the images is high enough for the purpose of measuring the variance of the signal.

By fitting Eq. (4.5) to the variance evolution with time measurements in the 20-100 µs time range (Figure 4.14), the self-diffusion coefficient of acetone was extracted for pressure values between 500 Pa and 10 kPa. The considered time range contains 9 data points for the variance at each pressure but for the sake of completeness we reported in (Figure 4.14) the extended dataset of the measured variance, from 5 ns to 300 µs. It can be noticed that the measurements are of high quality until 100 µs, since they respect the acquisition ranges established by R^2 and SNR. While for delay times larger than 100 µs the measured variance is characterized by larger fluctuations. A summary of the linear fitting functions measured for a larger range of pressure was presented in Figure 4.16. Let us remind here, that the slope of the linear fitting is directly proportional to the diffusion coefficient.

4.4.6 Measurement results of diffusion coefficient and kinetic diameter

The diffusion coefficient (D_m) was computed from the linear fitting slope measurement via the Einstein-Brownian equation (Eq.(4.5)). Thus, the calculation formula for the measured value of diffusion coefficient was defined as

$$D_m = \frac{\sigma_x^2 - \sigma_{x,0}^2}{2(t - t_0)}. \tag{4.12}$$

The experimental results of D_m were presented in Figure 4.17(a), which are compared with the theoretical predictions obtained from the Chapman-Enskog equation (Eq.(4.1)) by using the kinetic diameter values found in the literature (Table 4.1). The data is presented in a logarithmic scale, and the slope of dashed lines corresponds to a dependency *1/p* of the diffusion coefficient with the pressure. The results show that the diffusion coefficient decreased with pressure for most of the pressure range considered, but the monotonicity of D_m is lost for about $p > 5$ kPa. The measured diffusion coefficient also showed a linear behavior (in logarithmic scale) for 1 kPa < p < 5 kPa, but with a slope that is different than the Chapman-Enskog theory. Instead of being proportional to p^{-1} , the measured D_m resulted to be a different power law of the pressure, i.e., p^a with $0 > a > -1$. This unexpected behavior could be the result of more complex intramolecular phenomena that occur following the laser, such as the TTA or local heating. This behavior can also be related to the uncertainty of the measurement.

From the measured diffusion coefficient values and Chapman-Enskog equation (Eq.(4.1)) it was possible to indirectly extract the kinetic diameter (d_m) of gaseous acetone,

$$d_m = \sqrt{\frac{3\sqrt{\pi}}{8}\sqrt{\frac{k_B\,T}{m}}\frac{k_B T}{\sqrt{2}\pi D_m p}}\,, \tag{4.13}$$

where both p and temperature T can be assumed as constant during one experiment.

The indirect experimental measurements of kinetic diameter of acetone vapor for each measured diffusion coefficient were demonstrated in Figure 4.17 (b). Since D_m does not follow the expected trend, d_m is not constant with pressure. Nevertheless, it can be observed that at lower pressures ($p \leq 5$ kPa) the measured d_m is within the range of acetone kinetic diameter values reported in the literature. Only for pressures $p > 5$ kPa the measured D_m are higher than the values calculated with the smallest kinetic diameter available from the literature, d = 416 pm [23].The mean $d_{m,avg}$ of all measured kinetic diameter d_m is 436 pm, which is in good agreement with the predictions of [123] and [125]. The relatively large discrepancies on the diffusion coefficients recorded in the high-pressure range could be due to the inaccuracies related to the non-linear

behavior of the variance evolution with time. At higher pressures, molecular diffusion is smaller and the variation in time of the signal profile's variance changes slower in time.

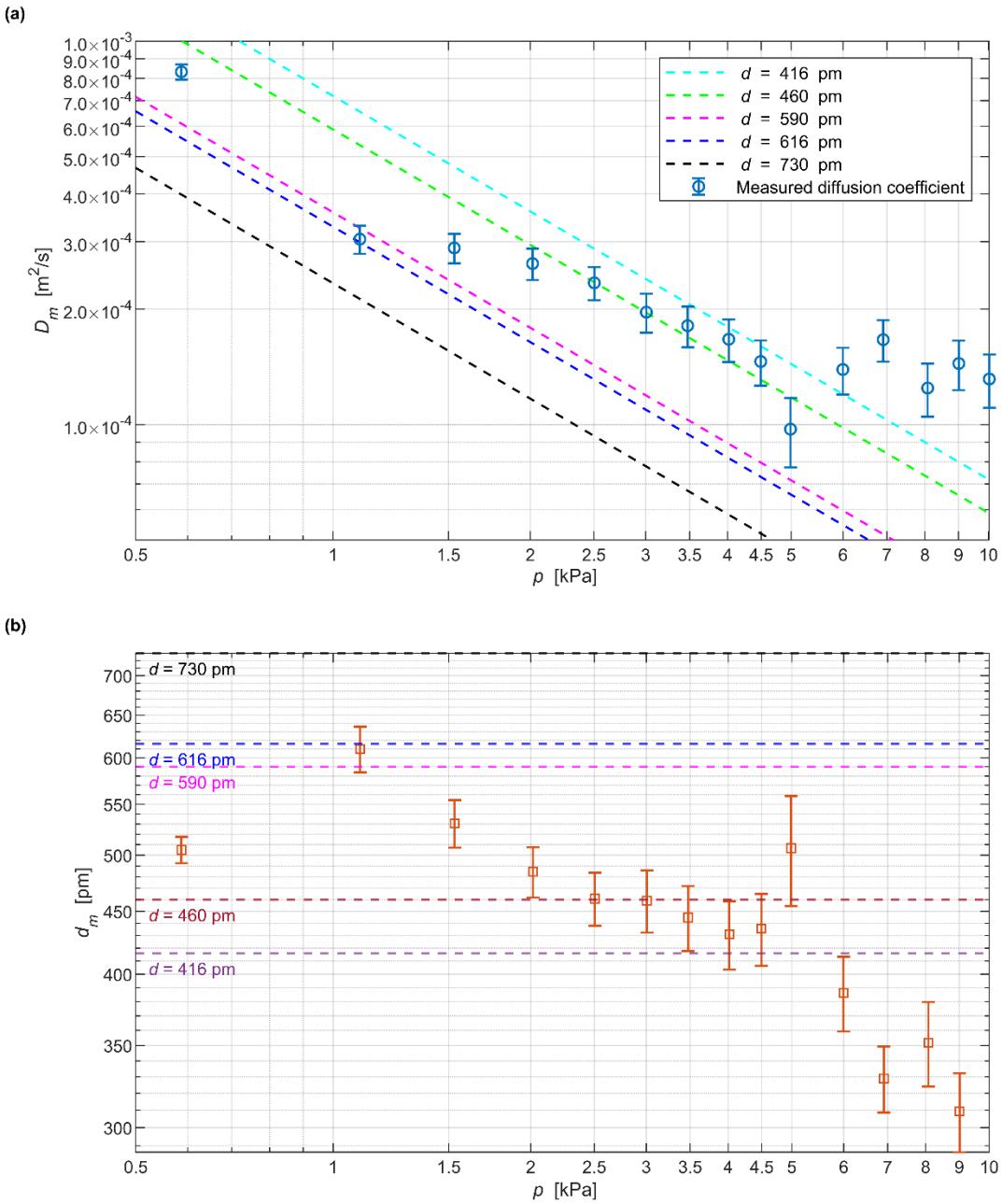

Figure 4.17. (a) Measured diffusion coefficient D_m (blue circles) as a function of the pressure compared to the corresponding theoretical values (dashed lines) in logarithmic scale; (b) kinetic diameters d_m calculated from D_m by means of the Chapman-Enskog equation (orange squares) as a function of the pressure and compared to the values (dashed lines) found in the literature (Table 4.1) in logarithmic scale.

4.4.7 Uncertainty calculation of the measured parameters

The spatial resolution of CCD is known as 15.2 μm, the resolution error ϵ_R is 0.5*15.2 = 7.6 μm. The tagged line width can be represented by FWHM of the peak. The FWHM is defined as the difference of the position x_1 and x_2, whose corresponding value $f(x_1)$ and $f(x_2)$ is half of Gaussian peak $f(x)_{max}$. The FWHM is also related to standard deviation according to

$$\mathrm{FWHM} = x_2 - x_1 = 2\sqrt{2\ln 2}\,\sigma_x. \tag{4.14}$$

The uncertainty of the position x_1 and x_2 is ϵ_R, separately. Based on the propagation of uncertainty principle [144], the uncertainty of FWHM can be defined as

$$\epsilon_{\mathrm{FWHM}} = \sqrt{2}\,\epsilon_R = \Delta\left(2\sqrt{2\ln 2}\,\sigma_x\right). \tag{4.15}$$

We can derive the uncertainty of standard deviation (ϵ_{σ_x})

$$\epsilon_{\sigma_x} = \frac{\epsilon_R}{2\sqrt{\ln 2}}. \tag{4.16}$$

We assume that variance measured at different delay time is uncorrelated. Following the propagation of uncertainty principle, the uncertainty of variance $\epsilon_{\sigma_x^2}$ can be expressed by:

$$\epsilon_{\sigma_x^2} = \left|\frac{d\left(\sigma_x^2(\mathrm{t})\right)}{d\left(\sigma_x\ (\mathrm{t})\right)}\right| \epsilon_{\sigma_x} = |2\sigma_x(t)|\epsilon_{\sigma_x}. \tag{4.17}$$

The uncertainty of variance at $t = t_0$ is

$$\epsilon_{\sigma_{x,0}^2} = \left|2\sigma_{x,0}\right|\Delta\left(\epsilon_{\sigma_x}\right). \tag{4.18}$$

The uncertainty of variance difference can be defined as

$$\epsilon_{\sigma_x^2(\mathrm{t})-\sigma_{x,0}^2} = \sqrt{\epsilon_{\sigma_x^2}^2 + \epsilon_{\sigma_{x,0}^2}^2} = 2\epsilon_{\sigma_x}\sqrt{\sigma_x^2(\mathrm{t}) + \sigma_{x,0}^2}. \tag{4.19}$$

The relative uncertainty of variance difference decreases as the value of the variance difference increases. From Figure 4.14, we can see that the value of the variance difference tends to increase linearly with time. Thus, the relative uncertainty of the variance difference decreases with increasing time at each pressure. As the diffusion coefficient value decreases with increasing pressure, the order of magnitude of the variance difference decreases with increasing pressure (Figure 4.14). The relative uncertainty of the variance difference increases with pressure.

It can be concluded that the relative uncertainty of the measured variance difference is negatively correlated with time and positively correlated with pressure. This tendency is reasonable. The uncertainty in variance difference is based on the spatial resolution of the CCD and temporal precision from PTU. The resolution ability of the apparatus is fixed, and as the measurement value becomes larger, the resolution accuracy becomes higher. This relative uncertainty of variance and time difference also supports our choice to choose effective data at high delay time and low pressures.

It is known that the delay time has an accuracy of 5 ns, corresponding to the PTU's precision for synchronizing the temporal signals [35]. The uncertainty of delay time can be assumed as $\epsilon_t =$ 5 ns. The delay time is also considered as an uncorrelated variable. The minimum uncertainty of time difference can be expressed as:

$$\epsilon_{\mathrm{t-t_0}} = \sqrt{\epsilon_t^2 + \epsilon_{t_0}^2} = \sqrt{2}\epsilon_t. \tag{4.20}$$

Since the measured diffusion coefficient is determined by the slope of the variance difference over the time difference (Eq.(4.12)). The uncertainty of the slope is determined by the maximum uncertainty range of slope defined within the uncertainty range of variance difference and time difference. The upper border of the slope uncertainty can be defined as maximum value of $\sigma_x^2(\mathrm{t}) - \sigma_{x,0}^2$ over the minimum value of $t - t_0$

$$slope_{up} = \frac{\sigma_x^2(\mathrm{t}) - \sigma_{x,0}^2 + \epsilon_{\sigma_x^2(\mathrm{t})-\sigma_{x,0}^2}}{t \quad - t_0 - \sqrt{2}\epsilon_t}. \tag{4.21}$$

Similarly, the lower border value of the slope uncertainty can be expressed as:

$$slope_{low} = \frac{\sigma_x^2(\mathrm{t}) - \sigma_{x,0}^2 - \epsilon_{\sigma_x^2(\mathrm{t})-\sigma_{x,0}^2}}{t \quad - t_0 + \sqrt{2}\epsilon_t}. \tag{4.22}$$

An example the slope uncertainty border is shown in Figure 4.18. The relative uncertainty of slope can be defined as:

$$U_{r,slope} = \frac{slope_{up} - slope_{low}}{2slope}. \tag{4.23}$$

The relative uncertainty of measured diffusion coefficient can be expressed as:

$$U_{r,D_m} = \frac{1}{2} U_{r,slope}. \tag{4.24}$$

The relative uncertainty of diffusion coefficient (U_{r,D_m}) at each pressure is summarized in Table 4.5.

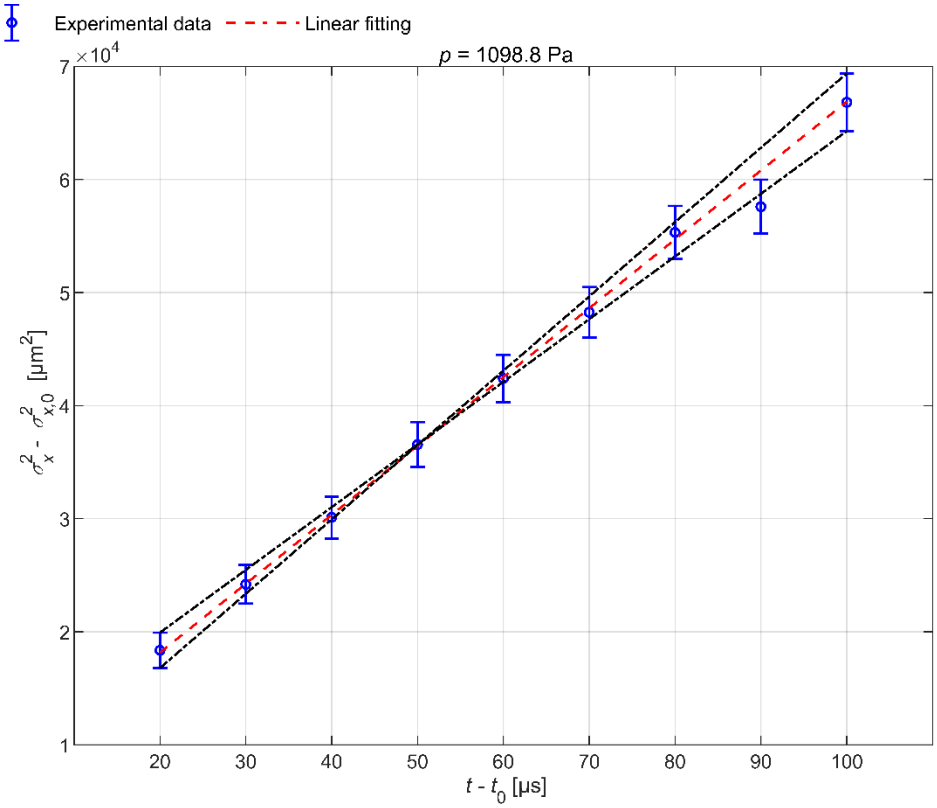

Figure 4.18. An example to show the measured slope (red dashed line) and its possible upper and lower border of uncertainty range (black dotted line) at p = 1 kPa.

The calculation of measured kinetic diameter can be expressed as

$$d_m = \sqrt{\frac{3\sqrt{\pi}}{8}\sqrt{\frac{k_B\,T}{m}}\frac{k_B T}{\sqrt{2}\pi D_m p}} = c_d T^{0.75} D_m^{-0.5} p^{-0.5}, \tag{4.25}$$

where c_d is a constant

$$c_d = \sqrt{\frac{3}{16}\sqrt{\frac{2k_B^3}{\pi m}}}.$$

Table 4.5. Measured quantities with corresponding relative uncertainty.

$p \pm U_{r,p}$([Pa])	$D_m \pm U_{r,D_m}$([m2/s])	$d_m \pm U_{r,d_m}$([pm])
587.0 ± 1.93%	0.000832 ± 4.55%	505.0 ± 2.47%
1098.8 ± 1.33%	0.000305 ± 8.46%	610.0 ± 4.28%
1530.9 ± 0.634%	0.000289 ± 8.86%	530.6 ± 4.44%
2015.6 ± 0.362%	0.000263 ± 9.4%	484.7 ± 4.71%
2504.1 ± 0.411%	0.000234 ± 9.92%	460.8 ± 4.97%
3006.4 ± 0.173%	0.000197 ± 11.6%	459.2 ± 5.81%
3475.3 ± 0.236%	0.000181 ± 12.1%	444.8 ± 6.07%
4015.9 ± 0.0523%	0.000167 ± 12.7%	431.0 ± 6.37%
4493.0 ± 0.145%	0.000146 ± 13.5%	435.6 ± 6.75%
4988.1 ± 0.00601%	0.0000973 ± 20.6%	506.6 ± 10.3%
5995.3 ± 0.0367%	0.000139 ± 14%	386.3 ± 6.99%
6909.0 ± 0.256%	0.000167 ± 12.4%	329.0 ± 6.21%
8076.2 ± 0.197%	0.000125 ± 15.8%	351.9 ± 7.92%
9011.6 ± 0.183%	0.000144 ± 14.8%	309.4 ± 7.39%
10028.3 ± 0.164%	0.000132 ± 15.9%	307.3 ± 7.97%

Based on the propagation of uncertainty principle, the relative uncertainty of measured kinetic diameter can be defined by:

$$U_{r,d_m} = \sqrt{\left(0.75U_{r,T}\right)^2 + \left(0.5U_{r,D_m}\right)^2 + \left(0.5U_{r,p}\right)^2}, \tag{4.26}$$

where U_{r,d_m}, $U_{r,T}$, and $U_{r,p}$ represent the relative uncertainty of measured kinetic diameter, temperature, and pressure, separately. The temperature is the measured room temperature of the thermostat room, whose uncertainty is constant at 0.5 K. The value of $U_{r,T}$ keeps constant as 0.17%. Apart from the pressure sensor's uncertainty acetone vapour absorption and desorption should also be considered when estimating the pressure uncertainty. The uncertainty of pressure is defined as the standard deviation of pressure variation during image acquisition. As shown in Table 4.5, the

value of $U_{r,p}$ decreases with increasing pressure. The maximum value of $U_{r,p}$ is no more than 1.92%, quite smaller compared to the value of U_{r,D_m}. Thus, the tendency of U_{r,d_m} is mainly determined by U_{r,D_m}. As shown in Figure 4.17 (b) and Table 4.5, the value of U_{r,d_m} shows similar tendency like U_{r,D_m}, negatively correlated with pressure. The maximum value also occurs when pressure equals 5 kPa. The mean value of kinetic diameter is $d_{m,avg} = 437 \pm 26.2$ pm (6.18%), whose range is closely aligned with the predictions of [123] and [125].

4.5 Conclusions

This work proves that an optical technique such as molecular tagging is an efficient tool for providing measurements of diffusion coefficients. To the best of our knowledge, this work presented the first measurements of self-diffusion coefficients of gaseous acetone via this technique. A pressure range from 500 to 10000 Pa was investigated at room temperature. The diffusion coefficients obtained are in good agreement with data found in the literature, especially for pressures lower than 5 kPa. However, the measured diffusion coefficients do not follow the Chapman-Enskog equation and a different power law seemed to describe the relationship p-D_m. Consequently, we inferred an acetone kinetic diameter that unexpectedly decreases with pressure. These findings may also be a confirmation that the wide range of values registered in literature of diffusion measurements may be dependent on the choice of the measuring technique and the range of pressures investigated. At higher pressures (p > 5 kPa) our measured D_m were higher than the values inferred from the kinetic diameters found in the literature, which corresponds to a measured kinetic diameter as low as 300 pm (Figure 4.17 (b)). At higher pressure, the TTA phenomenon is stronger and the accurate extraction of the diffusion coefficient from the time evolution of the signal's variance via an optical technique may require a model that considers the most important intramolecular processes governing the triplet population. The optical signal acquired does not correspond strictly to the diffusion case of the Eistein-Brownian formula, especially in the time interval where the variance appears to evolve in a non-linear manner with time.

Chapter 5 Application of MTV technique to rarefied gas flow at slip regime

5.1 Experimental setup for MTV technique at low pressures

The molecular tagging velocimetry technique experimental setup is similar to the setup presented in the previous chapter. However, it needs to be adapted in order to use it for rarefied gas flows in rectangular channels. Apart from the requirements for the static chamber, the experimental setup must meet several additional requirements:

1) A channel with optical access replaces the visualization chamber;
2) Controlled thermodynamic conditions must be imposed at the entrance of the channel;
3) High flow rates are necessary in order to achieve a detectable displacement profile;
4) The fluctuation of the mass flow rate through the channel must be small enough for the corresponding acquisition time during one experiment.

In this work, the MTV measurement was verified via the constant volume technique. Eventually, the experimental setup could be suitable for both molecular tagging velocimetry and thermometry applications.

5.1.1 Gas circuit for MTV

The experimental setup is illustrated in Figure 5.1. In respect to the gas system used for the static gas chamber, two big gas tanks were added at the upstream (T1) and downstream (T2) of the channel. Each tank had a volume of around 90 L [35; 102]. In order to create a one-directional pressure-driven flow from T1 to T2 through the channel, the pressure at T1 is always higher than the pressure at T2. A tank containing carrier gas such as helium was used to create gas-vapor mixtures. The vacuum pump 1 served to evacuate the channel and T1. Vacuum pump 2 served to evacuate the gas mixing line (tracer reservoir and carrier gas tank) and T1.

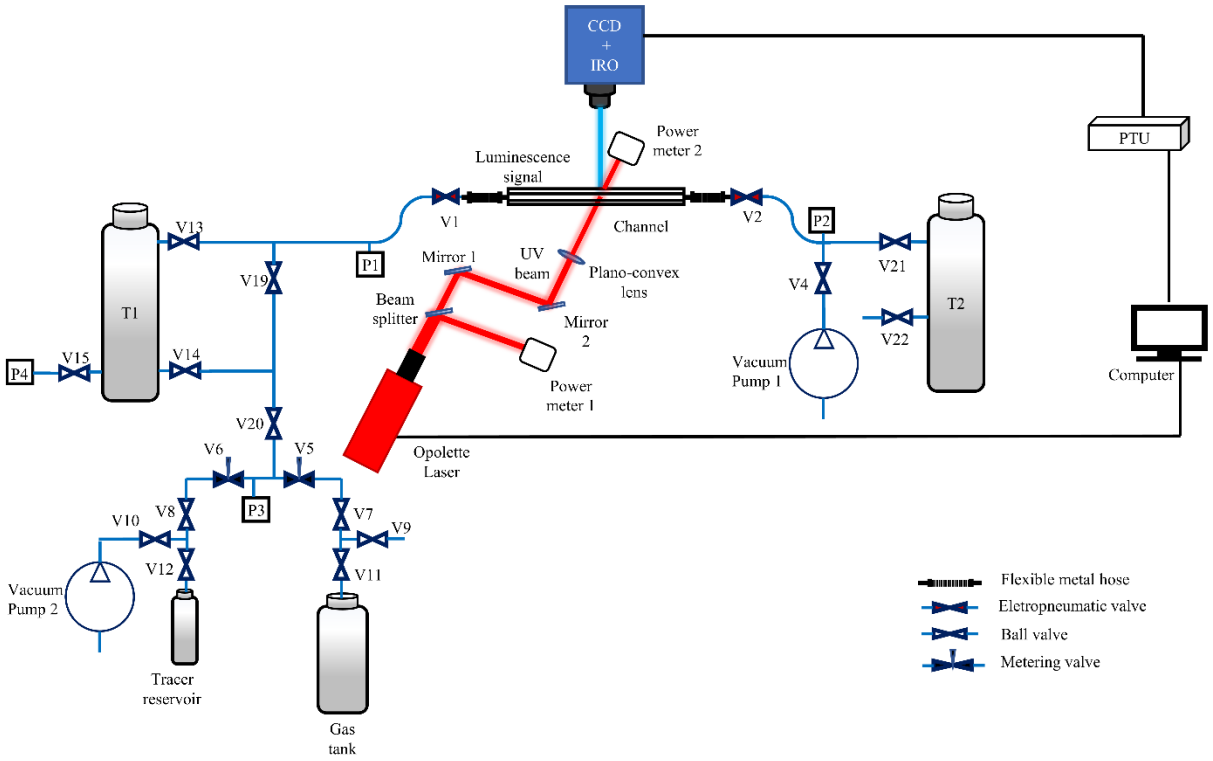

Figure 5.1. The sketch of gas system for implementation of MTV technique.

The pressure sensors located at different positions in this gas system were the same type described in Chapter 4. Here, pressure sensors P1 was employed for recording the static pressure at the inlet of the channel, while P2 was used to measure the static pressure at the outlet of the channel and at the downstream tank T2. Pressure sensor P3 monitored the outgassing of the acetone reservoir and the gas mixing line. Pressure sensor P4 measured the static pressure of the upstream reservoir T1. Through P1 and P4, it was verified that the pressure of T1 was always identical to the pressure at the inlet of the channel.

The gas mixture concentration was regulated through the pressure sensors. From an initial complete vacuum in the system, acetone vapor was introduced in Tank 1 to a desired partial pressure (which coincided with the total pressure in the tank). From here on, a carrier gas was introduced in Tank 1. By monitoring the total pressure, the concentration of each species could be deduced.

Three kinds of valves were used in the gas circuit i) Pfeiffer® DVC0 16PX electropneumatic valves (V1, V2) for controlling the flow in the channel, ii) HEF® dosing valves (V5, V6) for controlling the concentration of each species in the gas mixture, iii) Pfeiffer® ball valves for general purposes.

5.1.2 Channel

Velocimetry measurements were performed in a newly designed millimetric rectangular channel. The channel fulfilled the requirements as follows: i) good sealing properties in order to work at low pressures; ii) chemical resistance to acetone vapor; iii) optical access for tagging and acquisition; iv) controlled dimensions of the cross-section.

The main body of the channel consisted of three main parts, all of which were transparent materials. The laser entrance and exit were fabricated in Suprasil ®, the acquisition optical access was fabricated in borosilicate (Figure 5.2).

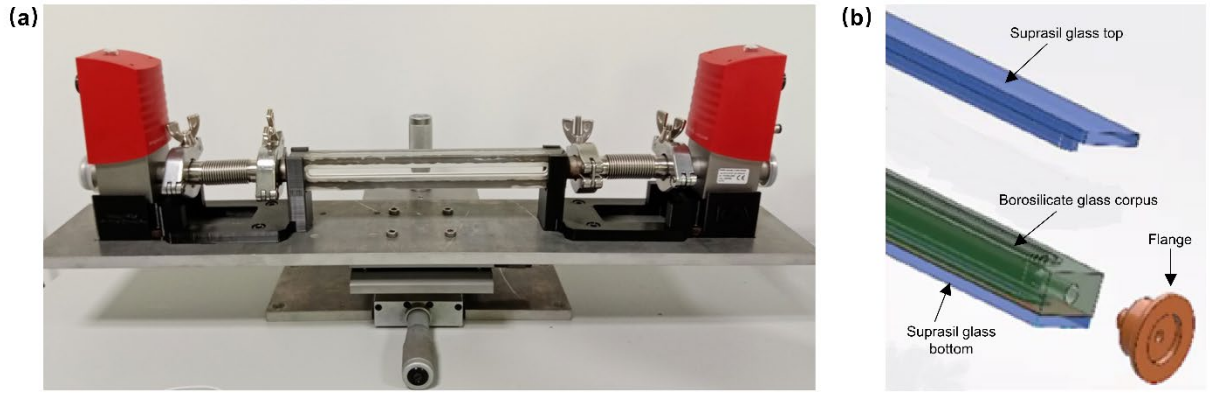

Figure 5.2. The transparent channel. (a) the photo of the channel with the flexible hoses, electropneumatic valve at the two side of the channel; (b) schematic of inside structure of the channel.

The connection between all the different parts was made by adhesive Araldite® 2014-2, which is resistant to most chemicals, such as acetone, water, high temperature and could also guarantee good sealing properties at low pressures. Furthermore, Araldite® 2014-2 produced very little out-gassing at low pressures. The curing of the adhesive was realized at room temperature. Unlike channels used in previous works [35; 102], this novel design ensured a constant cross-section along

the full length of the channel and a leakage-free environment. A further improvement consisted in having an optical access along the whole length of the channel, thus velocity profile measurements were possible at every cross-section. Laser reflections inside the channel were negligible since the whole channel was transparent.

The transparent channel was connected to the gas circuit through two flanges which were glued into the channel (Figure 5.3). In order to protect the connection between the flange and the borosilicate body, a pair of adjustable-length metal hoses were introduced between the flange and the electropneumatic valves V1 and V2. The valves served to regulate the inflow of gas in the channel. The electropneumatic valves could be remotely operated, this allowed less vibrations in the system at opening and closure. The channel and the valves were supported by a metallic platform.

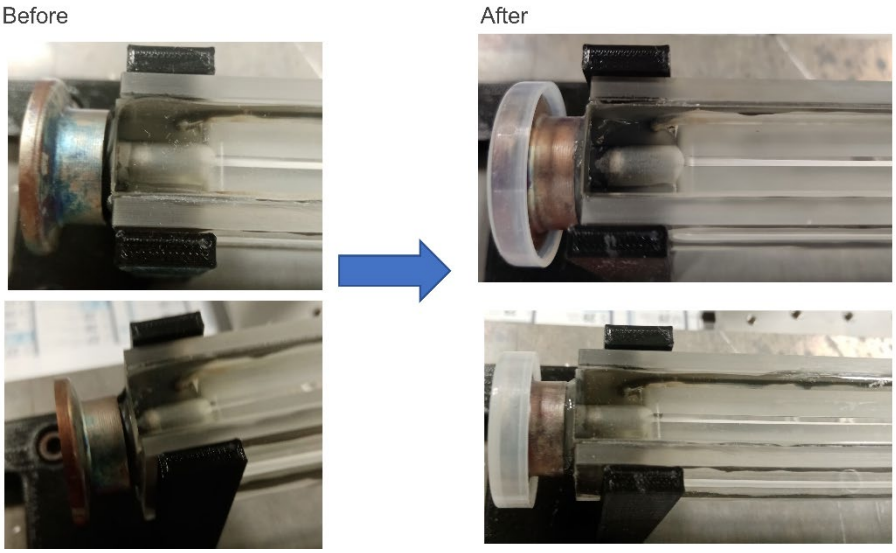

Figure 5.3. Adding adhesive to increase the sealing of the channel.

The sealing properties of the channel were checked with a Pfeiffer® ASM310 portable helium detector. Via this detector it was possible to detect leakage areas by locally spraying helium with a pistol. For a more local leak detection, alcohol drops were used on the external surface of the channel. Liquid drops appearing in the system after depositing a drop of alcohol was another sign

of local leakage. The use of high vacuum grease on the outer surface of the channel was avoided since the grease could be easily sucked into the inner sections of the channel at high vacuum. If necessary, adhesive was added to improve the sealing of the channel (Figure 5.3). The final leak rate value of the channel was measured to be around 1.2e-10 mbar l/s (indicated value read from the leak detector), and the pressure variation rate in the channel was 4.8 Pa/h.

5.1.3 Channel internal cross-section

The definition of the channel wall position was of vital importance for a correct and accurate measurement of slip velocity. The channel wall detection was particularly challenging since the channel was fully transparent. Different methods were employed:

i) The internal dimensions of the channel were measured via an X-ray tomography. For the cross-section size measurement, five images were acquired every 40 mm from the central position (Figure 5.4 (a)). Each image had a pixel size of 85.62µm x 85.62 µm (Figure 5.4 (a)), 7.71µm x 7.71 µm (Figure 5.4 (b)), and 7.97 µm x 7.97 µm (Figure 5.4 (c)), separately. The height (H) of the channel was measured in six different positions via imageJ on each image. Therefore 30 measurements were obtained at different positions of the axis of the channel (Table 5.1). The mean value of the height measurements resulted in H=1619 µm. The width of the channel was measured in the same manner resulting in b=7460 µm. The two white lines in Figure 5.4 (c) may indicate the air gap between the Suprasil glass top and bottom and the borosilicate glass corpus, which exists due to unavoidable gaps between the connection of different parts. The length of the channel is L= 20.9 cm. It was observed from the measurements that the channel height was smaller at its center, while larger at the two ends. This could be caused by uncertainties introduced by the focal point of the image which was positioned in the middle of the channel height and width.

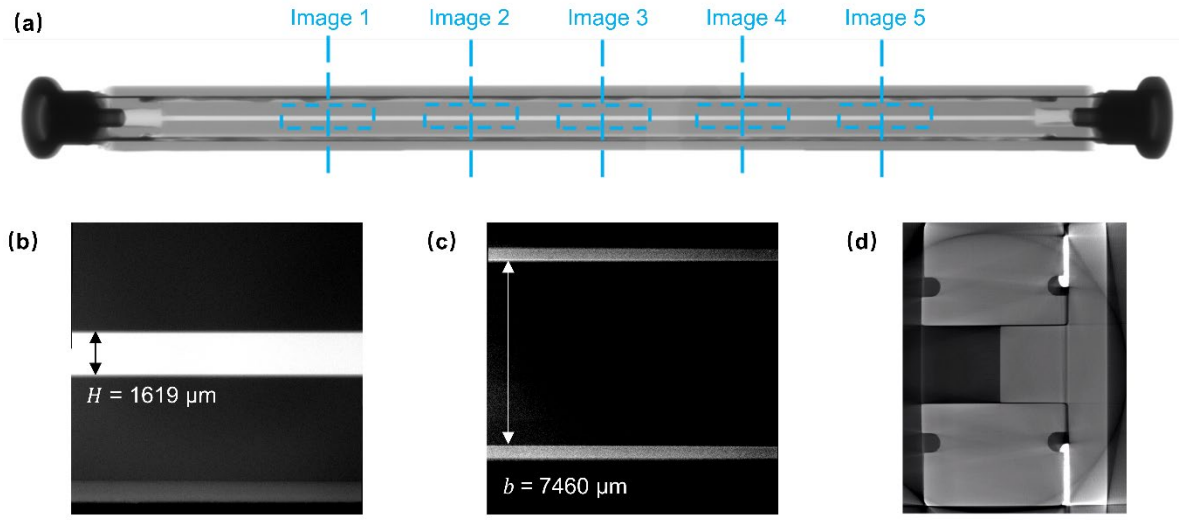

Figure 5.4. Tomography image of the channel. (a) The whole channel in the view of ICCD, each pixel represents 85.62 μm; (b) Measurement of the channel height, each pixel represents 7.71 μm; (c) Measurement of the channel width, each pixel represents 7.97 μm; (d) Cross-section of the channel.

Table 5.1. The 30 measurements of channel height via tomography

	Image 1 [μm]	Image 2 [μm]	Image 3 [μm]	Image 4 [μm]	Image 5 [μm]
1	1712	1588	1565	1557	1688
2	1704	1588	1550	1557	1688
3	1681	1604	1542	1550	1727
4	1673	1611	1573	1542	1712
5	1681	1627	1588	1534	1673
6	1665	1604	1565	1550	1673
Edge Method	1697	1629	1581	1559	1586

ii) Two edge detection algorithms (MATLAB®) were applied to the tomography images. The Canny algorithm uses the derivative of the Gaussian filter to compute the gradient of the channel wall image. The edges are detected by finding the local maximum value of the image gradient. This algorithm can find a strong and a weak edge by using two thresholds (Figure 5.5 (a)). The Roberts algorithm was tested, too, and it seemed to give the best results in terms of stability.

Roberts algorithm finds edges at those points where the gradient of the image intensity matrix is maximum (Figure 5.5 (b)). From here on, a linear fitting was implemented to detect the edges and thus, the corresponding height of the channel. The edge detection algorithm and post-processing method were implemented to all the tomography images (Figure 5.6). The mean value of channel height for each image is reported in Table 5.1. Since the tomography optics were focused in the center of the channel, the central image was considered the one with less uncertainty (Image 3, H = 1581 µm). Furthermore, it is possible to observe from the bottom images of Figure 5.7 that the inside of the channel may not be perfectly straight along the axis of the channel.

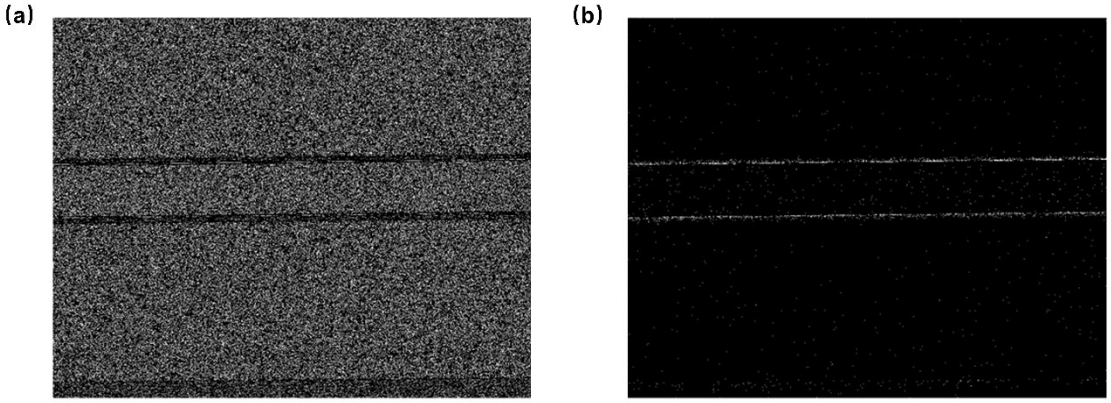

Figure 5.5. Edge detection method choice. Edge detection results by using Canny method (a) and Roberts method (b).

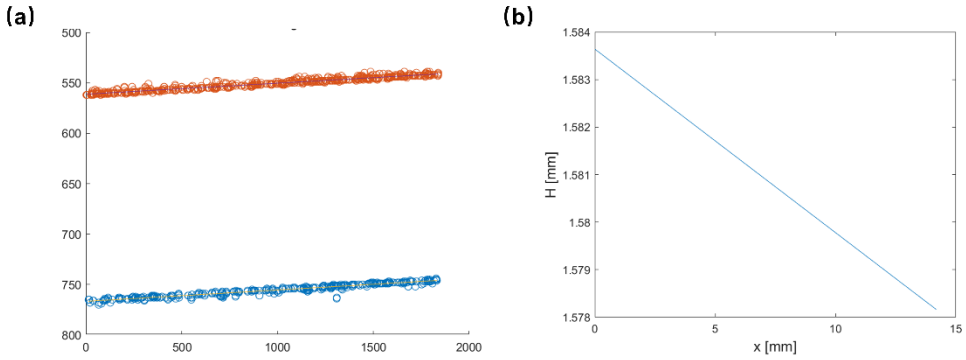

Figure 5.6. Channel wall boundary extraction from Robert method. (a) Linear fitting (black solid line) to the two channel wall boundaries (open circles); (b) Channel height measurement results.

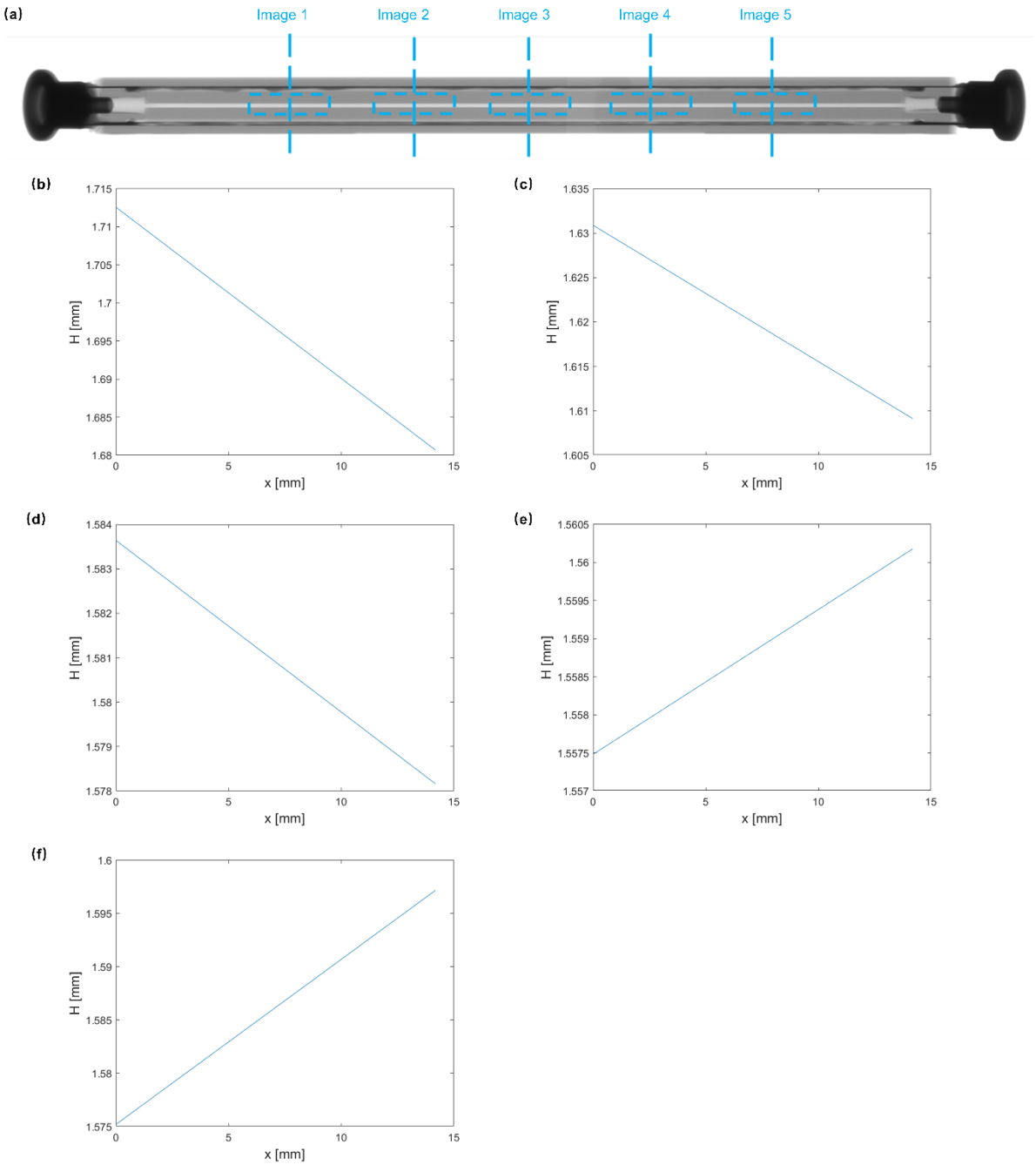

Figure 5.7. Edge detection algorithm on tomography images at different position along the channel. (a) The schematic of test section on different positions along the channel axis;(b), (c), (d), (e), (f) Channel height results along its test section corresponding to image 1,2,3,4,5 separately in (a).

iii) Measurements were obtained via a method based on a cold light source and image acquisition through the same lenses used for MTV. As shown in Figure 5.8 (a), the cold light source was put in front of the transparent channel, the angle of the lamp was precisely adjusted and tested until the edge of the channel could be identified (Figure 5.8 (b)).

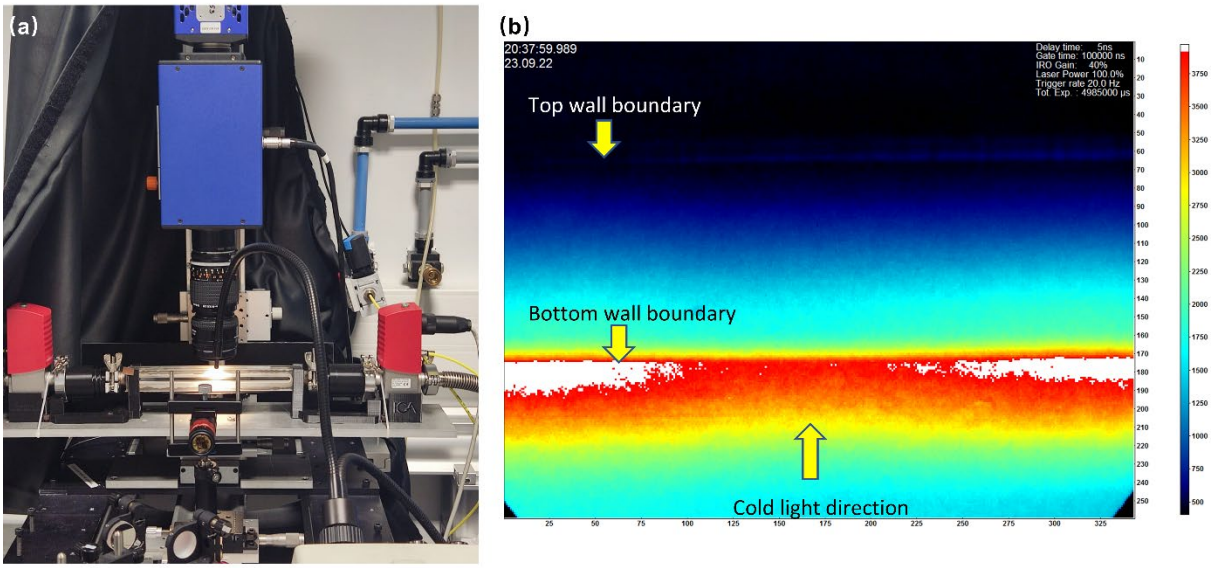

Figure 5.8. Experimental method for definition of channel wall position with cold light source. (a) Experimental setup; (b) Typical image of wall boundary took with cold light source, acquisition parameters: Δt = 5 ns, Δt_{gate} = 100000 ns, N_l = 100, N_i = 10, and G = 40% with a 4 × 4 binning.

The 3D-mapping of the raw images showed that the position of the channel walls corresponded to the position of two peaks (Figure 5.8 (b) and Figure 5.9 (b)). After processing the images through the Canny method, the wall positions were easily identifiable (Figure 5.9 (d)). The corresponding estimated channel height was H =1626 µm. The spatial resolution of the measurements was linked to the pixel dimension of 15.2 µm. Furthermore, this method improved the adjustments to be made in respect to the orientation of the channel in respect to the acquisition optical path. Since the channel wall, obtained by the edge detection, does not have any visible angle, it was possible to deduce that the channel is perpendicular and centred in respect to the

optical path of the IRO lenses. The edge detection algorithm and cold light source can also help to identify where the channel wall is.

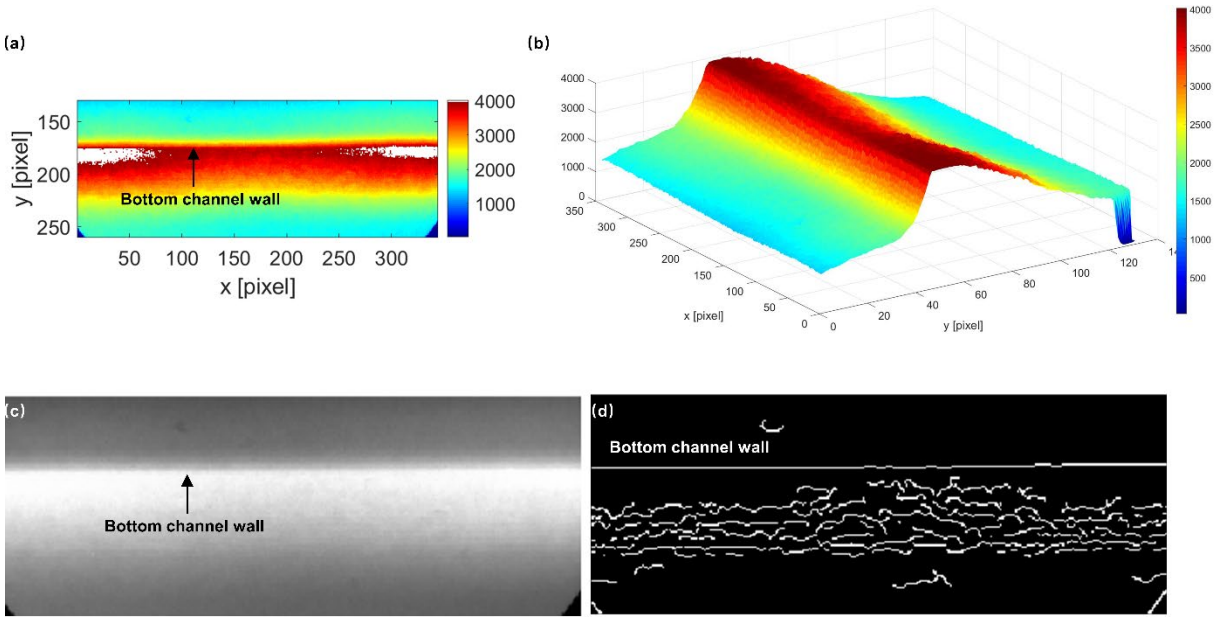

Figure 5.9 Edge detection implemented to the bottom image acquired by cold light source. (a) Upper half of the raw image; (b) 3D-mapping of the intensity image from (a); (c) The gray-scale image of (a); (d) the gray scale image after edge detection algorithm to tell where the channel wall is.

Although the novel channel had many advantages, the transparent design also brought some limitations. One big drawback was related to the correct channel wall detection during the velocity fields measurements. This issue was greatly improved by positioning a black paper cover along the whole thickness of the channel walls (Figure 5.10). The main target of the cover is to avoid light noise from the surrounding area, like reflection or refraction from other elements. On the top, front and back surfaces, black paper was cut to the size of the optical access. The bottom piece of the window was just a pure black paper.

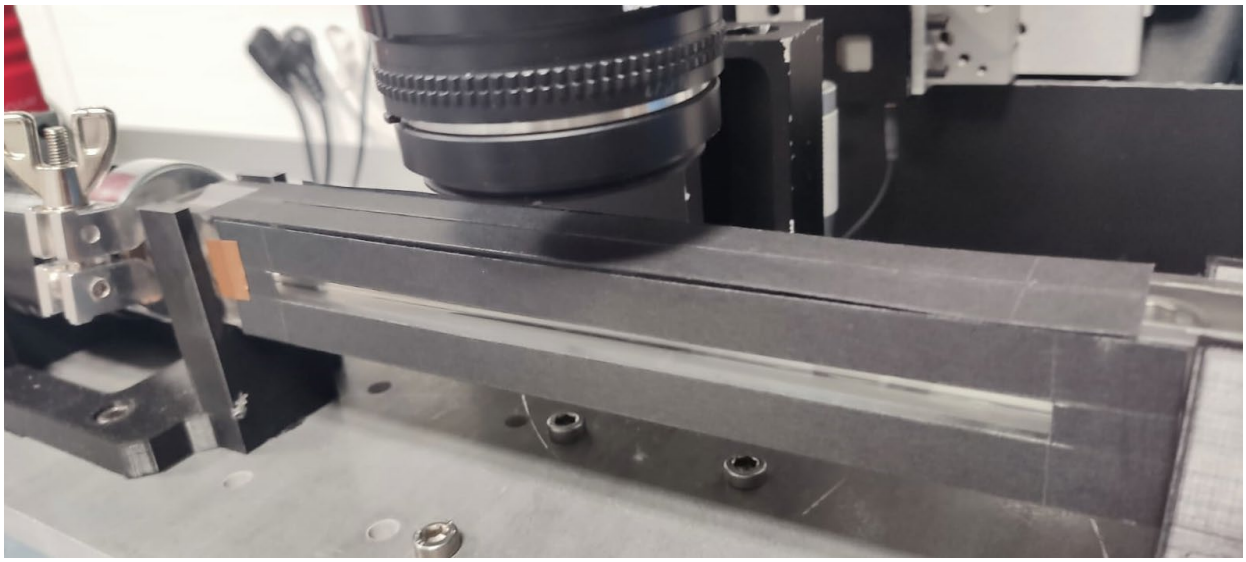

Figure 5.10. Light-absorbing window fabricated in black paper.

5.1.4 Optical path

Some new elements were introduced in the optical path in respect to those already discussed in the previous chapter. A flat 50: 50 TECHSPEC® UV Plate laser beam splitter was implemented before the reflection mirrors in order to measure the energy of the laser during the MTV experiments (Figure 5.1 and 5.11). The beam splitter allows optimal performance ranging from 250 - 450 nm.

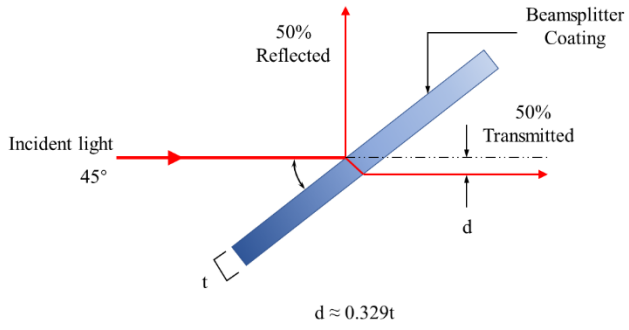

Figure 5.11. Schematic of the function of plat beam splitter.

Additionally, a Thorlabs ® BE02-UVB beam expander was used before the plano-convex lens in order to improve the laser beam focusing (Figure 5.12). The AR-coating on the lens allows

working with wavelength from 240 to 360 nm. The sliding lens on it can help to adjust the collimation of the laser beam. The beam expander has a fixed double laser beam magnification. When the diameter of the incident light passing through the plano-convex is two-times larger, the outgoing light beam is two times thinner. The beam expander can help increase the laser beam focusing power.

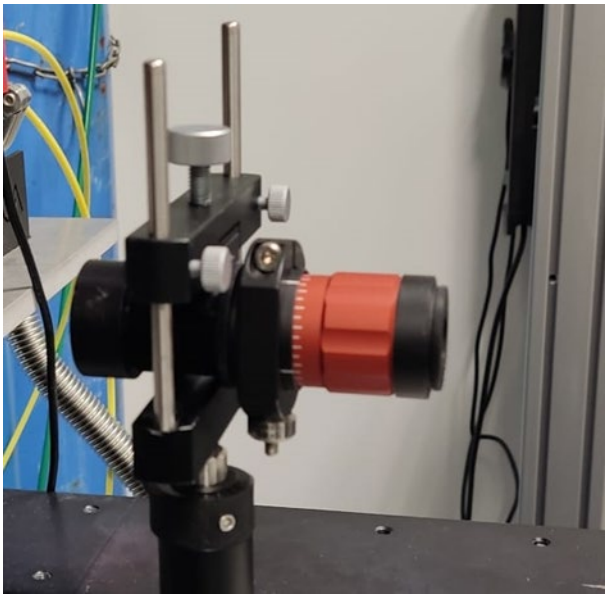

Figure 5.12. Beam expander.

5.2 Experimental methodology

5.2.1 T1-Channel-T2 and T1+T2-Channel experimental strategy

Since the goal of this work was to study rarefied gas flows, sub atmospheric pressures needed to be imposed between inlet and outlet of the channel. This might be of somehow difficult achievement if the experimental conditions need to be stationary.

Method A: Tanks T1 and T2 are positioned at both ends of the channel (Figure 5.1). During one experiment the T1-channel-T2 configuration works as a closed system. The methodology here employed in order to engender a Poiseuille flow in the channel coincides with the constant volume methodology [145]. The pressure in T1 is always larger than T2, that is $p_1(t) > p_2(t)$. Once an

initial pressure difference has been imposed between the two tanks, the thermodynamic system relaxes to a final equilibrium state where $\Delta p = p_1 - p_2 = 0$. The pressure p_1 is decreasing from its maximum to its minimum and p_2 is increasing from its minimum to its maximum. A typical example of pressure variation with time at the two ends of the channel is shown in Figure 5.13. The temporal variation of pressure is dependent on the initial pressure difference $\Delta p(t_0)$ and the volume ratio between T1 and T2. When the value of $\Delta p(t_0)$ and tank volume ratio V1/V2 is known, the pressure variation can be calculated if the conductance of the channel is known [145]. In our experiments, the two tanks have equal volumes (V1/V2 ≈ 1), thus during the totality of one experiment the mean pressure $p_m(t) = \frac{1}{2}(p_1 + p_2)$ remains constant (Figure 5.13 (b)). Furthermore, the pressure difference variation with time can be expressed as

$$\Delta p(t) = \Delta p(t_0) \exp\left(-\frac{t}{\tau_f}\right), \tau_f = \frac{V_0}{C}, V_0 = \frac{V_1 V_2}{V_1 + V_2} \tag{5.1}$$

where τ_f is the characteristic time of the flow and C is the conductance which depends on the channel geometry and mean rarefaction [6]. Our experiments verified the exponential decay of the pressure difference variation with time (Figure 5.13(b)), thus the value of τ_f could be obtained by fitting the exponential function to the experimental data. Since the volume of the tanks is known the conductance of the channel can be inferred.

Method B: a Poiseuille flow can be generated along the channel also in a slightly different manner. In the T1+T2-channel case scenario, the two tanks are positioned at the inlet of the channel and a vacuum pump is used to create a Poiseuille flow (open system). This strategy allows to create a great gas mass inertia at the inlet of the channel (180 liters), thus when pumping through the channel, pressure is considerably stable in the upstream volume during one experiment [35; 102]. Through this strategy it is possible to obtain quasi-stationary flow conditions in the system (Figure 5.14).

The current molecular tagging velocimetry experiment allows measurements for flows in stationary conditions. Thus, if the limit conditions of the flow evolve with time this might not be the case. In order to be able to acquire stationary flow conditions, the image acquisition has to be sufficiently short (low number of laser shots N_l).

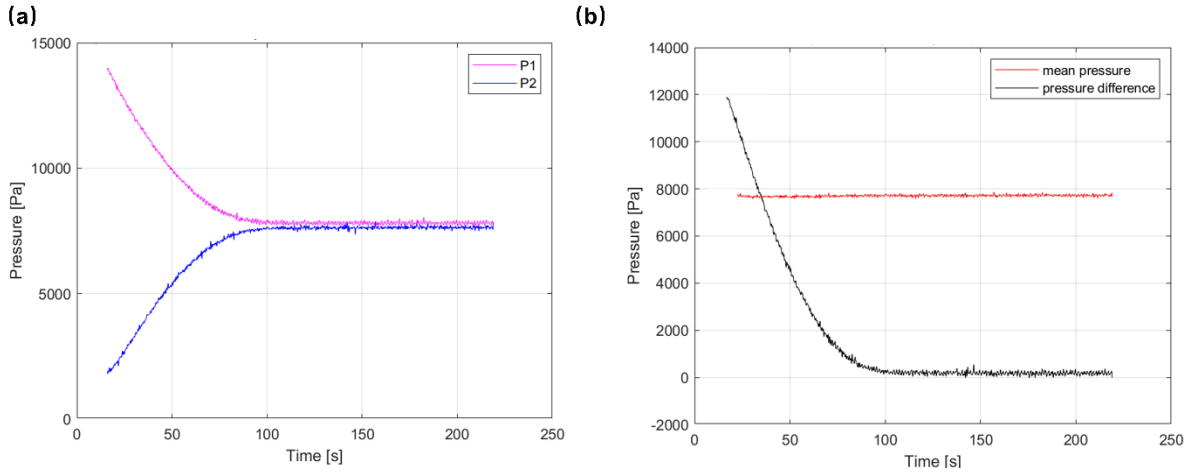

Figure 5.13. A typical example of pressure variation over time of T1-Channel-T2 method, when the initial pressure $p_{1,0}$ = 15 kPa, $p_{2,0}$= 1.4 kPa, pure acetone vapor flow. (a) Temporal evolution of p_1 and p_2; (b) Temporal evolution of pressure difference and mean pressure.

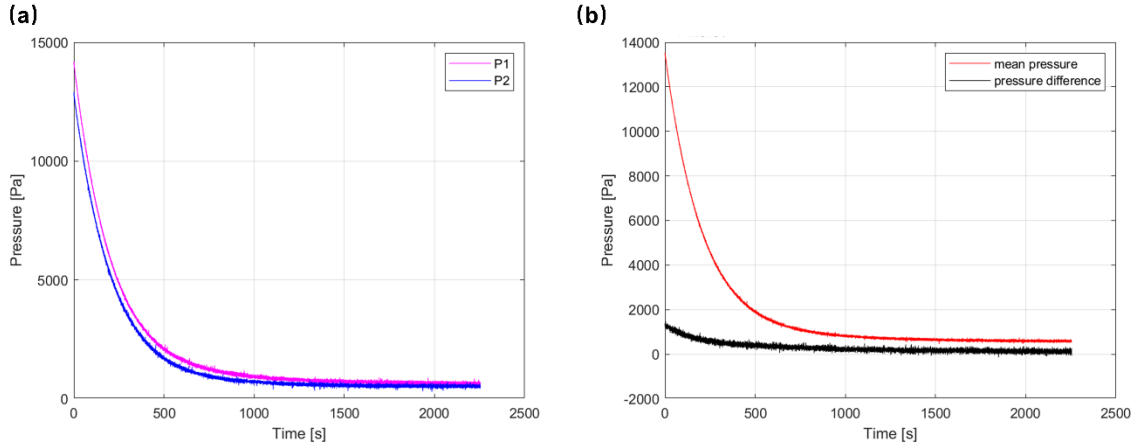

Figure 5.14. A typical example of pressure variation over time of T1+T2 Channel method, when the initial pressure $p_{1,0}$ = 15 kPa, $p_{2,0}$= 0, p_2 will jump to a high pressure when flow begins, pure acetone vapor flow. (a) Temporal evolution of p_1 and p_2; (b) Temporal evolution of pressure difference and mean pressure.

5.2.2 Dynamic constant volume technique

The present experimental configuration allows us to apply the constant volume technique [145] to measure the mass flow rate along the channel at every instant of one experiment. If the pressure difference imposed along the channel varies with time also the flow velocity and mass flow rate follow the same trend. From the mass flow rate measurements obtained via the constant volume technique, it is possible to extract the mean velocity of the flow for a given cross-section. This can cross-validate the velocity measurement results acquired via MTV technique. As reported in the literature [145] the mass flow rate can be obtained from our experiments as:

$$\dot{m}_{CV}(t) = -\frac{V_0}{R_s T}\frac{d\big(\Delta p(t)\big)}{dt}. \tag{5.2}$$

Thus, the mean velocity of the flow in a single cross section can be expressed as

$$\bar{u}_{CV,2D}(x,t) = \frac{\dot{m}_{CV}(t) R_S T}{Hbp(x,t)}, \tag{5.3}$$

where $\bar{u}_{CV,2D}(x,t)$ corresponds to a fully developed mean velocity of a two-dimensional Poiseuille flow and $p(x,t)$ represents pressure distribution along x-axis (centreline of the channel).

However, as explained in [6], the measured MTV value of the average velocity in the channel corresponded to the average of the velocity profile in the plane where the camera was focused, that is the centre of the channel, z = 0, x = L/2). The relation between these two velocities can be approximated as [102]:

$$\bar{u}_{CV,2D}(t) = 1.14\bar{u}_{2D}\left(x = \frac{L}{2}, t\right) = 1.14\ \bar{u}_{CV}, \tag{5.4}$$

where $\bar{u}_{2D}$ is the two-dimensional velocity distribution on a cross-section, $\bar{u}_{CV}$ is the mean velocity of the velocity profile in the centre plane where MTV were measured.

5.3 Experimental results for MTV

Velocity fields of pure acetone vapor flows were measured in hydrodynamic regime. The hereafter presented measurements were obtained with the T1-channel-T2 configuration. The initial pressure differences imposed between inlet and outlet of the channel were $p_{1,0}$ = 2kPa, $p_{2,0}$ = 1 kPa. The pressure variation with time during one experiment is represented in Figure 5.17 (a). The laser shots frequency was 20 Hz and the number of laser shots per image was set to N_l = 100. Thus,

the acquisition of one image needed around 5s. The gain was set at its maximum (G = 100%) and Δt_{gate} was set at 500 ns. The spatial resolution of the acquisition corresponded to a 4 × 4 pixels binning. Measurements were realized for four different delay times t = 20 µs, 30 µs, 40 µs, 50 µs. N_i = 10 images were averaged for each measurement. Since the flow is quasi stationary (Fig. 5.13), in order to have the same thermodynamic limit conditions on the channel, the experimental run needed to be repeated N_i times. The image acquisition strategy was thus a vertical averaging method as shown in Figure 5.15 [102]. The procedure had to be repeated for each delay time investigated, therefore 40 experimental runs were realized by imposing the same thermodynamic initial conditions at the two ends of the channel. A totality of 800 raw images were treated for the whole experimental campaign.

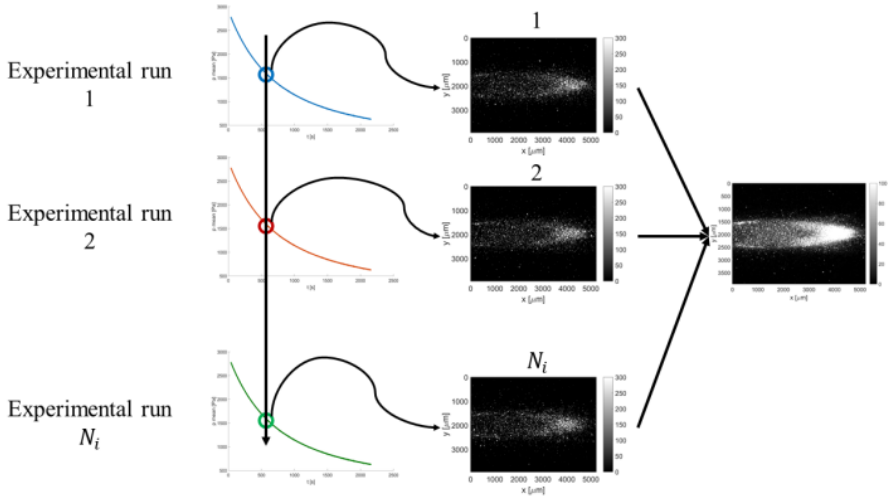

Figure 5.15. The schematic of 'vertical' image averaging strategy. Figure from Fratantonio [102].

As shown in Figure 5.16 (a), during the acquisition of one image (5s) the pressure difference between inlet and outlet of the channel decreased, while the mean pressure was stable. Thus, even if some systematic uncertainty was introduced in the velocity profile measurements, they could be quantified. The maximum pressure difference deviation during one image acquisition from its initial starting point is around 40 Pa. Considering that the accuracy of the pressure sensor is around

±20 Pa for the current pressure reading range, this pressure difference variation during one image seems acceptable.

The post-processing procedure detailed in Chapter 4 was implemented to the acquired images for velocity profile extraction. The channel wall position was measured as established in section 5.1.3. One single image of the displacement profile is shown in Figure 5.16 (b). Averaging along 10 images increases the overall quality of the image.

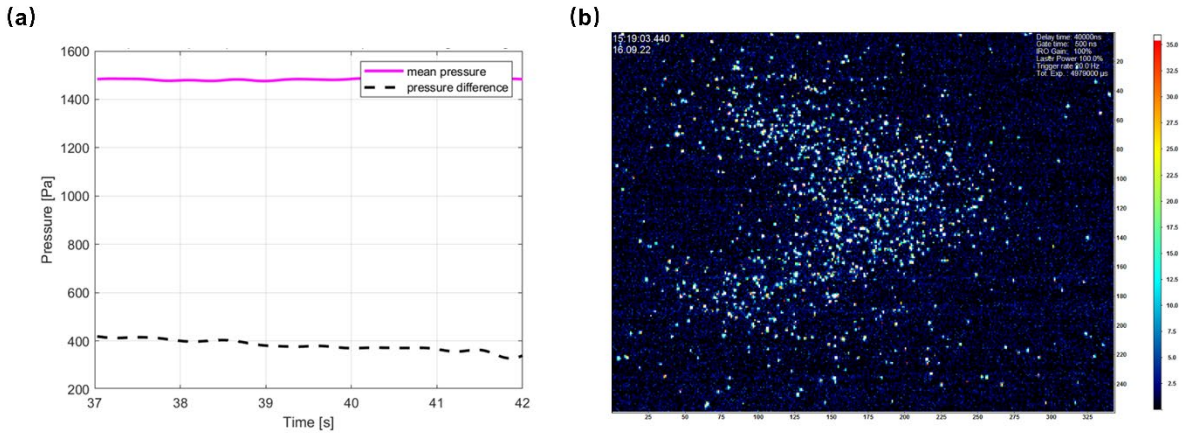

Figure 5.16. One raw image acquisition of pure acetone flow with p_m = 1481 Pa, Δp = 381 Pa, t = 30 µs, Δt_{gate} = 500 ns, N_l = 100, N_i = 1, and G = 100% with a 4 × 4 binning. (a) Temporal evolution of mean pressure and pressure difference during one raw image acquisition duration; (b) One raw image of displacement profile.

The displacement profile corresponding to each delay time was extracted (Fig 5.17). As indicated in chapter 4, a gaussian function was used to fit the photoluminescent signal at each horizontal line (y = constant). The peak of the gaussian fitting was used to follow the tracer displacement for velocimetry applications. Figure 5.17 shows the final averaged image and gaussian peaks of each horizontal lines at different delay times. It is possible to observe in these images how some photoluminescence is emitted also from the wall. Thus, the information used in order to apply the reconstruction method [35-37] was restrained to the channel inner dimensions.

The mean velocity of the flow measured via MTV was compared to the dynamic constant volume technique (DCVT) measurements. The peculiarity of this experimental method is that both measurements are realized exactly at the same time. Table 5.2. resumes the values obtained via

MTV and DCVT. One can see that there is a good agreement between both measurements. Nevertheless, there is still a relatively high uncertainty associated to the MTV method, especially in respect to obtaining slightly different values of mean pressure at different delay times.

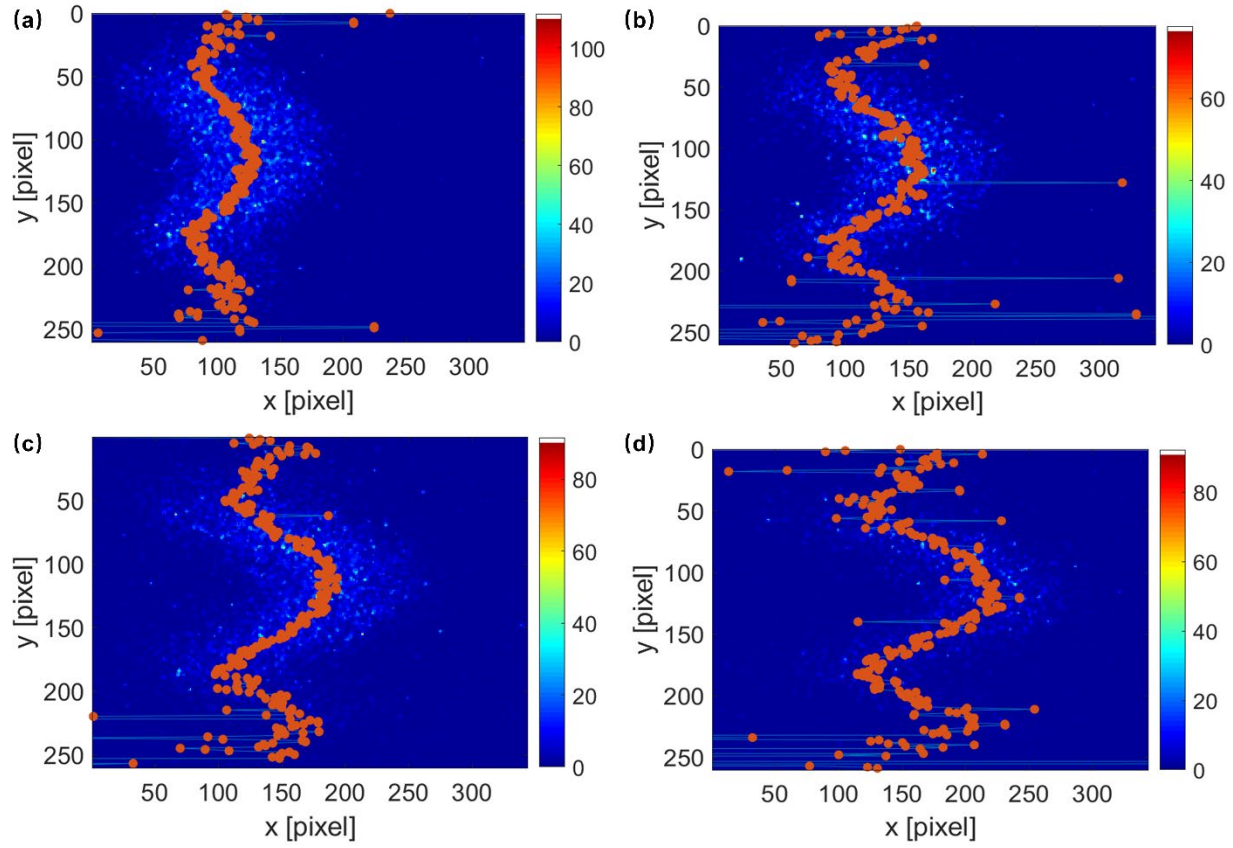

Figure 5.17. MTV acquisitions of pure acetone vapor flow with displacement profile with p_m = 1481 Pa, Δp = 381.0 Pa, Kn=0.00075, Δt_{gate} = 500 ns, N_l = 100, N_i = 1, and G = 100% with a 4 × 4 binning. (a) t = 20 µs, (a) t = 30 µs, (a) t = 40 µs, (a) t = 50 µs,

Table 5.2. Comparison of mean velocity between MTV and CV technique

$\overline{u_{MTV}}$ （m/s）					
Pressure difference (Pa)	381.0	284.6	235.4	194.7	161.0
20 μs	30.63	28.31	21.77	23.41	29.86
30 μs	34.18	27.85	24.01	17.93	17.38
40 μs	34.29	29.68	23.07	20.35	16.24
50 μs	36.10	31.65	24.62	21.92	17.56
$\overline{u_{CV}}$	37.48	31.00	25.64	21.21	17.54

5.4 Conclusions

In this chapter, we described the experimental setup and experimental method used for applying the MTV technique to rarefied gas flows. Specifically, a great effort has been done in respect to designing and fabricating a new transparent channel. The advantages and disadvantages of this new device were analysed, such as the difficulty of correctly detecting the inner wall of the channel. An original method based on edge detection algorithm was proposed to better identify the wall position. The experimental setup was adapted for realizing measurements via the dynamic constant volume technique in parallel of MTV. This possibility was interesting enough since it offered and excellent tool for indirectly verifying the molecular tagging measurements. This was a preliminary study, since implementing the new transparent channel was a real challenge. Thus, on this basis, future work will be focused on obtaining better experimental results of velocity fields for rarefied gas mixture flows with the same channel.

Chapter 6 Conclusions and perspectives

The work in this thesis was mainly focused on obtaining a more accurate and precision-controlled MTV measurement of rarefied gas flow in a rectangular channel when implementing the reconstruction method.

It has been verified in previous works that the combined effect of molecular diffusion and advection prevents the extraction of local velocity profiles by simply dividing the molecular displacement by the time of flight [81]. A reconstruction algorithm was proposed by Frezzotti *et al.* [36] to obtain a correct extraction of the velocity profile, nevertheless the reconstruction method is extremely dependent on the diffusion coefficient [36]. At relatively high pressures, the reconstruction method gives satisfactory results [35; 37], however, at low pressures, the reconstruction algorithm has failed to accurately provide velocity profiles matching theory [35]. A possible source of uncertainty comes from the method's strong sensitivity to the diffusion coefficient value, thus this parameter needs to be well-characterized.

Nevertheless, the diffusion coefficient in confined flows is of difficult estimation and new experimental methods are needed in order to measure this parameter. At the moment, the diffusion coefficient calculation is based on a correct knowledge of the kinetic diameter of the molecular species, however, little information is available for what concerns complex tracer molecules such as acetone. In the experimental work presented in Chapter 4, measurements of the molecular diffusion coefficient and of the molecular kinetic diameter of gaseous acetone were obtained through molecular tagging, which is an optical technique. To the best of our knowledge, this work presented the first measurements of self-diffusion coefficients of gaseous acetone via an optical technique. The measurements consisted in following the displacement of phosphorescent molecules from an initially tagged center line. The distribution of the emitted signal was quantified through gaussian fitting functions at different moments of the experiment. The diffusion coefficient extraction was realized through the Einstein-Brownian diffusion equation which relates the gaussian variance evolution with time to molecular diffusion. From the diffusion coefficient measurements, an indirect experimental estimation of the kinetic diameter of gaseous acetone was obtained, too. The pressure dependency of diffusion coefficient was verified based on the pressure

range from 500 to 10000 Pa at room temperature. Even if the experimental results are in the range of data available in the literature, these values have still to be tested in a real case scenario of reconstruction method for MTV applications. A rigorous sensitivity analysis was conducted based on R-squared and SNR was proposed and utilized both considering the goodness of the curve fitting and image quality. A rigorous procedure was discussed to define the time range of interest based on theory and signal quality.

A detailed analysis was realized over the curious behavior of the variance evolution with time after initial tagging, which was expected initially to be linear with time during the full duration of one experiment. The non-linear behavior of the variance evolution over time at early time and high pressure was explained local luminescence quenching coming from triplet triple annihilation. A second explanation was related to local heating after laser excitation. This effect was especially evident at high pressures. This effect can affect greatly the behavior of the variance variation with time and it is thus to be avoided when extracting diffusion coefficients through the classic Einstein-Brownian equation, since results do not follow the theoretical predictions of the Chapman-Enskog equation. The experimental results also indicate a possible pressure dependency of acetone kinetic diameter, this could be an explanation over the high range of values that are found in the literature.

However, further investigation is required to understand if the evolution of the kinetic diameter with pressure is either a real physical phenomenon or just an error bias caused by higher inaccuracies for the higher-pressure data and/or uncertainties on the experimental conditions inside the test section. Investigations will be carried in order to consider TTA and local heating when modeling the signal distribution evolution in space due to diffusion. A new experimental campaign will be realized for acetone and diacetyl at large pressure ranges, especially in the 100 Pa to 1000 Pa, were the non-linear behavior of variance with time can be considered negligible. Diffusion measurements for different gas temperatures in respect to ambient temperature will also be obtained.

As described in Chapter 5, a new transparent rectangular channel was designed and fabricated to improve the extent of the possible test sections to be monitored. With the current design it was potentially possible to investigate the flow along the full length of the channel. In respect to previous designs, the sealing properties of the channel were improved. The inner cross-section of the channel was measured via X-ray tomography. Furthermore, an edge detection method was used to measure the channel height at different positions. However, the channel height was not

constant along its full length. This may be caused by the uneven application of adhesive between different parts of the channel. One of the main limitations coming with the transparent channel was the interference from surrounding light. An outer black mask was a good solution to avoid this problem. The task of defining the position of the wall of the channel during experiments is of a certain difficulty, too. A new experimental method with cold light source and edge detection method was used to identify their position.

Due to the quasi-stationary nature of the experimental methodology used for creating a Poiseuille flow at low pressures along the channel, a 'vertical' image averaging acquisition method was tested for the first time. This method was successfully applied in a non-rarefied pure acetone flow. A dynamic constant volume technique measurement was operated at the same time. A good agreement was obtained between the different experimental methods. This possibility was interesting enough since it offered and excellent tool for indirectly verifying the molecular tagging measurements. The preliminary efforts realized in respect of using Molecular Tagging have been at the moment of great help in the perspective of future works. However, implementing the new transparent channel was a real challenge. Thus, on this basis, future work will be focused on obtaining better experimental results of velocity fields for rarefied gas mixture flows with the same channel.

Future work will also focus on using MT for gas mixture purposes, since through the technique it is also possible to measure molecular concentrations along the channel. There is a huge difference between the molar mass of tracer vapor acetone and carrier gas helium. Although the mole fraction of tracer and gas is constant in the upstream and downstream reservoir (T1, T2) in our experimental strategy, when the rarefied gas mixture flowing through the channel, lighter gas molecule diffuse faster, which cause the separation of the two species. The diffusion flux can be caused not only by a mole fraction gradient, but also by pressure and temperature gradients causing two species to have different mean velocities even if the chemical composition of the mixture is uniform. This velocity difference leads to a separation of species, which is very important to understand in practice. The core question is that whether this velocity difference can be measured by us. In our MTV works, we can measure the velocity profile of the tracer, and the acetone concentration in the gas mixture. Both the numerical and experimental work are necessary to understand the species separation phenomenon.

Another perspective for the future work will be applying MTV to rarefied gas flows in more complex situations, such as channels containing obstacles inside the rectangular channel or periodic flows. The flow behavior should be predicted by CFD tools-FVM or DSMC. The shape of obstacle can be rectangular (cube, cuboid), triangular (pyramid), etc. [146]. The geometry of the channel with obstacle can be first by 2-D then improved to 3-D. The flow regime can start with continuum regime then improve to rarefied regime. To conclude, several options and perspectives are possible, being the most interesting one the use of molecular tagging in micrometric confined gas flows, which is still a cumbersome task to realize.

Appendix A

Outgassing experimental procedures

In order to provide an oxygen-free environment, the following procedure is mandatorily (Figure 4.9):

1) all the valves keep closed at the beginning;
2) vacuum pump 1 and 2 keeps working;
3) open valve V3, V2 and create vacuum inside the chamber;
4) open the valve V8, V7, V5, V14, V4, and fully open valve V6 until the gas line is full of the acetone vapours and air hided inside each element;
5) once the numerical values read from P3 do not change any more, which means the pressure inside the gas line is quite stable, close the valve V8 and open valve V14 to create vacuum inside the gas line again;
6) the step 4 and 5 repeated several times to reach fully outgassing.

Appendix B

Measured laser energy and Absorption cross sections

A low laser energy value is preferred in order to protect the optical access of gas chamber and avoid TTA process or local temperature rise. A high stability of laser energy is also in need. It is necessary to precisely control and monitor the laser energy during image acquisition process.

As measurement strategy described in Section 4.2.2, the measured results obtained by laser energy detector 2 in the back of the gas chamber during the image acquisition $E_{2,img}$ ($t = 20\mu s \sim 100\mu s$). The evolution of the three measured variables with pressures are summarized in Figure B.1. From this figure, $E_{1,init}$ can be taken as a constant among all the experiments, which is obtained before the OPOlette laser and image acquisition. The mean value of $E_{1,init}$ among all the pressure range is 33.1 μJ, whose standard deviation is 0.9129 μJ, exactly within the uncertainty range. Thus, the induced laser energy at different pressure can be considered as a constant.

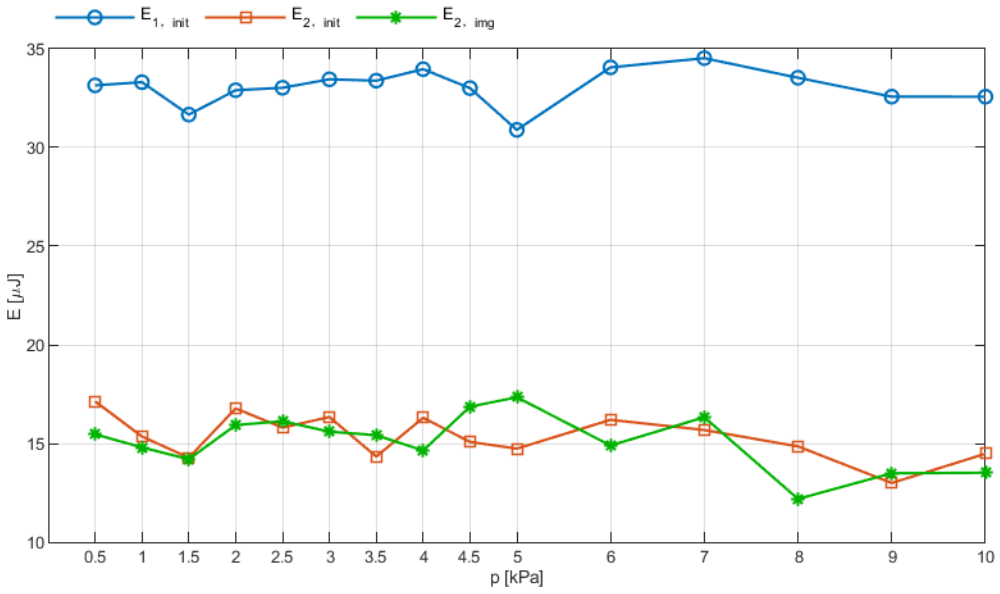

Figure B.1. Three measured averaged laser energy parameters evolve with pressure.

While the laser energy measured in the back of the chamber, both $E_{2,init}$ and $E_{2,img}$ before and during the image acquisition when the gas chamber was filled with acetone vapor at different pressure, show a tendency to decrease linearly with increasing pressure. Since $E_{1,init}$ can be regarded as a constant, the ratio between $E_{2,init}$ and $E_{1,init}$ and the ratio between $E_{2,img}$ and $E_{1,init}$

can also show a linear decrease tendency. A linear fitting is also performed on $E_{2,init}/E_{1,init}$ and $E_{2,img}/E_{1,init}$. The results of the ratios are illustrated in Figure B.2. The difference between $E_{2,init}$ and $E_{2,img}$ is due to the fact that the OPOlette laser shows a decreasing trend under long continuous emission. For $E_{2,img}$,the recording duration which is the image acquisition time is around 23 minutes (1350 s) in total. The recording duration for $E_{2,init}$ and $E_{1,init}$ is both only 5 min, in order to obtain the exact ratio of the laser energy ratio between the incoming laser and the outgoing laser of the gas chamber. This explain the reason why $E_{2,init}$ is larger than $E_{2,img}$.

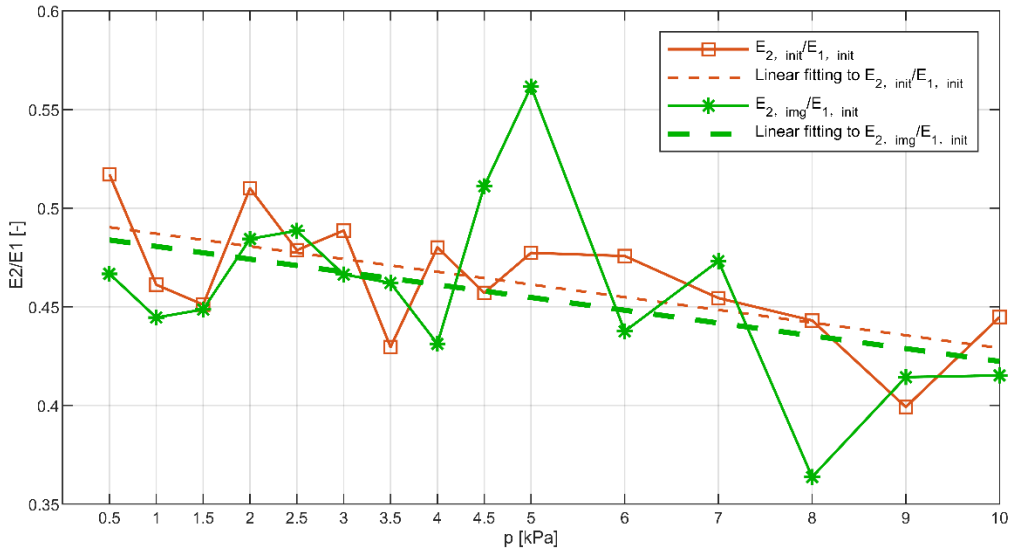

Figure B.2 Linear fitting to $E_{2,init}/E_{1,init}$ and $E_{2,img}/E_{1,init}$.

This linear decrease can be explained by the Beer-Lambert law, the relationship between the laser energy measured in the back of the gas container E_2 and laser energy measured before the gas container E_1 can be described as

$$\frac{E_2}{E_1} = e^{-\sigma_{abs} l n}, \tag{B.1}$$

where σ_{abs} is the absorption cross-section of the absorbing species, l is the optical length of the medium, $n = \frac{p}{k_B T}$ is the number density.

We assume that, in our case, during the laser excitation and light emission, the incident laser energy E_1, pressure p, and bulk temperature T can be considered as constant.

In that case, we can derive the following equation

$$\frac{E_2\ (p = 500Pa)}{E_1} = e^{-\sigma_{abs} l n_0},$$

$$\frac{E_2\ (p = 10000Pa)}{E_1} = e^{-\sigma_{abs} l 20 n_0},$$

$$\frac{E_2(p = 10000Pa)}{E_2(p = 500Pa)} = \frac{e^{-\sigma_{abs} l 20 n_0}}{e^{-\sigma_{abs} l n_0}} = e^{-\sigma_{abs} 19 l n_0}, \quad (B.2)$$

where n_0 represents the number density at p = 500 Pa. Based on the design blueprint of the gas chamber, the distance between the two Suprasil windows is 0.04568 m. The results of E_2 are acquired from the linear fitting of $E_{2,init}$ (Figure B.2). We can calculate the absorption cross-section of acetone vapor at T = 294 K, λex = 310 nm

$$\sigma_{abs} = -\frac{\ln\left(\frac{E_2(p = 10000Pa)}{E_2(p = 500Pa)}\right)}{19 l n_0}. \quad (B.3)$$

The calculated absorption cross-section of acetone vapor at 294 K is $\sigma_{abs} = 1.1785 \times 10^{-24}\ m^2$, which is close to the value proposed by Lozano and coworkers [95], which is $4.7 \times 10^{-24}\ m^2$ at T = 293 K, with an excitation wavelength of 275 nm. The measured value in this thesis and the values in the literature are of the same order of magnitude. Since absorption cross-section is a function of both excitation wavelength and gas temperature. The difference of wavelength and temperature in different study can explain the deviation between the values. The relationship between absorption cross-section and the excitation wavelength were already discussed in Section 3.2.2 and 3.2.3.

A possible limitation in the experimental measurement of absorption cross-section in this thesis is that we did not consider the energy loss due to other optics, such as laser energy absorbed by two Suprasil access, plano-convex lens, mirrors, etc. However, we can consider this problem in a pure mathematical way, as expressed by:

$$\frac{E_2(p = 10000Pa) + C_o}{E_2(p = 500Pa) + C_o} = \frac{E_2(p = 10000Pa)}{E_2(p = 500Pa)}, \quad (B.4)$$

in which C_o is the energy loss due to the optics. Eq.(B.4) holds mathematically, thus our measurement make sense. Future work can also be done to measure E_1, E_2 in visualization chamber without any gas (pure acetone vapor) in it.

Appendix C

Binary gas mixture flow properties calculation

It is underlying to calculate the flow properties of gas mixture flow for numerical and experimental work. Based on the previous work [35; 102], it is known that the pressure of rarefied pure acetone flow, which has a high Knudsen number, is too low to be exploited. The gas mixture composed of a lightweight carrier gas, such as helium or argon, and acetone vapor with a relatively high pressure can also reach a higher Knudsen number. The work of Sharipov showed that if there exists a large difference between molecular mass of two species, the approach for a single species will not be efficient for the gas mixture [147].

Here we introduce the specific approach to define the important properties of binary gas mixture. From the work of Bird [38], the mean free path for the binary gas mixture can be defined by:

$$\lambda = \bar{\lambda} = \sum_{i=1}^{2} \left\{ \left(\frac{n_i}{n} \right) \lambda_i \right\} = \sum_{i=1}^{2} \frac{\chi_i}{\sum_{j=1}^{2} n_j \pi d_{ij}^2 \sqrt{\frac{m_i + m_j}{m_j}}}, \qquad (C.1)$$

with the tracer concentration:

$$\chi_i = \frac{n_i}{n}$$

total density of the gas mixture:

$$n = \sum_{i=1}^{2} n_i,$$

distance between the molecule centres:

$$d_{12} = \frac{(d_1 + d_2)}{2},$$

in which the indices 1 and 2 refers to the tracer vapor and carrier gas, respectively.

The molar mass of the mixture M can be defined as:

$$M = \sum_{i=1}^{2} \frac{n_i}{n} M_i. \qquad (C.2)$$

The specific ideal gas constant can also be described in the equation:

$$R_s = c_p - c_v \qquad (C.3)$$

where c_p is the specific heat at constant pressure and c_v is specific heat at constant volume. The specific heats remain constant for an ideal gas. In that case, we can have the ratio of the specific heats:

$$\gamma = \frac{c_p}{c_V} \tag{C.4}$$

Then the specific heats of an ideal gas can be given by:

$$c_{\mathrm{v}} = \frac{1}{\gamma - 1} R_S \tag{C.5}$$

$$c_{\mathrm{p}} = \frac{\gamma}{\gamma - 1} R_S \tag{C.6}$$

The specific heats of gas mixture can be expressed by:

$$c_p = \sum_{i=1}^{2} \frac{n_i}{n} c_{p,i}, \tag{C.7}$$

$$c_V = \sum_{i=1}^{2} \frac{n_i}{n} c_{V,i}. \tag{C.8}$$

The specific heat ratio of the gas mixture can be defined as:

$$\gamma = \frac{\sum_{i=1}^{2} \frac{n_i}{n} \frac{\gamma_i}{\gamma_i - 1} R_{s,i}}{\sum_{i=1}^{2} \frac{n_i}{n} \frac{1}{\gamma_i - 1} R_{s,i}}, \tag{C.9}$$

with the specific ideal gas constant

$$R_{s,i} = \frac{R_{\mathrm{univ}}}{M_i}.$$

The specific ideal gas constant of the gas mixture can be expressed as:

$$R_s = \frac{R_{\mathrm{univ}}}{M}. \tag{C.10}$$

Compared to the Eq.(C.1) proposed by Bird, Sharipov and Kalempa [148] proposed a simpler approach to calculate the mean free path as following:

$$\lambda = \frac{\sqrt{\pi}\mu}{2p} \left(\frac{2kT}{m} \right)^{\frac{1}{2}}, \tag{C.11}$$

where μ is the viscosity of the mixture, p and T are the pressure and temperature of the gas mixture. The mean molecular mass m can be expressed as:

$$m = \sum_{i=1}^{2} \frac{n_i}{n} m_i. \qquad (C.12)$$

Eq.(C.7) is actually Eq.(2.7) when we choose to use Maxwell molecules model, that is $k_\lambda = \sqrt{\frac{2}{\pi}}$.

References

[1]Chircov, C., & Grumezescu, A. M. (2022). Microelectromechanical Systems (MEMS) for Biomedical Applications. *Micromachines, 13*(2), 164.

[2]Wang, Y.-H., Chen, C.-P., Chang, C.-M., Lin, C.-P., Lin, C.-H., Fu, L.-M., & Lee, C.-Y. (2009). MEMS-based gas flow sensors. *Microfluidics and Nanofluidics, 6*(3), 333. doi:10.1007/s10404-008-0383-4

[3]Fan, L.-S., Tai, Y.-C., & Muller, R. S. (1988). Integrated movable micromechanical structures for sensors and actuators. *IEEE Transactions on Electron Devices, 35*(6), 724-730.

[4]Javed, Y., Mansoor, M., & Shah, I. A. (2019). A review of principles of MEMS pressure sensing with its aerospace applications. *Sensor Review, 39*(5), 652-664. doi:10.1108/SR-06-2018-0135

[5]Ho, C.-M., & Tai, Y.-C. (1998). MICRO-ELECTRO-MECHANICAL-SYSTEMS (MEMS) AND FLUID FLOWS. *Annual Review of Fluid Mechanics, 30*(1), 579-612. doi:10.1146/annurev.fluid.30.1.579

[6]Colin, S. (2013). *Microfluidics*: John Wiley & Sons.

[7]Benam, K. H., Villenave, R., Lucchesi, C., Varone, A., Hubeau, C., Lee, H.-H., . . . Weaver, J. C. (2016). Small airway-on-a-chip enables analysis of human lung inflammation and drug responses in vitro. *Nature methods, 13*(2), 151-157.

[8]Si, L., Bai, H., Rodas, M., Cao, W., Oh, C. Y., Jiang, A., . . . Gilpin, S. E. J. B. (2020). Human organs-on-chips as tools for repurposing approved drugs as potential influenza and COVID19 therapeutics in viral pandemics. *54*.

[9]Si, L., Bai, H., Oh, C. Y., Jin, L., Prantil-Baun, R., & Ingber, D. E. J. M. S. (2021). Clinically relevant influenza virus evolution reconstituted in a human lung airway-on-a-chip. *9*(2), e00257-00221.

[10]Wang, G., Yang, X., Li, J., Wang, Y., & Qing, X. (2021). A flexible microfluidic sensor based on main-channel and branch-channels for aerodynamic pressure measurement. *Sensors and Actuators A: Physical, 319*, 112546. doi:https://doi.org/10.1016/j.sna.2021.112546

[11]Hughes, C. N., Dutta, D., Bashirzadeh, Y., Ahmed, K., & Qian, S. (2015). *Measuring shear stress with A MicroFluidic sensor to improve aerodynamic efficiency.* Paper presented at the 53rd AIAA Aerospace Sciences Meeting.

[12]Chigier, N., & Gemci, T. (2003). *A review of micro propulsion technology.* Paper presented at the 41st Aerospace sciences meeting and exhibit.

[13]Janson, S. W., Helvajian, H., Hansen, W. W., & Lodmell, J. (1999). *Microthrusters for nanosatellites.* Paper presented at the Second International Conference on Integrated Micro Nanotechnology for Space Applications.

[14]Andrikopoulou, C., Le Calvé, S., Sutter, C., Noël, F., Rodríguez-Cuevas, A., Lara-Ibeas, I., . . . Lefebvre, M. (2018). *MAV payload: An air-quality monitoring system for integration inside a drone.* Paper presented at the 10th International Micro-Air Vehicles Conference.

[15]Pour Razzaghi, M. J., Masoumi, Y., Liu, Y., & Rezaei Sani, S. M. J. P. o. F. (2023). Numerical study of microjet and heat flux effects on flow separation and heat transfer over a ramp. *35*(4).

[16]Kumar, V., & Alvi, F. S. J. A. j. (2006). Use of high-speed microjets for active separation control in diffusers. *44*(2), 273-281.

[17]Khobragade, N., Wylie, J., Gustavsson, J., & Kumar, R. J. N. S. (2019). Control of flow separation in a rocket nozzle using microjets. *7*(1), 31-42.

[18]Aubrun, S., McNally, J., Alvi, F., & Kourta, A. (2011). Separation flow control on a generic ground vehicle using steady microjet arrays. *Experiments in Fluids, 51*(5), 1177-1187. doi:10.1007/s00348-011-1132-0

[19]Saliba, G. (2022). *Study and develpment of fluidic micro-oscillators for cooling electronic systems.* Université Paul Sabatier-Toulouse III,

[20]Wang, X., Su, T., Zhang, W., Zhang, Z., Zhang, S. J. M., & Nanoengineering. (2020). Knudsen pumps: A review. *6*(1), 26.

[21]Rojas-Cárdenas, M., Graur, I., Perrier, P., & Méolans, J. G. J. P. o. F. (2013). Time-dependent experimental analysis of a thermal transpiration rarefied gas flow. *25*(7).

[22]López Quesada, G., Tatsios, G., Valougeorgis, D., Rojas-Cárdenas, M., Baldas, L., Barrot, C., & Colin, S. (2020). Thermally driven pumps and diodes in multistage assemblies consisting of microchannels with converging, diverging and uniform rectangular cross sections. *Microfluidics and Nanofluidics, 24*(7), 54. doi:10.1007/s10404-020-02357-z

[23]Rojas Cardenas, M., Graur, I., Perrier, P., & Meolans, J. G. J. P. o. F. (2011). Thermal transpiration flow: A circular cross-section microtube submitted to a temperature gradient. *23*(3), 031702.

[24]McNamara, S., & Gianchandani, Y. B. (2005). On-chip vacuum generated by a micromachined Knudsen pump. *Journal of Microelectromechanical Systems, 14*(4), 741-746. doi:10.1109/JMEMS.2005.850718

[25]Gupta, N. K., An, S., & Gianchandani, Y. B. (2012). A Si-micromachined 48-stage Knudsen pump for on-chip vacuum. *Journal of Micromechanics and Microengineering, 22*(10), 105026.

[26]An, S., Gupta, N. K., & Gianchandani, Y. B. (2014). A Si-Micromachined 162-Stage Two-Part Knudsen Pump for On-Chip Vacuum. *Journal of Microelectromechanical Systems, 23*(2), 406-416. doi:10.1109/JMEMS.2013.2281316

[27]Baier, T., Hardt, S. J. M., & Nanofluidics. (2020). Gas separation in a Knudsen pump inspired by a Crookes radiometer. *24*, 1-10.

[28]Yang, Y. (2013). Experimental and numerical analysis of gas forced convection through Microtubes and Micro Heat Exchangers.

[29]Yang, J., Zhao, Y., Chen, A., & Quan, Z. (2019). Thermal Performance of a Low-Temperature Heat Exchanger Using a Micro Heat Pipe Array. *12*(4), 675.

[30]Colin, S. p. (2004). *Rarefaction and compressibility effects on steady or transient gas flows in microchannels.* Paper presented at the International Conference on Nanochannels, Microchannels, and Minichannels.

[31]Sharipov, F. J. J. o. P., & Data, C. R. (2011). Data on the velocity slip and temperature jump on a gas-solid interface. *40*(2), 023101.

[32]Colin, S. (2011). Gas Microflows in the Slip Flow Regime: A Critical Review on Convective Heat Transfer. *Journal of Heat Transfer, 134*(2). doi:10.1115/1.4005063

[33]Pitakarnnop, J., Varoutis, S., Valougeorgis, D., Geoffroy, S., Baldas, L., & Colin, S. (2010). A novel experimental setup for gas microflows. *Microfluidics and Nanofluidics, 8*(1), 57-72.

[34]Silva, E., Rojas-Cardenas, M., & Deschamps, C. J. (2016). Experimental analysis of velocity slip at the wall for gas flows of nitrogen, R134a, and R600a through a metallic microtube. *international journal of refrigeration, 66*, 121-132.

[35]Fratantonio, D., Rojas-Cárdenas, M., Barrot, C., Baldas, L., & Colin, S. (2020). Velocity measurements in channel gas flows in the slip regime by means of molecular tagging velocimetry. *Micromachines, 11*(4), 374.

[36]Frezzotti, A., Mohand, H. S. H., Barrot, C., & Colin, S. (2015). Role of diffusion on molecular tagging velocimetry technique for rarefied gas flow analysis. *Microfluidics and Nanofluidics, 19*(6), 1335-1348.

[37]Mohand, H. S. H., Frezzotti, A., Brandner, J. J., Barrot, C., & Colin, S. (2017). Molecular tagging velocimetry by direct phosphorescence in gas microflows: correction of Taylor dispersion. *Experimental Thermal and Fluid Science, 83*, 177-190.

[38]Bird, G. A., & Brady, J. (1994). *Molecular gas dynamics and the direct simulation of gas flows* (Vol. 42): Clarendon press Oxford.

[39]Kandlikar, S., Garimella, S., Li, D., Colin, S., & King, M. R. (2005). *Heat transfer and fluid flow in minichannels and microchannels*: elsevier.

[40]Shen, C. (2006). *Rarefied gas dynamics: fundamentals, simulations and micro flows*: Springer Science & Business Media.

[41]Koura, K., & Matsumoto, H. J. P. o. f. A. f. d. (1991). Variable soft sphere molecular model for inverse‐power‐law or Lennard‐Jones potential. *3*(10), 2459-2465.

[42]Koura, K., & Matsumoto, H. J. P. o. F. A. F. D. (1992). Variable soft sphere molecular model for air species. *4*(5), 1083-1085.

[43]Maxwell, J. C. J. P. T. o. t. r. s. o. L. (1879). VII. On stresses in rarified gases arising from inequalities of temperature. (170), 231-256.

[44]SAGAR, M. A., ALI, S. M., MANJARI, A. N., Sushma, L. J. I. J. o. M., Research, P. E., & Development. (2019). Effect of Knudsen number on blunt body during hypersonic speeds for reducing drag. *9*(6), 451-462.

[45]Colin, S., Fernández, J. M., Barrot, C., Baldas, L., Bajić, S., & Rojas-Cárdenas, M. J. M. (2022). Review of optical thermometry techniques for flows at the microscale towards their applicability to gas microflows. *13*(11), 1819.

[46]Agrawal, A. (2012). A comprehensive review on gas flow in microchannels. *International Journal of Micro-Nano Scale Transport*.

[47]Cercignani, C., Illner, R., & Pulvirenti, M. (2013). *The mathematical theory of dilute gases* (Vol. 106): Springer Science & Business Media.

[48]Karniadakis, G. E., Beskok, A., & Gad-el-Hak, M. J. A. M. R. (2002). Micro flows: fundamentals and simulation. *55*(4), B76-B76.

[49]Chapman, S., Cowling, T. G., & Burnett, D. (1952). *The Mathematical Theory of Non-uniform Gases: An Account of Kinetic Theory of Viscosity, Thermal Conduction, and Diffusion*: Cambridge University Press.

[50]Deissler, R. J. I. J. o. H., & Transfer, M. (1964). An analysis of second-order slip flow and temperature-jump boundary conditions for rarefied gases. *7*(6), 681-694.

[51]Cercignani, C. (1969). *Mathematical methods in kinetic theory* (Vol. 1): Springer.

[52]Hsia, Y.-T., & Domoto, G. (1983). An experimental investigation of molecular rarefaction effects in gas lubricated bearings at ultra-low clearances.
[53]Mitsuya, Y. (1993). Modified Reynolds equation for ultra-thin film gas lubrication using 1.5-order slip-flow model and considering surface accommodation coefficient.
[54]Hadjiconstantinou, N. G. J. P. o. F. (2003). Comment on Cercignani's second-order slip coefficient. *15*(8), 2352-2354.
[55]Cercignani, C., & Lorenzani, S. J. P. o. F. (2010). Variational derivation of second-order slip coefficients on the basis of the Boltzmann equation for hard-sphere molecules. *22*(6).
[56]Lorenzani, S. J. P. T. o. t. R. S. A. M., Physical, & Sciences, E. (2011). Higher order slip according to the linearized Boltzmann equation with general boundary conditions. *369*(1944), 2228-2236.
[57]Silva, G., & Semiao, V. J. P. R. E. (2017). Consistent lattice Boltzmann modeling of low-speed isothermal flows at finite Knudsen numbers in slip-flow regime: Application to plane boundaries. *96*(1), 013311.
[58]Maxwell, J. C. (1890). *The Scientific Papers of James Clerk Maxwell* (Vol. 2): University Press.
[59]Winer, M. H., Ahmadi, A., & Cheung, K. C. J. L. o. a. C. (2014). Application of a three-dimensional (3D) particle tracking method to microfluidic particle focusing. *14*(8), 1443-1451.
[60]Ebert, W., & Sparrow, E. M. (1965). Slip flow in rectangular and annular ducts.
[61]Colin, C. A., StÉphane %J Microscale Thermophysical Engineering. (2001). High-order boundary conditions for gaseous flows in rectangular microducts. *5*(1), 41-54.
[62]Prud'Homme, R. K., Chapman, T. W., & Bowen, J. R. J. A. s. r. (1986). Laminar compressible flow in a tube. *43*, 67-74.
[63]Van den Berg, H., Ten Seldam, C., & Van der Gulik, P. J. J. o. F. M. (1993). Compressible laminar flow in a capillary. *246*, 1-20.
[64]Beskok, A., & Karniadakis, G. J. A. P. (1993). Simulation of heat and momentum transfer in micro-geometries. *933269*.
[65]Arkilic, E. B., Schmidt, M. A., & Breuer, K. S. (1997). Gaseous slip flow in long microchannels. *Journal of Microelectromechanical systems, 6*(2), 167-178.
[66]Zohar, Y., Lee, S. Y. K., Lee, W. Y., Jiang, L., & Tong, P. J. J. o. f. m. (2002). Subsonic gas flow in a straight and uniform microchannel. *472*, 125-151.
[67]Wilson, R. J. A. J. (1973). Aerodynamic interference of pitot tubes in a turbulent boundary layer at supersonic speed. *11*(10), 1420-1421.
[68]Evans, M. J., & Medwell, P. R. (2019). Understanding and Interpreting Laser Diagnostics in Flames: A Review of Experimental Measurement Techniques. *5*. doi:10.3389/fmech.2019.00065
[69]Abdulwahab, M. R., Ali, Y. H., Habeeb, F. J., Borhana, A. A., Abdelrhman, A. M., Al-Obaidi, S. M. A. J. J. o. A. R. i. F. M., & Sciences, T. (2020). A review in particle image velocimetry techniques (developments and applications). *65*(2), 213-229.
[70]Ashwood, A., Hogen, S. V., Rodarte, M., Kopplin, C., Rodríguez, D., Hurlburt, E., & Shedd, T. J. I. J. o. M. F. (2015). A multiphase, micro-scale PIV measurement technique for liquid film velocity measurements in annular two-phase flow. *68*, 27-39.
[71]Li, Y., Kazemifar, F., Blois, G., & Christensen, K. T. J. W. R. R. (2017). Micro ‐ PIV measurements of multiphase flow of water and liquid CO 2 in 2 ‐ D heterogeneous porous micromodels. *53*(7), 6178-6196.

[72]Rajan, V., Varghese, B., van Leeuwen, T. G., & Steenbergen, W. (2009). Review of methodological developments in laser Doppler flowmetry. *Lasers in Medical Science, 24*(2), 269-283. doi:10.1007/s10103-007-0524-0

[73]Ehn, A., Zhu, J., Li, X., & Kiefer, J. (2017). Advanced Laser-Based Techniques for Gas-Phase Diagnostics in Combustion and Aerospace Engineering. *Applied Spectroscopy, 71*(3), 341-366.

[74]Kerhervé, F., Jordan, P., Gervais, Y., Valiere, J.-C., & Braud, P. J. E. i. f. (2004). Two-point laser Doppler velocimetry measurements in a Mach 1.2 cold supersonic jet for statistical aeroacoustic source model. *37*(3), 419-437.

[75]Koochesfahani, M. M., & Nocera, D. G. (2007). Molecular tagging velocimetry. *Handbook of experimental fluid dynamics*, 362-382.

[76]Hoffmann, M., Schlüter, M., & Räbiger, N. J. C. e. s. (2006). Experimental investigation of liquid–liquid mixing in T-shaped micro-mixers using μ-LIF and μ-PIV. *61*(9), 2968-2976.

[77]Jahanmiri, M. (2011). *Particle image velocimetry: Fundamentals and its applications*. Retrieved from

[78]Fang, C., & Hong, L. J. C. J. o. A. (2018). Particle image velocimetry for combustion measurements: Applications and developments. *31*(7), 1407-1427.

[79]Li, F., Zhang, H., & Bai, B. J. M. (2021). A review of molecular tagging measurement technique. *171*, 108790.

[80]Choi, D., Byun, J., & Park, H. J. J. o. F. M. (2022). Analysis of liquid column atomization by annular dual-nozzle gas jet flow. *943*, A25.

[81]Samouda, F., Colin, S., Barrot, C., Baldas, L., & Brandner, J. J. (2015). Micro molecular tagging velocimetry for analysis of gas flows in mini and micro systems. *Microsystem Technologies, 21*(3), 527-537.

[82]Yamaguchi, H., Hayashida, K., Ishiguro, Y., Takamori, K., Matsuda, Y., & Niimi, T. (2016). Micro-molecular tagging velocimetry of internal gaseous flow. *Microfluidics and Nanofluidics, 20*(2), 32.

[83]Matsunuma, T., Abe, H., Tsutsui, Y. J. J. I. J. S. B. F., & Engineering, T. (2002). LDV measurements of unsteady flow within a turbine rotor at low Reynolds numbers. *45*(3), 457-464.

[84]Kyoden, T., Akiguchi, S., Tajiri, T., Andoh, T., Furuichi, N., Doihara, R., . . . Instrumentation. (2019). Assessing the infinitely expanding intersection region for the development of large-scale multipoint laser Doppler velocimetry. *70*, 101660.

[85]Kyoden, T., Yasue, Y., Ishida, H., Akiguchi, S., Andoh, T., Takada, Y., . . . Hachiga, T. J. J. J. o. A. P. (2014). Multi-channel laser Doppler velocimetry using a two-dimensional optical fiber array for obtaining instantaneous velocity distribution characteristics. *54*(1), 012501.

[86]Andrade, A., Hoffman, E. N., LaLonde, E. J., & Combs, C. S. J. O. E. (2022). Velocity measurements in a hypersonic flow using acetone molecular tagging velocimetry. *30*(23), 42199-42213.

[87]Samouda, F., Brandner, J., Barrot, C., & Colin, S. (2012). *Velocity field measurements in gas phase internal flows by molecular tagging velocimetry.* Paper presented at the Journal of Physics: Conference Series.

[88]Ismailov, M. M., Schock, H. J., & Fedewa, A. M. (2006). Gaseous flow measurements in an internal combustion engine assembly using molecular tagging velocimetry. *Experiments in Fluids, 41*(1), 57-65.

[89]Miles, R., Cohen, C., Connors, J., Howard, P., Huang, S., Markovitz, E., & Russell, G. (1987). Velocity measurements by vibrational tagging and fluorescent probing of oxygen. *Optics Letters, 12*(11), 861-863.

[90]Miles, R. B., Grinstead, J., Kohl, R. H., & Diskin, G. (2000). The RELIEF flow tagging technique and its application in engine testing facilities and for helium-air mixing studies. *Measurement Science and Technology, 11*(9), 1272.

[91]Pitz, R. W., Wehrmeyer, J. A., Ribarov, L. A., Oguss, D. A., Batliwala, F., DeBarber, P. A., . . . Dimotakis, P. E. (2000). Unseeded molecular flow tagging in cold and hot flows using ozone and hydroxyl tagging velocimetry. *Measurement Science and Technology, 11*(9), 1259.

[92]ElBaz, A., & Pitz, R. (2012). N 2 O molecular tagging velocimetry. *Applied Physics B, 106*(4), 961-969.

[93]Fratantonio, D., Rojas-Cardenas, M., Mohand, H. S. H., Barrot, C., Baldas, L., & Colin, S. (2018). Molecular tagging velocimetry for confined rarefied gas flows: Phosphorescence emission measurements at low pressure. *Experimental Thermal and Fluid Science, 99*, 510-524.

[94]Thurber, M. C., Grisch, F., Kirby, B. J., Votsmeier, M., & Hanson, R. K. (1998). Measurements and modeling of acetone laser-induced fluorescence with implications for temperature-imaging diagnostics. *Applied Optics, 37*(21), 4963-4978. doi:10.1364/AO.37.004963

[95]Lozano, A., Yip, B., & Hanson, R. (1992). Acetone: a tracer for concentration measurements in gaseous flows by planar laser-induced fluorescence. *Experiments in Fluids, 13*(6), 369-376.

[96]Almy, G., & Anderson, S. (1940). Lifetime of fluorescence in diacetyl and acetone. *The Journal of Chemical Physics, 8*(10), 805-814.

[97]Kaskan, W., & Duncan, A. F. (1950). Mean lifetime of the fluorescence of acetone and biacetyl vapors. *The Journal of Chemical Physics, 18*(4), 427-431.

[98]Thurber, M., & Hanson, R. K. J. A. P. B. (1999). Pressure and composition dependences of acetone laser-induced fluorescence with excitation at 248, 266, and 308 nm. *69*(3), 229-240.

[99]Fratantonio, D., Yeachana, V., Rojas-Cárdenas, M., Colin, S., & Barrot-Lattes, C. (2018). *Imaging technique for measuring the diffusion of diacetyl and acetone vapors at low pressures*. Paper presented at the 31st International Symposium on Rarefied Gas Dynamics, Glasgow, United Kingdom. https://hal.archives-ouvertes.fr/hal-03517063

[100]Lempert, W. R., Boehm, M., Jiang, N., Gimelshein, S., & Levin, D. (2003). Comparison of molecular tagging velocimetry data and direct simulation Monte Carlo simulations in supersonic micro jet flows. *Experiments in Fluids, 34*(3), 403-411. doi:10.1007/s00348-002-0576-7

[101]Tran, T., Kochar, Y., & Seitzman, J. (2005). *Measurement of liquid acetone fluorescence and phosphorescence for two-phase imaging.* Paper presented at the 43rd AIAA Aerospace Sciences Meeting and Exhibit.

[102]Fratantonio, D. (2019). *Molecular tagging velocimetry in rarefied and confined gas flows.* INSA Toulouse,

[103]Roetmann, K., Schmunk, W., Garbe, C. S., & Beushausen, V. J. E. i. f. (2008). Micro-flow analysis by molecular tagging velocimetry and planar Raman-scattering. *44*(3), 419-430.

[104]Fort, C., Andre, M., & Bardet, P. (2020). *Development of long distance 2D micro-molecular tagging velocimetry (μMTV) to measure wall shear stress.* Paper presented at the AIAA Scitech 2020 Forum.

[105]Gendrich, C., Koochesfahani, M., & Nocera, D. J. E. i. f. (1997). Molecular tagging velocimetry and other novel applications of a new phosphorescent supramolecule. *23*(5), 361-372.

[106]Hu, H., Koochesfahani, M. M. J. M. S., & Technology. (2006). Molecular tagging velocimetry and thermometry and its application to the wake of a heated circular cylinder. *17*(6), 1269.

[107]Hosokawa, S., Fukunaga, T., & Tomiyama, A. J. E. i. f. (2009). Application of photobleaching molecular tagging velocimetry to turbulent bubbly flow in a square duct. *47*(4), 745-754.

[108]Stier, B., & Koochesfahani, M. (1999). Molecular tagging velocimetry (MTV) measurements in gas phase flows. *Experiments in Fluids, 26*(4), 297-304.

[109]Andre, M., Bardet, P., Cadell, S., Woods, B., Burns, R., & Danehy, P. (2017). *Development of a molecular tagging velocimetry technique for non-intrusive velocity measurements in low-speed gas flows.* Paper presented at the International Topical Meeting on Nuclear Reactor Thermal Hydraulics (NURETH-17).

[110]Smith, C. D., Lester, L. E., Siddiqui, F., & Gragston, M. (2023). *10 kHz Acetone Molecular Tagging Velocimetry in a Mach 4 Ludwieg Tube.* Paper presented at the AIAA SCITECH 2023 Forum.

[111]Pitz, R. W., Danehy, P. M. J. O. D. f. R., Theory, N.-R. F., & Practice. (2020). Molecular Tagging Velocimetry in Gases.

[112]Segall, B. A., Shekhtman, D., Hameed, A., Chen, J. H., & Parziale, N. J. J. E. i. F. (2023). Profiles of streamwise velocity and fluctuations in a hypersonic turbulent boundary layer using acetone tagging velocimetry. *64*(6), 122.

[113]Koochesfahani, M. (1999). *Molecular Tagging Velocimetry (MTV)-progress and applications.* Paper presented at the 30th Fluid Dynamics Conference.

[114]ElBaz, A., & Pitz, R. J. A. P. B. (2012). N2O molecular tagging velocimetry. *106*(4), 961-969.

[115]Bathel, B. F., Danehy, P. M., Inman, J. A., Jones, S. B., Ivey, C. B., & Goyne, C. P. (2011). Velocity profile measurements in hypersonic flows using sequentially imaged fluorescence-based molecular tagging. *AIAA journal, 49*(9), 1883-1896.

[116]Lempert, W. R., Jiang, N., Sethuram, S., & Samimy, M. J. A. j. (2002). Molecular tagging velocimetry measurements in supersonic microjets. *40*(6), 1065-1070.

[117]Hammer, P., Pouya, S., Naguib, A., & Koochesfahani, M. (2013). A multi-time-delay approach for correction of the inherent error in single-component molecular tagging velocimetry. *Measurement Science and Technology, 24*(10), 105302.

[118]Samouda, F. (2012). *Développement de la technique de Vélocimétrie par Marquage Moléculaire pour l'étude expérimentale des micro-écoulements gazeux.* Toulouse, INSA,

[119]Marrero, T. R., Mason, E. A. J. J. o. P., & Data, C. R. (1972). Gaseous diffusion coefficients. *1*(1), 3-118.

[120]Van der Perre, S., Van Assche, T., Bozbiyik, B., Lannoeye, J., De Vos, D. E., Baron, G. V., & Denayer, J. F. (2014). Adsorptive characterization of the ZIF-68 metal-organic framework: a complex structure with amphiphilic properties. *Langmuir, 30*(28), 8416-8424.

[121]Song, Z., Huang, Y., Xu, W. L., Wang, L., Bao, Y., Li, S., & Yu, M. (2015). Continuously adjustable, molecular-sieving "gate" on 5A zeolite for distinguishing small organic molecules by size. *Scientific reports, 5*, 13981.

[122]Navaneethan, M., Mani, G. K., Ponnusamy, S., Tsuchiya, K., Muthamizhchelvan, C., Kawasaki, S., & Hayakawa, Y. (2017). Influence of Al doping on the structural, morphological, optical, and gas sensing properties of ZnO nanorods. *Journal of Alloys and Compounds, 698*, 555-564.

[123]Hu, H., Zhu, J., Yang, F., Chen, Z., Deng, M., Weng, L., . . . Zhou, Y. (2019). A robust etb-type metal–organic framework showing polarity-exclusive adsorption of acetone over methanol for their azeotropic mixture. *Chemical Communications, 55*(46), 6495-6498. doi:10.1039/C9CC02439E

[124]Nadykto, A. B., & Yu, F. (2003). Uptake of neutral polar vapor molecules by charged clusters/particles: Enhancement due to dipole‐charge interaction. *Journal of Geophysical Research: Atmospheres, 108*(D23).

[125]Bowen, T. C., Noble, R. D., & Falconer, J. L. J. J. o. M. S. (2004). Fundamentals and applications of pervaporation through zeolite membranes. *245*(1-2), 1-33.

[126]Einstein, A. (1956). *Investigations on the Theory of the Brownian Movement*: Courier Corporation.

[127]Rousson, V., & Goşoniu, N. F. J. S. M. (2007). An R-square coefficient based on final prediction error. *4*(3), 331-340.

[128]Sinnakaudan, S., Ghani, A. A., Ahmad, M., & Zakaria, N. J. J. o. H. E. (2006). Multiple linear regression model for total bed material load prediction. *132*(5), 521-528.

[129]Vidyullatha, P., Rao, D. R. J. I. J. o. E., & Engineering, C. (2016). Machine learning techniques on multidimensional curve fitting data based on R-square and chi-square methods. *6*(3), 974.

[130]Garabedian, M. E., & Dows, D. A. J. J. o. t. A. C. S. (1968). Vapor-phase bimolecular quenching of the triplet state of biacetyl. *90*(10), 2468-2470.

[131]Sidebottom, H. W., Badcock, C. C., Calvert, J. G., Rabe, B. R., & Damon, E. K. J. J. o. t. A. C. S. (1972). Lifetime studies of the biacetyl excited singlet and triplet states in the gas phase at 25. deg. *94*(1), 13-19.

[132]Sijtsema, N. M., Dam, N. J., Klein-Douwel, R. J., & Ter Meulen, J. J. A. j. (2002). Air photolysis and recombination tracking: a new molecular tagging velocimetry scheme. *40*(6), 1061-1064.

[133]Hsu, A. G., Srinivasan, R., Bowersox, R. D., & North, S. W. J. A. j. (2009). Molecular tagging using vibrationally excited nitric oxide in an underexpanded jet flowfield. *47*(11), 2597-2604.

[134]Danehy, P. M., Burns, R. A., Reese, D. T., Retter, J. E., & Kearney, S. P. J. A. R. o. F. M. (2022). FLEET velocimetry for aerodynamics. *54*, 525-553.

[135]Limbach, C. M., & Miles, R. B. J. A. J. (2017). Rayleigh scattering measurements of heating and gas perturbations accompanying femtosecond laser tagging. *55*(1), 112-120.

[136]Jiang, N., Halls, B. R., Stauffer, H. U., Danehy, P. M., Gord, J. R., & Roy, S. (2016). *Selective two-photon absorptive resonance femtosecond-laser electronic-excitation tagging (STARFLEET) velocimetry in flow and combustion diagnostics.* Paper presented at the 32nd AIAA Aerodynamic Measurement Technology and Ground Testing Conference.

[137]Bominaar, J., Pashtrapanska, M., Elenbaas, T., Dam, N., Ter Meulen, H., & van de Water, W. J. P. R. E. (2008). Writing in turbulent air. *77*(4), 046312.

[138]Edwards, M., Dogariu, A., & Miles, R. (2013). *Simultaneous temperature and velocity measurement in unseeded air flows with FLEET.* Paper presented at the 51st AIAA Aerospace Sciences Meeting including the New Horizons Forum and Aerospace Exposition.

[139]DeLuca, N. J., Miles, R. B., Kulatilaka, W. D., Jiang, N., & Gord, J. R. (2014). *Femtosecond laser electronic excitation tagging (FLEET) fundamental pulse energy and spectral response.* Paper presented at the 30th AIAA aerodynamic measurement technology and ground testing conference.

[140]Burns, R. A., Danehy, P. M., Jiang, N., Slipchenko, M. N., Felver, J., & Roy, S. (2018). Unseeded Velocimetry in Nitrogen for High-Pressure Cryogenic Wind Tunnels, Part 2: Picosecond-Laser Tagging. *Meas Sci Technol, 29*(11). doi:10.1088/1361-6501/aade15

[141]New-Tolley, M. R., Shneider, M. N., & Miles, R. B. (2017). *Modeling of the FLEET filament interaction with a nonuniform gas flow.* Paper presented at the 55th AIAA Aerospace Sciences Meeting.

[142]Mirzaei, M., Dam, N., & van de Water, W. J. P. R. E. (2012). Molecular tagging velocimetry in turbulence using biacetyl. *86*(4), 046318.

[143]Heicklen, J. J. J. o. t. A. C. S. (1959). The fluorescence and phosphorescence of biacetyl vapor and acetone vapor1. *81*(15), 3863-3866.

[144]Fantner, G. J. A. a. E. h. w. e. c. l. l. w.-c. u. E.-P. p. a. p. (2013). A brief introduction to error analysis and propagation.

[145]Rojas-Cárdenas, M., Silva, E., Ho, M.-T., Deschamps, C. J., Graur, I. J. M., & Nanofluidics. (2017). Time-dependent methodology for non-stationary mass flow rate measurements in a long micro-tube: Experimental and numerical analysis at arbitrary rarefaction conditions. *21*, 1-15.

[146]Coltman, E., Lipp, M., Vescovini, A., & Helmig, R. J. T. i. P. M. (2020). Obstacles, interfacial forms, and turbulence: A numerical analysis of soil–water evaporation across different interfaces. *134*, 275-301.

[147]Sharipov, F. J. J. o. V. S., Technology A: Vacuum, S., & Films. (2013). Gaseous mixtures in vacuum systems and microfluidics. *31*(5), 050806.

[148]Sharipov, F., Kalempa, D. J. J. o. V. S., Technology A: Vacuum, S., & Films. (2002). Gaseous mixture flow through a long tube at arbitrary Knudsen numbers. *20*(3), 814-822.